Microwave Breast Cancer Detection: Signal Processing and Device Prototype

Evgeny Kirshin

Department of Electrical & Computer Engineering
McGill University, Montreal

August 2015

A thesis submitted to McGill University in partial fulfillment of the requirements for the degree of Doctor of Philosophy.

This thesis is dedicated to my parents, Liudmila Kirshyna and Aliaksandr Kirshyn.

Abstract

Breast cancer, one of the primary causes of women mortality worldwide, can be effectively treated if detected at its early stage. Micro**w**ave Imaging (MWI), an emerging technique, promises to complement the currently used diagnostic modalities. It is safe, non-ionizing and potentially inexpensive, thus possessing key features to make it a good candidate for frequent and mass screenings.

This thesis summarizes results of novel research done towards a prototype of a microwave device aimed at screening breast tissues.

The author first presents the results of a research to combine Micro**w**ave Radar (MWR) breast imaging technique with Micro**w**ave-Induced Thermoacoustic (MWIT) imaging to improve tumor detection rate. An optimal rule for fusing information from the two modalities is developed and applied to numerically-simulated microwave and acoustic signals. The results demonstrate advantages of the hybrid method, compared to the MWR and MWIT methods used individually.

Next, the thesis describes a research study to address the challenge of data acquisition in MWI. Recording microwave signals with high signal-to-noise ratio is either too expensive or suffers from numerous artifacts and measurement errors. The author presents studies aimed to improve the quality of collected time-domain data by minimizing the effect of phase uncertainties using software compensation.

Finally, the thesis focuses on MWI algorithms. A comparative analysis of several existing time-domain MWI algorithms is accomplished to identify their advantages and weaknesses. This analysis yields important lessons on algorithm development in the light of the specific challenges presented by the MWI of the breast tissue. The author presents two improved MWI algorithms that address the identified drawbacks of the existing algorithms. The performance of the new algorithms is evaluated with experimentally-recorded data sets.

Sommaire

Le cancer du sein, l'une des principales causes de mortalité chez les femmes dans le monde, peut être traité efficacement s'il est détecté à son stade précoce. L'imagerie par micro-ondes (MWI), une technique émergente, promet de compléter les modalités de diagnostic actuelles. Elle est sécuritaire, non-ionisante et potentiellement peu coûteuse, possédant ainsi les principales caractéristiques pour en faire une bonne candidate pour des dépistages fréquents et de masse.

Cette thèse résume les résultats des nouvelles recherches concernant le prototype d'un dispositif de micro-ondes destiné à examiner les tissus mammaires.

L'auteur présente en premier lieu les résultats de recherche qui combine la technique d'imagerie de radar micro-ondes (MWR) avec l'imagerie thermoacoustique induite par micro-ondes (MWIT) afin d'améliorer le taux de détection des tumeurs. Une règle optimale pour combiner l'information des deux modalités est développée et applique aux signaux numériquement simulés micro-ondes et acoustiques. Les résultats démontrent les avantages de la méthode hybride par rapport aux méthodes MWR et MWIT utilisées séparément.

Ensuite, la thèse décrit une étude de recherche pour relever les difficultés de l'acquisition des données en imagerie MWI. L'enregistrement de signaux micro-ondes ayant un rapport signal-bruit élevé est soit trop coûteux, soit génère des artefacts ou de nombreuses erreurs de mesure. L'auteur présente des études visant à améliorer la qualité des données recueillies dans le domaine temporel en minimisant l'effet des incertitudes de phase en utilisant la compensation de logiciel.

Finalement, la thèse se concentre sur les algorithmes MWI. Une analyse comparative de plusieurs algorithmes MWI dans le domaine temporel existant est réalisée pour en identifier leurs avantages et faiblesses. Cette analyse enseigne des leçons importantes sur la conception d'algorithmes à la lumière des défis spécifiques présentés par le MWI des tissus mammaires. L'auteur présente deux algorithmes MWI améliorés qui concernent des limitations identifiées des algorithmes existants. La performance des nouveaux algorithmes est évaluée à l'aide de données enregistrées.

Acknowledgments

First, I would like to express gratitude to my research supervisor, Prof. Milica Popović. Without her caring support and guidance, my work would not be possible.

I thank Prof. Mark Coates for co-supervising my research in the area of signal processing. His critical feedback was always valuable. I would like to acknowledge all members of our research group, with whom I collaborated: Emily Porter, Adam Santorelli, Guangran Kevin Zhu and Boris Oreshkin. I am happy to remember the days of our meetings, discussions and experiments with the equipment.

Great support has been provided from the laboratory of telecommunications and signal processing: I highly appreciate all the help from Prof. Mike Rabbat for sharing the network cluster, which significantly accelerated our numerical computations.

I was lucky to have helpful and cheerful lab mates. I am grateful to Tapabrata Mukherjee for his sincere friendship. I would like to thank Hussein Moghnieh for his warm welcome to the lab and further support in many things. I highly value all the encouragement and source of motivation from Maryam Golshayan and Maryam Mehri. I would like to say thank you to Adrian Ngoly, who infected me with his tremendously curious attitude to Knowledge. Many thanks go to Jian Wang and Rajeev Das for valuable discussions and interesting ideas. I would like to thank Nadine Kolment for helping with the translation of the Abstract into French language.

Our research would not be possible without funding provided by Natural Sciences and Engineering Research Council of Canada (NSERC) and PROMPT Quebec.

I am especially grateful to my parents, Liudmila Kirshyna and Aliaksandr Kirshyn, who have always supported and encouraged me with my work.

Preface and contribution of authors

This thesis represents three studies with the following contributions:

1. Chapter 4 - Dual-modality microwave breast cancer detection: MWR and MWIT. Specific contributions are:
    - The derivation of the fusion rule of the MWR and MWIT signals and analysis of the resulting noise distribution for setting a detection threshold;
    - Application of the developed data fusion rule to numerically simulated two-dimensional data to evaluate the performance of the combined method versus the MWR and MWIT methods alone.
2. Chapter 5 - Phase uncertainty compensation from time-domain data acquisition system, with the following specific contributions:
    - A developed method to estimate phase delay between two channels of the recording device based on the analysis of "step"-like signals;
    - Assessment of the variability of the phase delays in the recording device to demonstrate that the phase delay of the two channels with respect to the trigger is significantly correlated between the channels, thus enabling software compensation of the phase uncertainty by phase-aligning the recorded signals;
    - Optimization of the alignment method using experimental data.
3. Chapter 6 - Advancement of time-domain microwave imaging algorithms, with the following specific contributions:
    - Evaluation of several algorithms, mostly presented in the literature, and identification of those that can offer high performance for dense and highly heterogeneous cases;
    - Derivation of an **o**ptimized version of the Delay-Multiply-And-Sum (DMASo) algorithm and assessment of its computational complexity;
    - Development of a **f**requency-domain counterpart of the Delay-And-Sum (DASf) algorithm and evaluation of the algorithm on three-dimensional experimentally-recorded data.

The contribution of the research group members to the work are specified below.

- The author of this thesis claims the following original work:

    1. Chapter 4: he derived the optimal data fusion rule for the dual-modality detection; managed preparation of numerical datasets; he applied the developed algorithm to the numerically simulated data and evaluated the detection performance;
    2. Chapter 5: he proposed a method to compensate for the phase uncertainty in microwave data acquisition system; he developed a method to estimate phase delays between two channels of the recording device based on the analysis of "step"-like signals; he studied the variability of the phase delays between the channels in the recorded device to confirm the hypothesis of their correlated behavior; he applied and statistically evaluated the developed signal alignment method using experimental signals;
    3. Chapter 6: he implemented existing MWI algorithms discussed in the literature; managed preparation of numerical datasets for two-dimensional modeling and was involved in the data acquisition process for the experimental three-dimensional imaging; he applied and evaluated the existing microwave imaging algorithms using the two-dimensional numerical datasets; he derived and implemented the DASf algorithm; he mathematically optimized and implemented the improved version of the DMAS algorithm (DMASo); studied the performance of the DASf and DMASo algorithms using the experimentally acquired signals from realistic breast phantoms.

- Guangran Kevin Zhu implemented the two-dimensional FDTD simulator, helped preparing numerical breast phantoms and run numerical simulations on a computational cluster. These simulated signals were used both for the dual-modality detection study (chapter 4) and for the evaluation of MWI algorithms (chapter 6).

- Boris Oreshkin helped deriving the expressions for noise distribution of the dual-modality test statistics for hypothesis testing and setting a threshold. He also initially

implemented the Generalized Likelihood Ratio Test (GLRT) and skin-breast artifact removal algorithms.

- Adam Santorelli and Emily Porter contributed to the work described in chapter 6 with the acquisition of the experimental signals. In particular, they executed the system setup, prepared realistic breast phantoms and recorded the datasets used for testing the algorithms.

Contents

List of Figures

List of Tables

List of Abbreviations

Abbreviation	Meaning
3D	Three-Dimensional
ADC	Analog-to-Digital Converter
APES	Amplitude and Phase E**s**timation (imaging algorithm)
CDF	Cumulative Distribution Function
CT	Computed Tomography (clinical method to diagnose breast cancer)
DAS	Delay-And-Sum (imaging algorithm)
DASi	Delay-And-Sum with **i**nterpolation spatial focusing (imaging algorithm)
DASf	Delay-And-Sum in **f**requency domain (imaging algorithm)
DASs	Delay-And-Sum with **s**ample-by-sample spatial focusing (imaging algorithm)
DBT	Digital Breast Tomosynthesis (relatively new clinical method to detect breast cancer)
DCIS	Ductal Carcinoma In Situ (type of breast cancer)
DMAS	Delay-Multiply-And-Sum (imaging algorithm)
DMASo	Delay-Multiply-And-Sum, **o**ptimized version (imaging algorithm)
EIM	Electrical Impedance Mapping (alternative breast imaging method)
EIS	Electrical Impedance Spectroscopy (alternative breast imaging method)
EIT	Electric Impedance Tomography (equivalent to EIS)
EM	Electro**m**agnetic (referred to waves, radiation, etc.)
FAS	Filter-And-Sum (imaging algorithm)
FDA	Food and Drug Administration
FDR	False Discovery Rate (one of the metrics to characterize detection performance)
FDTD	Finite-Difference Time-Domain (numerical analysis technique)
FE	Finite-Element (numerical analysis technique)
FFT	Fast Fourier Transform (type of signal transformation)

GLRT	Generalized Likelihood Ratio Test (method to test hypotheses, used as one of breast imaging algorithms)
IDAS	Improved Delay-And-Sum (imaging algorithm)
IDC	Invasive Ductal Carcinoma (type of breast cancer)
ILC	Invasive Lobular Carcinoma (type of breast cancer)
LCIS	Lobular Carcinoma In Situ (type of breast cancer)
MAMI	Multistatic Adaptive Microwave Imaging (imaging algorithm)
MCU	Micro**c**ontroller Unit (equivalent to "microcontroller")
MWI	Micro**w**ave Imaging (a set of imaging techniques that use microwaves)
MIST	Microwave Imaging via Space-Time beamforming (imaging algorithm, equivalent to FAS beamforming)
MWIT	Micro**w**ave-Induced Thermoacoustics (here, as a method to detect breast cancer)
MLE	Maximum-Likelihood Estimates (estimated values of variables based on maximum likelihood assumption)
MOM	Method Of Moments (numerical analysis technique)
MWR	Micro**w**ave Radar (here, as a method to detect breast cancer)
MRI	Magnetic Resonance Imaging (clinical method, used to diagnose breast cancer)
MSE	Mean Squared Error (metric between two vectors)
MSHM	Maximum Size at Half Maximum (image quality metric for imaging algorithms)
MT	Microwave Tomography (one of microwave imaging methods)
MVDR	Minimum-Variance Distortion-less Response beamformer (imaging method)
MUX	M**u**ltiple**x**er (hardware element for connecting one channel to one of a set of others)
NIS	Near Infrared Spectroscopy (alternative breast imaging method)
PC	Personal Computer
PET	Positron-Emission Tomography (imaging technique that can be used for breast cancer detection)
PSLR	Peak to Side-Lobe Ratio (image quality metric for imaging algorithms)
RMVB	Robust Minimum-Variance Beamformer (imaging algorithm)
RCB	Robust Capon Beamformer (imaging algorithm)
RF	Radio Frequency (frequency range from 3kHz to 300GHz)
RWCB	Robust Weighted Capon Beamformer (imaging algorithm)
RX	Receiver (referred to an antenna or a path of RF switching matrix)
SAR	Specific Absorption Rate (characteristic of material under RF radiation)

SNR	Signal-to-Noise Ratio (metric characterizing quality of a signal or an image)
SINR	Signal-to-Interference-and-Noise Ratio (metric characterizing quality of a signal or an image)
SP8T	Single Pole eight Throw (type of switch, 1x8)
SPDT	Single Pole Dual Throw (type of switch, 1x2)
SPECT	Single-Photon Emission Computed Tomography (imaging technique that can be used for breast cancer detection)
SVM	Support Vector Machines (machine learning method to model a system)
TSAR	Tissue Sensing Adaptive Radar (microwave breast imaging system developed by Fear et al. [1, 2])
TX	Transmitter (referred to an antenna or a path of RF switching matrix)
TWTLA	Traveling Wave Tapered and Loaded Antenna (type of antennas applied in the experimental system [3])
UWB	Ultrawide-Band (frequency region from 3.1 to 10.6 GHz)

Chapter 1

Introduction

1.1 Rationale and objectives

Breast cancer remains one of the deadliest diseases in Canada and worldwide. According to the Canadian Cancer Society [4], there are estimated 25,000 new incidences and 5,000 deaths in 2015. US statistics quote expected 232,000 new cases and 40,000 deaths in the same year [5]. The most efficient countermeasure against breast cancer is to detect new lesions at early stages, which greatly increases the chance of recovery.

During the past fifty years, X-ray mammography has been the standard clinical screening technique [6]. However, the limitations of the X-ray mammography are well recognized. First, it yields high false-positive detection rate, especially on patients with dense breasts; second, it exposes patients to ionizing radiation; third, it requires painful breast compression [7].

Many efforts have been made to overcome these limitations using different technologies. For example, ultrasound imaging is a quick diagnostic tool that could be used for mass screening purposes due to its non-ionizing nature. However, ultrasound suffers from several shortcomings. First, it fails to distinguish between malignant and benign tumors, second, it often misses microcalcifications due to the "speckle" phenomenon and, third, it has high operator dependency in interpretation of the results. Magnetic Resonance Imaging (MRI) provides high tumor detection sensitivity [8]. However, it is a complex and expensive method, usually requiring use of contrast agents. Therefore, it is not applicable for mass-

screening.

It is worthwhile to mention that all the three clinical modalities mentioned above prove to be an effective tool when used together [9]. However, in practice, their application is limited to the cases when the cancer has already developed to its later stages. This motivates a continuous search for new techniques to effectively detect tumors early.

One of the novel methods for early breast cancer detection is microwave imaging. The method is based on the difference in dielectric properties between malignant and benign tissues. Studies of dielectric properties of human tissues in the microwave frequency range [10–12] demonstrate that the contrast between malignant and benign tissue reaches 10 times in dielectric permittivity and conductivity. MWI is non-ionizing and does not require such expensive hardware as MRI scanners. This enables low-cost equipment, safe for frequent scans of one patient, thereby potentially enabling mass screening [13].

One approach of microwave imaging is a time-domain Ultra**w**ide-Band (UWB) Micro**w**ave Radar (MWR), which is the focus of our research group at McGill University, guided by Prof. Milica Popović. Several challenges are related to the breast MWI in general and, in particular, to the UWB time-domain breast imaging.

First, Electro**m**agnetic (EM) waves with wavelength of several centimeters in breast tissues, physically limit high imaging resolution. Next, highly heterogeneous and dense breasts result in signals with a lot of clutter, i.e. reflections from normal tissues, surrounding a possible tumor. In addition to the physical limitations, there is a significant challenge in the time-domain data acquisition for the MWR method. Currently available inexpensive microwave samplers suffer from noise, most significant of which is phase noise. Finally, MWI algorithms currently represented in the literature are very computationally expensive, requiring high-performance computational clusters for three-dimensional MWI in order to build one image in a time-frame of approximately an hour. Thus, algorithms for the MWR method require optimization and improvement to decrease the cost of equipment and to reduce imaging time.

The research work presented in this thesis is directed to address the challenges described above. In particular, the studies described further pursue the following goals:

1. Combine signals collected by two methods - MWR and Micro**w**ave-Induced Thermoacoustics (MWIT) in order to improve imaging performance. Within this

study the following milestones have been considered:

- Develop optimal data fusion rule for MWR and MWIT signals;
- Derive expressions to compute hypothesis test statistics and their noise distributions for setting tumor detection thresholds;
- Implement and evaluate the performance of the dual-modality detection algorithm, based on the simulated datasets.

2. Develop a method to compensate phase uncertainty in the microwave sampler by using software algorithms.
   - Propose a method to reduce uncertainties in the microwave sampler;
   - Develop an accurate method of phase delay estimation between "step"-like signals;
   - Statistically evaluate the method using experimental signals.
3. Improve performance of microwave imaging algorithms.
   - Compare existing microwave imaging algorithms using simulated datasets with variable parameters: levels of heterogeneity and contrast;
   - Optimize the existing Delay-Multiply-And-Sum (DMAS) algorithm to improve computational performance;
   - Develop a frequency-domain counterpart of the existing Delay-And-Sum (DAS) algorithm to improve both computational performance and image quality.

1.2 Thesis outline

The rest of the thesis is organized as follows.

Chapter 2 provides a literature review of breast cancer imaging and detection, with special emphasis on the current research in the area of microwave imaging.

Chapter 3 presents the theoretical background, required for further chapters. Imaging problem is formulated and methods for signal acquisition and pre-processing are described.

Next, the chapter summarizes essential models of EM signal propagation. The rest of the chapter is dedicated to the description of MWI algorithms.

Chapter 4 presents the methodology of signal fusion from two microwave breast imaging modalities - MWR and MWIT and discusses the results of the application of this technique to numerically simulated data.

The first part of *Chapter 5* is dedicated to the design of the experimental data-acquisition system. The second part of the chapter describes the methodology of phase uncertainty compensation for time-domain data acquisition.

The purpose of *Chapter 6* is two-fold. First, several existing imaging algorithms are evaluated using numerically simulated datasets. Next, the chapter presents the Delay-And-Sum algorithm in the **f**requency domain (DASf) and an **o**ptimized version of the Delay-Multiply-And-Sum algorithm (DMASo). Finally, the chapter closes with a discussion of the advantages of the two proposed algorithms.

Chapter 7 concludes this thesis and presents suggestions for future work.

Chapter 2

Literature review

The non-invasive breast cancer detection techniques were first introduced with X-ray imaging in 1960s [6]. Since that time, X-ray breast imaging has been accepted as a clinical technique and took the name "mammography". Several new techniques, such as ultrasound and MRI, were introduced into breast imaging later.

The goals of breast cancer detection and diagnosis include:

a) improved performance in terms of: detection of tumors - i.e., the ability to correctly identify their presence at earliest stages; localization - the ability to correctly determine spatial location of tumors and their spread; characterization of abnormal masses, most importantly, determining if they are malignant or benign tissues;

b) improved convenience for patients - eliminate safety risks (X-ray radiation dose, etc.); lower patient discomfort (e.g. breast compression, injection of bio-markers); improvement in data acquisition time;

c) cost reduction, so that the screenings can be regular and can cover a higher percentage of the population.

So far, no technique has met all the described criteria simultaneously. This chapter describes the fundamentals of breast cancer and techniques for its detection and diagnosis.

2.1 Anatomy and pathology of female breast

The anatomy of an adult female breast is shown in Fig. 2.1. Milk glands, consisting of small lobules, produce and store milk. Ducts act as channels to release milk from the breast. Fatty tissues surround the glandular network.

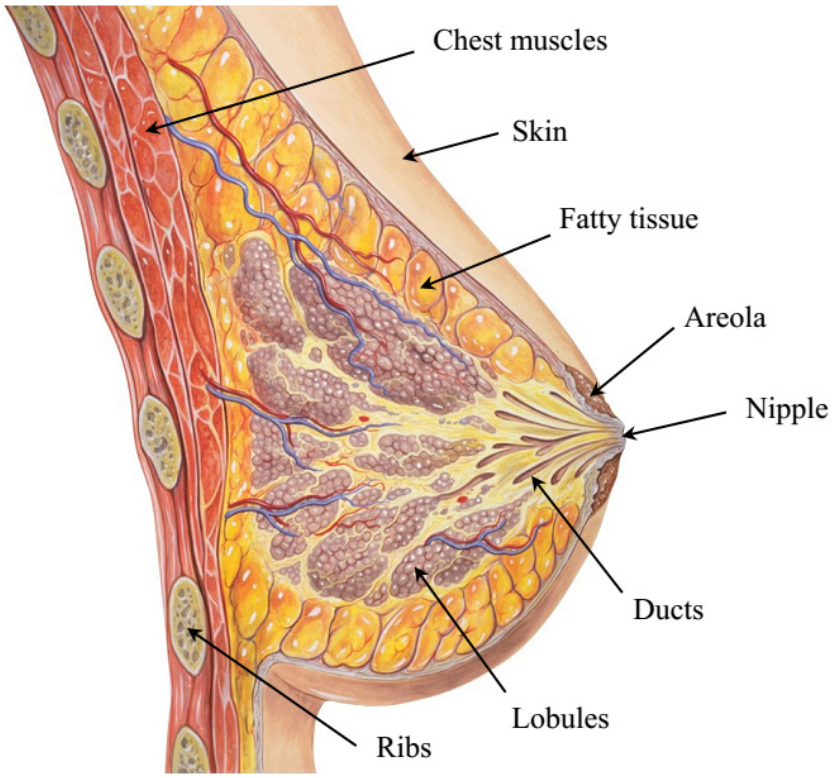

Fig. 2.1 Illustration of the anatomy of female breast (modified image, original image by Patrick J. Lynch available at http://coastfieldguides.com/).

Glandular tissues of the breast are soft and prone to the genesis of tumors of different kinds. Breast cancer can develop both in lobules and in ducts: Lobular Carcinoma In Situ (LCIS) - tumorous mass within a lobule; Ductal Carcinoma In Situ (DCIS) - tumorous mass inside a duct. With further progress, the tumor expands into the glandular tissues, resulting in Invasive Lobular Carcinoma (ILC) and Invasive Ductal Carcinoma (IDC) [7]. At later stages cancerous cells start to penetrate into blood vessels and spread throughout the whole body (metastasis) [14].

The symptoms of breast cancer include breast irritation, swellings, palpable lumps of

irregular shape, breast or nipple pain [14]. These symptoms usually appear only at later stages of cancer development, when the tumor becomes larger in size and occupies more breast tissues. Thus, it is essential to maximize the detection of asymptomatic cancer as early as possible.

2.2 A summary of clinical methods for breast cancer detection and diagnosis

Clinical methods for breast cancer detection have to be approved by relevant governmental bodies, e.g. in the United States, the Food and Drug Administration (FDA). Detection of breast cancer starts with screening, with the goal to detect any anomalies in the breast [9]. The requirement for screening techniques is high sensitivity, i.e. the ability to correctly identify those women who have cancer. In a clinical environment the process usually starts with clinical breast exam, which involves palpation - a procedure performed by a doctor or other health professional to detect tumors based on hand tactile feeling [15]. Palpation, being the quickest and easiest technique, can detect only large late-stage lesions inside the breast, which can rarely be treated effectively [6]. In order to detect small, non-palpable, lesions, non-invasive imaging techniques have been developed. X-ray mammography currently provides the best trade-off between sensitivity and cost. Whenever any suspicious lesions are detected, the patient is recommended for further analysis, to characterize the found abnormalities and finalize the diagnosis. Additional imaging methods, such as MRI and ultrasound may be involved at this stage, helping to diagnose and localize the lesions. The requirement for the diagnostic techniques is high specificity, i.e. the ability to correctly identify those women who do not have cancer [9].

Finally, the ultimate diagnosis about the suspicious already imaged lesion can be given by biopsy - the procedure where a small amount of breast tissue is extracted and biochemical analysis is performed to characterize the cell structure. Imaging methods, such as ultrasound, are often used to guide the needle to the correct place for tissue extraction [16]. Since biopsy is invasive and creates discomfort to patients, efforts are usually made to avoid or minimize its usage.

2.2.1 Notes on terminology

Throughout this thesis, the term "Imaging" is used for any kind of technique producing an image at the output. The term "detection" is used to assume a process or its result, that answers a yes/no question if a tumor is present in a breast. Examples of the detection techniques can be found among machine learning methods that draw a conclusion by analyzing input signals directly, based on hidden logical reasoning. On the other hand, term "detection method" might be applied to an imaging method when it is assumed that the detection step is applied after generating an image - this can be either an automated image analysis algorithm (e.g., thresholding) or traditional analysis by a trained radiologist.

2.2.2 X-ray methods

Mammography

Since the 1960s X-ray mammography (or just "mammography") has been utilized as the main clinical routine screening and diagnostic technique [17].

From the imaging perspective, mammography is a transmission-type method. Similar to bone radiography, mammography utilizes X-rays that are radiated through a breast and then recorded at the opposite side to get an image of dense objects inside the soft tissues. Microcalcifications [18], usually linked to breast cancer, can be detected and localized by trained radiologists.

Mammography screening requires a breast to be compressed between two plates while a patient is standing in front of a mammographic machine. The compression helps reduce the minimum needed radiation dose, which is achieved by reducing the attenuation of X-rays in the thinner lossy medium. Moreover, compression helps reduce the superposition of healthy heterogeneous tissues by spreading the volume of the breast to a larger area exposed to X-rays [6].

X-ray mammography has clearly identified downsides [7]. First, it provides high false-positive detection rate, especially on patients with dense breasts; second, it exposes patients to ionizing radiation, limiting its frequency of usage to annual exams; third, it requires painful breast compression [15].

Digital mammography

Digital mammography does not have greatly improved performance in terms of the detection/diagnostic capability in comparison with traditional mammography [19]. However, it has enabled the application of computer-aided detection and improved storage and management of images [7]. For a long time it has been a technological challenge for digital mammography to be compared with conventional film mammography from imaging resolution perspective. In order to reach a resolution comparable with conventional mammography, digital mammography requires a sensor matrix with over 100 Megapixels, a challenge which has been overcome only recently [20].

Digital breast tomosynthesis (DBT)

The clinical setup for breast tomosynthesis is close to mammography except that the transmitter moves along a limited arc over the compressed breast and several X-ray shots are taken [20]. These images are then used by reconstruction algorithms to represent a three-dimensional view of the breast. The reconstruction is performed by algorithms similar to those used in Computed Tomography (CT), such as filtered back projection [21, 22]. However, the reconstruction quality is limited in DBT compared to that given by the CT, since the shots are made from only a limited arc of the transmitter path. The reconstructed three-dimensional view helps better understand the structure of the breast and differentiate malignant lesions from surrounding benign tissues. The radiation dose used in DBT is usually comparable to mammography. DBT technology is being introduced into clinical screening [23]. Several commercial FDA-approved scanners are already available on the market [24]. Studies that compare mammography with DBT report a significant increase in performance when DBT is used in addition to mammography [23, 25]. At the same time, applying two X-ray imaging methods simultaneously inevitably increases the radiation dose. Some studies claim that performance increase of DBT over mammography is not convincing [25]. When used alone, DBT has reported problems in the detection of microcalcifications [26], which is essential for a successful breast screening modality. Currently, DBT is still under evaluation and is in the development stage. In clinical environment it helps resolve complex structures seen on mammography to avoid unneeded patient recalls [23].

2.2.3 Ultrasound breast imaging

During ultrasound breast scanning, the patient lies in a supine position and the operator moves an ultrasound transducer probe over the breast to obtain an image, which is updated on a screen in real-time [18]. The images display an ultrasound echo profile of the tissues under the probe. Dark areas represent tissues with higher water content, where attenuation is high, often highlighting benign cysts inside the breast.

When used alone, ultrasound cannot detect microcalcifications and solid masses due to the "speckle" phenomenon [6], which is prohibitive for a screening modality. In addition, ultrasound imaging is too operator-dependent. On the other hand, ultrasound is an indispensable adjunct to mammography to characterize soft masses. It has proven to eliminate many unneeded biopsies after X-ray mammography had previously identified a suspicious mass. As ultrasound is non-ionizing, it gives the advantage to an operator to make as many scans as needed. Offering the capability of real-time imaging, ultrasound is beneficial for guiding needle biopsies, after the tumor has been detected by mammography or MRI [16].

2.2.4 Magnetic resonance imaging

In general, Magnetic Resonance Imaging (MRI) is a risk-free imaging technique to obtain high-resolution high-contrast anatomic images of interior structures of a human body. It is based on the principle of nuclear magnetic resonance. Magnetic momentum of spin systems (protons) interact with externally applied EM radiation - when an EM pulse stimulates the spins, they react by generating echo signals. The echo signals are different depending on the material that the echoes come from. The recorded echo signals are picked up and processed by image reconstruction algorithms to generate images that correlate with the spatial distribution of the material under analysis [27].

During breast scanning a patient is lying inside the MRI scanner in a supine position. Strong magnetic fields are generated by magnets in the tube. There is an inner layer of Radio Frequency (RF) coils that generate EM pulses and record the echo response from the patient.

MRI has been used for breast cancer imaging since the 1980s, after a specialized RF coil

for breast MRI was developed [28]. The main advantages of MRI over mammography are as follows: *a*) very high sensitivity (reported values as high as 100% [29]), *b*) non-ionizing nature of the method and *c*) no need for breast compression.

The disadvantages of MRI are that it is very expensive, time-consuming and used for breast screening mostly with contrast agents [30]. In addition, MRI struggles to distinguish malignant and benign lesions [31].

MRI is used mostly as an adjunct technique for characterization of tumors and their spread analysis when they are detected by mammography. In addition, MRI is applied to clarify obscure mammography and ultrasound images, as well as in the neoadjuvant treatment and post-operative assessment [8].

2.3 Alternative methods for breast cancer detection

Numerous alternative and/or complementary imaging modalities have been introduced during the past years. These methods are based on the contrast between malignant and benign breast tissues in their mechanical, thermal, acoustic and/or electromagnetic properties. Some of these methods are currently in the evaluation stage and have not yet received FDA approval. Others experience difficulties or limitations, which currently question their application in breast cancer detection.

Further in this section a summary of alternative breast imaging methods is provided. A comprehensive recent review of the imaging modalities in comparison with the current clinical methods is available in [32, 33].

Thermography

This is a passive method that records and analyzes infrared radiation generated by the human body. Abnormalities in the form of increased skin temperature in the areas adjacent to the underlying cancerous zones can be detected in the images from an infrared camera [34]. This technique was promising in 1970s, but was not efficient [35, 36]. Interest in this technology has increased after technological advancement, which enabled efficient measurement and recognition of energy patterns in the microwave region. Since microwaves exhibit much higher penetration ability in the human body than

infrared radiation, they can carry information from much deeper breast regions [37]. The continuation of development has been seen in microwave radiometry [38]. The first microwave radiometer for breast screening purposes was FDA-approved in 1999 [39].

Solutions involving ionizing techniques

Computed Tomography (CT), another widely spread clinical X-ray-based method of whole-body imaging, rarely used for breast cancer screening and considered as an adjunct to mammography [6, 15]. There are several reasons behind this. First, the radiation dose required by CT is too high and is a prohibitive factor for screening purposes. Second, CT has not proven to yield higher breast cancer detection rates. Although it provides a three-dimensional image of the breast and helps eliminate the artifacts associated with superposition of breast tissues (present in mammography), the resolution of CT is much lower than that of film mammography [40]. Third, CT can only detect small microcalcifications with the help of intravenous injection of iodide [41].

Positron-Emission Tomography (PET) [42] and scintimammography [6] - techniques that use radioactive tracers that concentrate in tumorous areas. The radiation of the tracers around tumors can be seen by PET or Single-Photon Emission Computed Tomography (SPECT) scanners. The injection of the tracers is invasive and more expensive than ultrasound and mammography. These methods are not considered to be safe for pregnant women.

Active infrared and near-infrared imaging

Application of light in infrared and near-infrared range for breast cancer detection started from transillumination (also known as light scanning, or diaphanography). This is a technique that uses transmission of red and near infrared light through the breast [42]. Transillumination is based on the preferential absorption of the light in breast tumors due to increased amount of blood in the neovascular network. Later studies have shown that this method is inefficient in comparison to mammography and other methods. Studies of near-infrared techniques continue in the form of Near Infrared Spectroscopy (NIS) [43]. NIS targets to tomographically reconstruct optical properties of breast tissues by using such techniques as diffuse optical tomography [33, 44]. This method has been proposed

for use in combination with other modalities, such as MRI [45]. Studies of NIS are still in progress and it has not yet been accepted as a clinical technique.

Electrical impedance techniques

These methods are proposed to detect tumors based on the decreased impedance of malignant tissues over benign. Electric Impedance Tomography (EIT), also known as Electrical Impedance Spectroscopy (EIS), is a method that aims to reconstruct dielectric properties of breast tissue, based on impedance measurements in low-frequency range (< 1 MHz). To accomplish this task, low currents (microamps to milliamps) are run through the breast with several electrodes applied at various locations on the breast skin [43]. Although this technique has not yet demonstrated vast clinical applicability, promising results have been reported in [46, 47] and new algorithmic machinery to reconstruct the EIT images is under development [48]. Electric Impedance Mapping (EIM) method does not aim at reconstructing the whole breast conductivity profile. Instead, it measures bulk impedance under the electrodes [49]. Although this method does not offer high specificity, limits penetration depth of measurements and lacks localization information for biopsy [49], it has been suggested that it is applicable as an adjunct technique to mammography: the first commercially available EIM scanner got a pre-market FDA approval in 1999 [6].

Hybrid methods

Several methods take advantage of using more than one physical principle to detect breast cancer. The photoacoustic imaging technique employs optical and radio frequency waves to illuminate the breast and receive ultrasound signals, induced by the selective absorption of these waves inside malignant and normal tissues [50]. Acoustic waves can be induced by microwave radiation - this approach is known as Micro**w**ave-Induced Thermoacoustics (MWIT), which is described later in this chapter.

Another form of joint acoustic and microwave detection methods is described in [51]. The proposed idea suggests using acoustic signals to modulate the microwave response. The "Doppler" effect in microwave backscattered signal depends on the elastic properties of the tissues and the amplitude of the scattered signals at the fundamental microwave frequency

depends on the dielectric properties of the tissue.

Finally, elastography, also a hybrid technique, seeks to identify suspicious masses based on their mechanical elasticity. Elasticity is measured indirectly, via other physical properties, such as acoustic (ultrasound elastography [52]) or electromagnetic (magnetic resonance elastography [43]).

2.4 Active microwave breast cancer detection

Similar to electrical impedance described earlier, MWI is based on a significant contrast in dielectric properties ("dielectric contrast") between malignant and healthy tissues. During the active MWI procedure, the breast is illuminated with low-power microwaves and the response is processed and analyzed to detect the difference in the dielectric properties of breast tissues in the microwave spectrum. The dielectric contrast between the tissues can be used to detect the areas inside the breast with abnormalities.

Several studies report on measurement of dielectric properties of breast tissue. In 1988 Surowiec et al. published results of their measurements of breast dielectric properties [53] in the range 10 kHz - 100 MHz. According to their data, the ratio between malignant and normal breast tissues reaches 10:1 in both permittivity and conductivity. However, no differentiation between glandular and adipose tissues is made in this study. Another set of measurements of biological tissues by Joines et al., conducted six years later, extended the frequency range to 50 - 900 MHz [54]. Their results report the dielectric contrast of approximately 4:1 in permittivity and about 6:1 in conductivity. Further studies [10–12, 55, 56] report consistent values and extend the frequency range up to 20 GHz. In these studies it has been determined that malignant tissues possess more water, which increases both their conductivity and permittivity.

A later large-scale study of breast specimens obtained from cancer surgeries by Lazebnik et al. in 2007 [57] confirmed the previously measured 10:1 dielectric contrast only between tumorous and adipose tissues: it is reported that the measured contrast of glandular tissues with respect to the tumor tissues hardly reaches 10%.

A study to compare the dielectric properties of the breast specimens in the frequency range of 100 Hz - 8.5 GHz, measured *in vivo* with those measured *ex vivo*, is conducted by

Halter et al. in [58]. The study demonstrates significant decrease in both conductivity and permittivity of *ex vivo* samples compared to the *in vivo* measurements.

Further analysis of the tissue structures with cancer cells was performed by Sugitani et al. [59]. It is reported in the publication that the proportion of the cancer cells in the tissue is correlated with the measured conductivity and permittivity of the specimens in the range of 1 - 6 GHz.

Since the onset of breast cancer most often happens within ducts and lobules (LCIS/DCIS) - the dielectric contrast between tumors and surrounding tissues (glandular tissues) is not as high as when the tumor spreads and touches the adipose tissues. This fact suggests that detecting tumors at an earlier stage might be much more challenging than initially anticipated - not only because of the tumor size itself, but also because of the reduced dielectric contrast. This conclusion is especially relevant for the time-domain UWB radar approach since most image of the reconstruction techniques are based on the reflectivity from scatterers inside the breast.

Despite the fact of the reported low contrast, active MWI is still encouraging for several reasons. First, the 10% value of dielectric contrast is still higher for microwave imaging compared to existing clinical methods, e.g. mammography (2%) and ultrasound (under 10%) [60]. Second, it is argued [58] that the measurements in [57] might not reflect the true values of the tissues since the samples were analyzed *ex vivo*, several minutes after their extraction.

Breast tissue attenuates microwaves, which limits their penetration (but still does not prohibit tumor detection). According to the analysis in [61], average attenuation of breast tissues is less than 4 dB/cm up to 10 GHz. This allows for microwaves to penetrate the tissue up to 10 cm from the skin surface, with their backscatter still detectable at the surface of the breast.

The female breast is structurally heterogeneous. This complex environment challenges the analysis of microwave propagation inside the breast since EM waves experience multiple-scattering. As a result, one cannot make a simplifying assumption about tissue homogeneity, often an enabling factor for imaging algorithms; in addition, multiple reflections between surrounding tissues and tumors that exist in the recorded signals further complicate the analysis of the signals by masking the direct reflections from the

tumors.

Finally, breast tissues are dispersive [10–12, 55–58], i.e. their properties are frequency-dependent. This must be taken into account when evaluating wide-band wave propagation through the tissues.

2.4.1 Microwave tomography

Microwave Tomography (MT) aims to reconstruct dielectric properties of the whole domain of a biological specimen, one cross-sectional slice at a time. The first application of MT was described by Larsen and Jacobi [60], who successfully reconstructed an image of a canine kidney. MT images are built by solving an inverse-scattering problem of EM propagation and scattering. This is accomplished by fitting an EM model to the recorded data, by iterative adjustment of the unknown parameters of the model, which are the dielectric properties of the propagation environment (the biological specimen). Several reconstruction algorithms have been proposed, which include methods based on Born linearization techniques [62, 63] as well as those based on shape functions [64].

The inverse problem requires multiple iterations of forward modeling, which are usually computationally expensive. Various computational techniques are employed, such as Finite-Difference Time-Domain (FDTD), Method Of Moments (MOM) and method of Finite Elements (FE). In addition, the problem is often ill-posed, possibly resulting in multiple solutions and instability of results (when slight variation in recorded data might result in completely different reconstructed images).

Several experimental systems have been built and clinically tested [65, 66]. Major problems associated with microwave tomography are the very high computational complexity of the image reconstruction algorithms and the low quality of the images due to the ill-posed imaging problem.

2.4.2 Microwave-induced thermoacoustics

Microwave-induced thermoacoustics (MWIT) is a hybrid technique which employs microwaves to illuminate the breast and to receive the thermally-induced acoustic, rather than microwave, response signals. The principle of MWIT is based on higher EM signal

absorption rate by the malignant tumors as compared to that by the normal tissue. When illuminated by short microwave pulses, the differential heating of tumors results in their rapid micro-shrinkage and expansion. These size vibrations produce ultrasound signals, which are recorded by acoustic sensors and analyzed for the presence of tumors [67].

In contrast to microwaves, acoustic waves have shorter wave lengths, which potentially leads to higher spatial resolution. In breast imaging, MWIT method is mostly represented by works of Kruger et al. [68] with a demonstrated experimental system. However, recent studies report that the images produced by the MWIT are hard to interpret due to the multiple physical processes involved in the origin of the acoustic signals. Further, the implementation of the MWIT for breast cancer detection requires uniform breast heating, which is a non-trivial task. Increasing the system complexity would result in its higher cost, which would ruin the initial positioning of this microwave method as a good candidate for mass-screening.

Hybrid imaging techniques involving the analysis of both acoustic and microwave response signals are under investigation. Our research group has studied the application of MWIT for breast cancer imaging. We proposed in [69] to combine this method with the UWB microwave radar to increase the signal-to-noise ratio of the resulting images. Due to increased amount of information coming from two different physical phenomena, this combination may provide significant improvement, as it is further elaborated in chapter 4.

2.5 Ultrawide-band time-domain microwave radar

In the late 1990s, a group at Northwestern University investigated the UWB radar method to detect breast cancer [61, 70]. What differentiates UWB radar from MT is that, instead of reconstructing the dielectric profile of the breast, UWB radar images spatial distribution of scattering intensity, which is based on the contrast between tissue properties rather than on their absolute values. Significant dielectric contrast between malignant and benign breast tissues creates dielectric interfaces in the tissues, which produce back-scattered reflections when an impulse propagates within the breast. UWB radar imaging algorithms make an assumption of linear propagation. This approach significantly reduces the algorithmic complexity because radar-based methods do not rely on inverse-scattering reconstruction. In addition, the bandwidth of the UWB radar might offer higher spatial resolution compared

to MT.

Time-domain UWB radar requires rather simple hardware. The associated computationally-efficient image-formation algorithms dramatically decrease its cost. It is therefore a viable candidate for a mass-screening tool.

The rest of this chapter describes essential aspects of UWB time-domain radar, such as data acquisition systems with their elements, as well as numerical simulations, data pre-processing and imaging algorithms.

2.5.1 Data acquisition

An example of a typical UWB radar data acquisition system design is illustrated in Fig. 2.2. The system consists of a radome with a matching medium, where a breast is placed for analysis. A pulse generator produces UWB pulses that are sent through antenna TX. The response is picked up by antenna RX and sampled by a receiver. In practice, usually more than one antenna is used at both transmitting and receiving sides. In this case a switching mechanism has to be implemented to switch between antennas. A controller is responsible for the supervision of the data collection. The collected signals are pre-processed and an imaging algorithm is applied. The resulting images are visualized on a display.

Antenna arrays and elements

In order to maximize the amount of collected information, the breast is usually illuminated from multiple locations to collect an array of signals. This can be accomplished in several ways. First, only one antenna can be used for scanning around the breast [71]. This kind of signal acquisition is known as synthetic monostatic array - the signals are transmitted by the same moving antenna ("synthetic"), which is used both as a transmitter and as a receiver of the microwave signals ("monostatic"). When more than one antenna is used, bistatic or multistatic arrays are formed: when one antenna transmits, others record the response. Multistatic arrays [72–74] can be implemented as either a synthetic array by using only two independently moving antennas or as a real array - with many spatially fixed antennas. Synthetic monostatic arrays are convenient in terms of RF implementation. They require only one antenna without any RF switching mechanism involved. Another advantage is

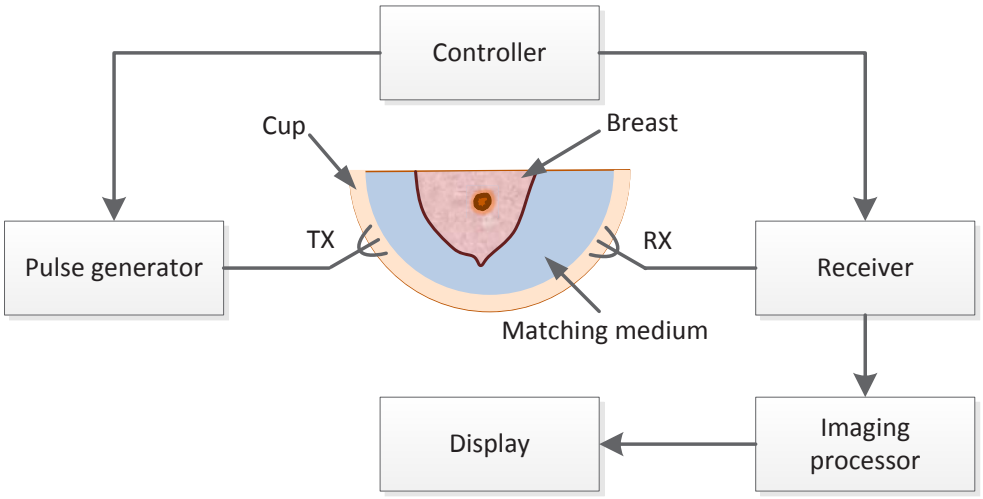

Fig. 2.2 Typical data acquisition system for ultrawide-band time-domain radar.

that the number of collected signals can be easily configured in software. At the same time, the downsides of this configuration are: complex mechanical system for antenna movement, increased data acquisition time and limited collected information compared to the multistatic arrangement.

In terms of data acquisition locations, several types of antenna arrays have been considered. For a clinical setup when a patient lies in a supine position, conformal and planar antenna arrays have been used in most cases [75–77]. This design does not require the usage of a matching medium since the antennas can be positioned as close to the breast as needed. Consistent distance between the skin and the antennas also helps in terms of signal pre-processing, e.g. skin artifact removal, as further discussed in this chapter. However, when the antenna layout can conform to the breast, their locations are not accurately known with respect to each other for varying breast shapes. In addition, small variations in the antenna-skin distance can cause big variations in antenna performance, as predicted by antenna theory for antennas placed on or very close to an interface of two dielectrics.

In practice, arrays with fixed locations are used most often. Fear et al. [1, 2] use a cylindrical synthetic aperture array in their Tissue Sensing Adaptive Radar (TSAR) system; Craddock

et al. have developed a hemispherical array and implemented it in their experimental system [73]. A hemispherical array is also used in the experimental system of our research group[72].

More advanced antenna arrays are also considered, such as a rotating planar array, described in [78], conformal array based on aspiration [74], which adjusts the breast to the hemisphere by using air suction.

An essential part of a data acquisition system is the antenna element. Antennas in UWB radar usually act as both receivers and transmitters. There are several criteria for antenna design to use in the UWB radar breast imaging. First, antennas have to be compact in order to fit in the area around the breast. Second, antennas need to efficiently operate in a chosen frequency range (for UWB radar, 500 MHz - 10 GHz). Third, antennas need to operate in the near-field region and have a specific radiation patterns. Fourth, antennas should be optimized to work with a particular coupling medium.

Numerous antenna designs have been evaluated for microwave breast cancer detection, such as resistively loaded bow-tie antennas [1, 79–81], horn antennas [76, 82, 83], Vivaldi antennas [84], Vee dipoles [1], Wu-King monopoles [2], patch antennas [85] and custom designs [3, 86].

Matching medium

In order to better couple antennas to the breast tissues and reduce excessive energy scattering from the breast skin, a special matching medium usually fills the gap between the antennas and the breast. The matching medium is a liquid substance, such as oil or gel, in which the breast and antennas are immersed while the breast scanning procedure is performed. The most common consideration for choosing a matching medium is to provide a permittivity value close to those of the skin and antennas and, at the same time, to lower the conductivity in order to reduce losses in this medium as much as possible. For example, [87] describes immersion liquids tests and suggests that oil-based liquids provide better permittivity coupling. Work by Zhou et al. [88] proposes to use ethanol, which well matches the results of numerical simulations presented in [89].

In the work described in this thesis, ultrasound gel was used as the best option among the commercially available clinically-approved materials. The dielectric properties of the

ultrasound gel in the UWB range [90] are close to those of the breast skin, which provides a good coupling between the antennas and the breast.

Frequency range and pulse shape

Another important factor for time-domain UWB radar is the excitation signal. First, the RF pulse should occupy a frequency range wide enough to optimize the imaging resolution (i.e., the pulse width should be minimized). Second, the energy of the radiated pulse should be sufficient to propagate to the tumor and back with acceptable attenuation and should be limited by safety regulations [91–93]. Third, pulse shape should be consistent with the characteristics of the antennas that are used to radiate and receive the feedback.

Several types of pulses have been considered for use in UWB microwave radar systems for breast cancer detection. The most commonly used excitation signal is a Gaussian pulse [94–96]. Gaussian pulse generation is implemented in numerous microwave pulse generators. Parametric Gaussian pulses are beneficial in advanced signal processing algorithms, such as the wavelet transform [97]. Modulated Hermite pulses are studied for use in UWB breast cancer imaging [98]. The work of this thesis uses a custom-synthesized broadband reflector pulse shaping filter structure in order to generate a pulse that spans the range of 2 - 4 GHz with maximum efficiency [99].

Microwave receiver

After a receiving antenna records the backscattered signal, the signal has to be digitized for further processing. This is an essential step that has been a bottleneck for many years for practical applications of UWB breast time-domain radar.

In general, there are two ways of acquiring UWB data from the system: *a*) sampling the response from a transmitted UWB pulse (time-domain acquisition); and *b*) acquiring a frequency response of the system in the range of interest and then using this data to synthesize the response from a particular pulse (frequency-domain acquisition). The time-domain method is considered to be used in practice in the final device since it offers faster data acquisition than the frequency-domain method and can reduce the cost of the sampler by taking advantage of equivalent-time sampling techniques [100, 101]. The

frequency-domain method is mostly used in research environments due to the following advantages: *a*) VNAs with high dynamic range are available as standalone devices; *b*) frequency-domain data is more beneficial than sampled time-domain reflections since it allows to model the response from virtually any type of excitation pulse (under the assumption of system linearity).

Numerical simulations and breast models

Numerical simulations are largely used to synthesize data in the area of UWB microwave imaging. The breast model is constructed and provided as an input to a computational engine that simulates the excitation and propagation of EM waves in space and time and computes EM fields for further evaluation.

At early stages of system development, the simulations are essential for feasibility assessment. Simulations help design and optimize components of an experimental system, such as the matching medium or antennas. The simulated UWB signals provide a means of developing imaging algorithms without building actual equipment. Simulated data is also beneficial for the statistical evaluation of algorithms under one varying factor with all other factors fixed (which is often impossible in practice).

Two essential elements of any numerical model for breast cancer detection are the breast model and the antenna models. The breast can be modeled with a simplified surface as a regular hemisphere or ellipsoid and with a realistic anatomical shape. For realistic modeling, usually MRI images are used to derive the surface and internal structures, e.g. [102], [103]. Recent EM solvers allow dispersive materials to be introduced into the simulation in terms of Debye, Cole-Cole or other dispersive models. Antenna modeling has its challenges: thin structures (which are usually resistive and conductive layers in antenna design) require a very fine spatial grid, which results in a very high number of cells in the model. This can easily make the simulation prohibitively large.

Nowadays a number of commercial full-wave EM simulation packages are available, such as CST Microwave Studio [104], SEMCAD by SPEAG [105], ANSYS High Frequency Structure Simulator package (HFSS) [106] as well as COMSOL Multiphysics [107]. Such numerical methods as FDTD, FE and MOM are used in order to solve space-time Maxwell's equations in two-dimensional and three-dimensional environments.

In order to validate simulated investigations in practice, numerical simulations are usually followed by experimental trials that involve breast-mimicking phantoms [108–112].

2.5.2 Signal pre-processing

Before imaging algorithms can be applied to the collected signals they need to be pre-processed to remove artifacts, compensate for antenna performance, band-pass filter and remove other types of measurement noise. At the signal pre-processing stage other parameters can be estimated, such as breast shape or average dielectric properties.

Calibration

Antennas can be used both to transmit and receive feedback signals. It is crucial to separate incident antenna pulses from scattered signals in time. In order to remove this initial pulse, a calibration procedure is performed. It consists in the subtraction of a calibration signal from the received signals. The calibration signal is acquired by transmitting and recording the waveforms without the breast exposed to the illumination. Besides the incident antenna reflection, this procedure also reduces the effects of coupling between adjacent antenna elements.

Breast properties estimation

Most imaging modalities require certain parameters to be known prior to the application of the algorithms. These include breast shape, skin thickness and average dielectric parameters of the internal structures. Simulated experiments usually assume these parameters are known. However, in reality they need to be estimated.

Works by Winters et al. [113] and Williams et al. [114–117] propose algorithms to estimate skin surface by preliminary breast scanning and making use of skin reflection. The problem of breast surface identification is also addressed in [118] when the application of planar antenna array for a hemispherical breast model is considered.

Skin thickness estimation is discussed in [1]. The authors of the study propose a method to estimate thickness based on the difference in alignment between two skin cylinder

reflections. Preliminary dielectric properties estimation is discussed in works by Winters et al. in [119–121].

Skin-breast artifact removal

One of the challenges at the signal processing stage is to remove the skin-breast artifact in the received signal. This interference is caused by a high-contrast dielectric interface between skin and inner breast tissues and is aggravated by a not completely compensated matching-medium-to-skin interface.

Several approaches for skin artifact removal have been proposed. First, when planar or cylindrical breast models are used, the artifact in each channel is identical. A simple averaging algorithm [94] can be used to estimate the artifact response and to subsequently subtract the average from each channel. This approach is applicable only in cases when antennas are positioned at equal distances from the regularly-shaped breast.

An algorithm proposed by Bond et al. in [75], applies Wiener filtering to the signals that estimates skin reflection as a filtered combination of the signals. This efficiently compensates for a time mismatch of the skin artifacts between the channels. This method has been applied in many works and has been extended for a multistatic setting in [122].

Another approach proposed by Sill et al. [2] applies the Recursive Least Squares (RLS) algorithm, adapted from a beamformer approach with the combination of Woody averaging [71]. In comparison to Bond's method, it iteratively searches for weighting coefficients which change in time.

An entropy-based time window approach for skin-breast artifact removal is proposed by Zhi et al. in [123]. This algorithm searches for a maximum entropy in the signals to localize the dominant skin reflections.

An algorithm proposed by Maskooki et al. [124] addresses the problem of skin reflection compensation by decomposing the received signals in frequency domain into complex exponentials, which describe the responses from most significant scatterers. It is assumed that the largest components represent skin reflections, which are removed after the decomposition.

The described methods vary in their applicability to different breast shapes and antenna

placement. So far, no solution has been proposed to remove the reflection from a realistic irregular three-dimensional breast shape for a scenario when antennas are placed at a distance of several centimeters from skin.

In order to remove the skin-breast artifact in simulated data, the following procedure is usually used. A simulation of a tumor-free breast is performed and the signals are subtracted from the signals acquired from the corresponding tumorous model. This gives a tumor-only response which is then used to evaluate imaging algorithms.

2.5.3 Ultrawide-band breast cancer detection and imaging algorithms

The general problem of microwave breast cancer detection can be viewed as follows: based on the recorded microwave signals, identify if a tumor exists inside the breast or not. This ultimate goal can be approached in several ways.

One approach is to apply a machine-learning algorithm that can provide a direct answer if a tumor exists in the breast or not. These algorithms are based on extensive statistical model training (learning). Efficient algorithms, such as Support Vector Machines (SVM) and neural networks have been developed and can provide a high detection rate (see section 2.5.4). The machine-learning approach is relatively new in microwave breast cancer detection and has not been well advanced due to several problems: it requires a large amount of training data, which is not easy to obtain; the decision made by a classifier is based on unknown rationale; as practice shows, it is very hard to detect a tumor when parameters of the breast change (training on different datasets makes the classifier more general, which introduces errors).

Another approach involves imaging, which has traditionally been used in other modalities, such as mammography, ultrasound and MRI. This is a two-stage approach: first, an image of the breast is built and, second, it is analyzed to detect and localize tumors. The second stage can be done either manually (by a trained clinical professional) or by software. There are several challenges associated with the software-driven detection of tumors. First, generating a high-quality image that can be used to automatically detect tumors is a hard task. Second, to make the decision, the algorithm requires a threshold. Estimation of the threshold, similarly to the machine learning approach, requires large amount of training data. The advantage of the imaging approach is that it generates an image, which can be analyzed

by a human to verify the decision made by the algorithm. Further in this thesis imaging approach will be considered, if not mentioned otherwise.

Most of the UWB breast imaging algorithms have been adapted from radar signal processing. They all strive to resolve issues resulting from the following: *a*) the propagation of microwaves occurs in a multi-media environment that usually consists of a background (air or matching medium), skin and breast tissue; *b*) breast tissue is highly heterogeneous; *c*) in most cases, no far-field assumption can be made since antennas are located close to the breast.

The first algorithm applied to UWB breast imaging was the Delay-And-Sum (DAS) beamformer [1, 61, 94]. The DAS algorithm applies synthetic spatial focusing of the collected signals by time-shifting them to a particular point inside the breast interior, then adding them together and detecting the peak of the resulting waveform. The idea of this algorithm is that when a tumor is present at a particular point, pulses reflected from this scatterer are coherently summed up together, which results in a higher energy peak. When no tumor is present, the peaks that might come from other locations are not in phase, which spreads their energy along the resulting waveform and there is no strong pulse. The map of the resulting waveform peaks provides the image of scattering power in the breast interior, which potentially highlights the presence of tumors.

Resolution and detection performance of this algorithm has been analyzed in [125]. It is reported that, according to numerical studies, tumors of less than 1 cm in diameter can be successfully detected. An experimental feasibility study [126] has confirmed the detection of objects with size of 1.2 cm.

Several modifications to improve performance of DAS have been introduced. Delay-Multiply-And-Sum (DMAS) algorithm [127] applies cross-multiplication of all the signals before applying the DAS algorithm - this effectively suppresses clutter in the resulting image. Further, in chapter 6 of this thesis, the DMAS algorithm is analyzed and its optimized version is proposed.

Klemm et al. proposed an Improved Delay-and-Sum (IDAS) beamforming algorithm in [128], applied to their experimental system. The IDAS introduces an additional weighting quality factor, which helps highlighting those areas with significant reflectors. Another variation of DAS, Delay-and-Product beamforming algorithm, has been introduced in [129].

Instead of summing the time-shifted signals, this beamformer computes their product and calculates the amount of in-phase components in the resulting product vector. A similar approach combining the above ideas is published in [130].

Further improvement of the DAS algorithm is proposed in [131]. The described channel-ranked beamformer uses only those channels from the multistatic signal array, for which the signal propagation distance is lower than a certain pre-determined threshold. Due to the shorter propagation distance, the recorded signals are stronger in their amplitude, which improves their signal-to-noise ratio. The proposed beamformer demonstrates increased performance, compared to the traditional DAS [131].

Besides the described improvements, DAS-like algorithms are limited in performance due to: *a*) coarse time-shifting of the signals due to discretization in time; *b*) assumption of frequency-independent propagation speed in breast tissues; *c*) assumption that the propagation speed in breast tissues is perfectly known.

To overcome the drawbacks of the DAS algorithm, the Microwave Imaging via Space-Time (MIST) beamforming was introduced into the microwave imaging field by Bond et al. [75]. Later in this thesis we refer to the described MIST algorithm as Filter-And-Sum (FAS) beamformer. The proposed algorithm is also based on the time-alignment of signals to perform spatial focusing and uses additional filtering. The filter is designed to equalize path length dependent dispersion and attenuation, interpolate any fractional time delays remaining in the backscattered tumor responses after coarse time alignment, and band-pass filter the signal [75]. The filtered signals are then summed-up and time-windowed to calculate power corresponding to the test location. The MIST algorithm has proven to be relatively robust to variations of dielectric parameters of tissue. Rigorous analysis has been performed in [75, 118, 132] to evaluate the performance of the algorithm under the mismatch between average taken dielectric properties and the actual ones. A similar approach to compensate for the attenuation and dispersion is followed in [133], which demonstrates the robustness of MIST to breast heterogeneity and tumor size.

Further works extended the application of the described algorithms to multistatic systems. Due to the increased amount of information, multistatic algorithms further improve the detection performance [122, 134–136].

Another type of UWB breast imaging technique is the Generalized Likelihood Ratio Test

(GLRT). It was adopted by Davis et al in 2005 and is described in [76]. The algorithm is based on statistical hypothesis testing approach. Describing the no-tumor scenario as a null-hypothesis and assuming the alternative hypothesis when tumor exists, each of the test locations inside the breast domain is tested based on a computed test statistic. The test statistic is a value representing a degree of similarity between the received signal and some theoretical "signal template", which is derived by modeling a wave propagation inside the breast. In contrast to the beamforming approach, hypothesis testing does not make an assumption of a linear steering operation on a common signal. Instead, it proposes a way to apply a signal model of arbitrary complexity. For example, scattering effects can be included into the model, which may significantly increase matching the signal templates to the signals recorded by antennas. The image of the computed test statistic values for each spatial location provides the probability map of tumor presence at those locations. In order to provide an answer on whether a tumor exists in the breast or not, a thresholding technique should be applied. The value of the threshold is obtained with the procedure of false discovery rate control, proposed by Benjamini et al. in [137]. More recent papers on this technique are available [138, 139].

Studies of the detection approach in our group using numerical datasets from reduced-contrast phantoms demonstrate that the GLRT method is very promising as it gives high performance on medium-complexity scenarios and is the only successful algorithm on highly-heterogeneous and extremely dense breast phantoms [96].

Both works, [75] (MIST) and [76] (GLRT), report the capability of the algorithms to detect and localize small tumors (< 0.6 cm) in numerical breast phantoms when the contrast of dielectric permittivity between normal and malignant tissues decreases to 2:1.

A technique based on multiple windowing is proposed by Bond et al. in [140]. It employs multiple space-time beamformers (or windows) to obtain approximately statistically independent images of backscattered power which are then averaged. According to the published results, this approach improves the signal-to-clutter ratio and enables the detection of 2-mm-diameter lesions in very heterogeneous tissues.

Further steps in detection performance have been made with the introduction of robust algorithms. The robust methods have been developed to deal with the challenges associated with experimental trials. Since in the experimental setup there are significantly more unknown factors compared to the numerically simulated signals, robustness in signal

processing is essential.

A data-adaptive technique called Robust Weighted Capon Beamformer (RWCB) has been proposed in [141, 142]. Similar to previously described algorithms, the signals are spatially focused to the points within the breast. However, in order to deal with uncertainties in the attenuation due to the propagation in lossy tissues with unknown loss, additional factors are introduced (see chapter 3). These factors are adjusted based on the analysis of the recorded data, and their optimum values that maximize the signal-to-noise ratio are taken. In addition, authors in [142] propose the Amplitude and Phase Estimation (APES) algorithm, with the intention to compute beamformer weights based on the known signal waveform, provided by the RWCB algorithm. The volumetric image is then calculated similar to DAS and MIST algorithms as the power of the resulting summed signal. Investigations in [141, 142] demonstrate that these two data-adaptive techniques outperform their data-independent counterparts in terms of improved resolution and better interference suppression.

The increase in available computational power has enabled robust multistatic signal processing. Works by Xie et al. [143, 144] describe the application of adaptive techniques, such as Robust Capon Beamformer (RCB), which is a simplified version of RWCB without the data-adaptive window. The Multistatic Adaptive Microwave Imaging (MAMI) algorithm is presented in [143]. For each transmitting antenna, a multistatic setting provides a set of received waveforms at receiving antennas when every other antenna acts as a transmitter. The authors propose a two-stage algorithm which first applies an RCB procedure for each group of signals pertaining to one transmitting antenna separately. The second stage applies the RCB algorithm again to produce one combined waveform for a given synthetic focus location. Then, the power is calculated similar to the DAS and MIST algorithms. The paper [144] compares the proposed method with different combinations of other techniques: multistatic DAS, RCB, APES, MIST and monostatic DAS. It is demonstrated that MAMI clearly stands out from all other techniques but requires higher computational resources. Further development of this technique is described in [144], where authors propose another variation of the MAMI algorithm (MAMI-II) by changing the order of the two described stages. It is reported that these two algorithms provide better performance for different Signal-to-Interference-and-Noise Ratio (SINR). The authors in [144] combine these two

modifications of MAMI to produce a universal MAMI-C algorithm. Investigations of its performance show that the combined version outperforms the MAMI-I and MAMI-II algorithms for 4-mm and 6-mm tumor detection, for both low and high signal-to-noise values.

The forward-scattering radar system proposed by Munawar et al. in [145] employs a bistatic system to scan the area of the breast. The basic idea of the algorithm consists in the analysis of the Doppler frequency in the received signals.

Another type of robust beamformer is known as the time-reversal beamformer, which is described in [146] and further developed for complex breast models in [147]. This method is an adaptive waveform transmission scheme that utilizes the rich scattering medium to best match the target response. It is shown that this technique is more robust and provides higher resolution than conventional beamformers.

Another approach to MWI is synthetic aperture radar imaging (also known as holography), which is applied to microwave breast cancer imaging in works of Flores-Tapia et al. [148]. The algorithm employs a spatial fast Fourier transform, which makes imaging procedure much faster than the traditional approach and enables real-time breast scanning.

Wavelet analysis is applied in works by Lazaro et al. [97] to estimate the time of arrival of tumor response. The rationale of wavelet transform application is based on the idea that it provides a convenient tool to perform a multiple scale correlation analysis between the received signal and signal templates in shape of a Gaussian pulse, which can be represented as a wavelet.

2.5.4 Machine learning approach

Machine learning algorithms have been applied to breast cancer detection. A decision-making structure is being trained with multiple datasets, for which the tumor existence is already determined by other means ("supervised learning"). Then trained, these machines can then classify new cases as either tumorous or not. The main difference of these algorithms from the imaging algorithms is that they usually draw a conclusion without any intermediate step, such as formation of images or probability maps. This makes it hard to evaluate their decision in favor of one or another conclusion. In a publication by Kerhet et al. [149] an SVM-based approach is described. An SVM

classifier is being taught to distinguish tumor-bearing signals from the normal ones. Neural networks-based approach is represented in works by AlShehri et al. in [150] and Woten et al. [151]. They use similar forward-scattering setting and adapt neural networks for classification purposes. Kurrant et al. in their paper [152] propose Bayesian classifier approach to compress the data into a lower dimensional space.

There has been significant interest in classification algorithms recently [153–156]. High values of detection performance have been reported in [157–159]. In spite of the promising results, currently the application of machine learning techniques remains challenging. The main reason is that in order to train a classifier, large amount of training data is required. In order to get such data patients have to be first accurately diagnosed with clinical methods to get the training outputs, then UWB radar data collection has to be applied to the same patient to get the corresponding training inputs. Considering that for successful training the number of needed patients might be high, clinical trials of this size may be difficult for many research groups.

2.5.5 Algorithm performance comparison

Several publications that compare imaging techniques are available. For example, [143] compares six UWB imaging algorithms in a common setting. Studies described in [135, 136] evaluate data-independent algorithms using numerical breast models.

Although most of the algorithms build an image of statistical measure of tumor presence, which can be directly compared, it becomes a challenge to provide equal initial conditions, which greatly affect the performance of the algorithms and complicate the comparison. There are many factors, such as simplifying assumptions of the propagation model (accountability for dispersion, breast shape, level of heterogeneity and dielectric contrast); number of antennas and array configurations; the type of matching medium; pulse shape and frequency range. To estimate the relative efficiency of the algorithms, they should be applied to one equal setting. The author of this thesis was involved in a study that compares a set of algorithms on a series of numerical breast phantoms with variable degree of heterogeneity and dielectric contrast between tumorous and normal tissues [96]. This study is described further in this thesis in chapter 6.

2.5.6 Experimental studies

Currently no complete clinical UWB radar breast imaging device, ready for FDA-approval, has been developed. However, several prototypes have been constructed and their results reported in publications.

The first time-domain UWB breast cancer detection system has been described in [71]. The second generation of this system [2] has been assembled for clinical trials. The described TSAR system is composed of a patient table with a hole for a breast to be immersed into a special reservoir filled with canola oil. Multiple studies have been performed with this experimental system, including studies with patients [160].

A clinically-ready experimental system with a fixed multistatic hemispherical antenna array has been developed by Craddock et al. [161, 162].

The research group at McGill University has developed and advanced an experimental multistatic hemispherical microwave breast imaging system based on time-domain measurements [72, 163]. The system has been tested on volunteers and prepared for clinical trials at the time of the thesis submission.

2.6 Conclusion

Ultra-wideband microwave breast imaging is a novel area in breast cancer screening, which has a potential to complement existing clinical modalities for early breast cancer detection.

Currently, microwave breast cancer detection and screening faces several challenges, which are, in part, a subject of investigations reported in this thesis:

a) Efficient antenna design: the group at McGill University has been working on improving both RF and mechanical performance of the antennas. The main focus is to design a small, but yet efficient antenna that can be integrated into the whole system design;

b) Improvement of a radome design: a breast-holding radome has to be made of dielectrically compatible material, be able to hold the antenna array and minimize the number of air gaps and other surface discontinuities encountered by the emitted

microwave signal;

c) Removal of artifacts from signals: no algorithm has so far been developed to efficiently remove the skin reflection artifacts from the collected signals;

d) Efficient data sampling unit: multistatic data has to be collected fast enough to minimize artifacts associated with patient movement. On the other hand, it is essential to maximize the dynamic range and to keep the noise floor of the sampled signals as low as possible. These requirements set constraints to the design of a new sampling unit for the experimental system.

e) Robust imaging algorithms: in a realistic clinical environment, prone to high noise and multiple sources of measurement uncertainties, an adaptive approach is needed. The group at McGill University has been working towards improved imaging algorithms to apply to experimentally obtained data.

Chapter 3

Theoretical background: time-domain microwave breast imaging

This chapter provides the theoretical background of the microwave imaging algorithms. In the formulations throughout the document the following notation is used. Lower-case bold symbols denote one-dimensional column-vectors while upper-case bold symbols denote matrices. Superscripts T, H and -1 denote the transpose, the conjugate transpose and the inverse, respectively. Symbols $Re\{\cdot\}$ and $Im\{\cdot\}$ denote real and imaginary parts of a complex variable, respectively. Lower-case symbols represent time-domain signals and their upper-case counterparts denote the frequency-domain representation of the signals. Forward and inverse Fourier transform of signal x are denoted by $\mathcal{F}(x)$ and $\mathcal{F}^{-1}(x)$, respectively.

The rest of the chapter is organized as follows. First, the general problem of microwave breast imaging is formulated and a theoretical model of the signals is introduced. Further, the chapter describes theoretical EM propagation models and models for the dielectric properties of breast tissues. The core of this chapter represents the formulation of the MWI algorithms based on detection theory (section 3.5) and beamforming (section 3.6). In order to quantitatively assess the performance of the imaging algorithms, appropriate metrics are defined in section 3.7.

3.1 Problem statement and signal model

A typical data acquisition scenario for breast cancer detection is depicted in Fig. 3.1. A patient is lying in a prone position having one of the breasts immersed into the matching medium and surrounded by an array of antennas held in the radome. The breast is illuminated with microwave radiation; the response is received by the antennas and recorded by a sampler.

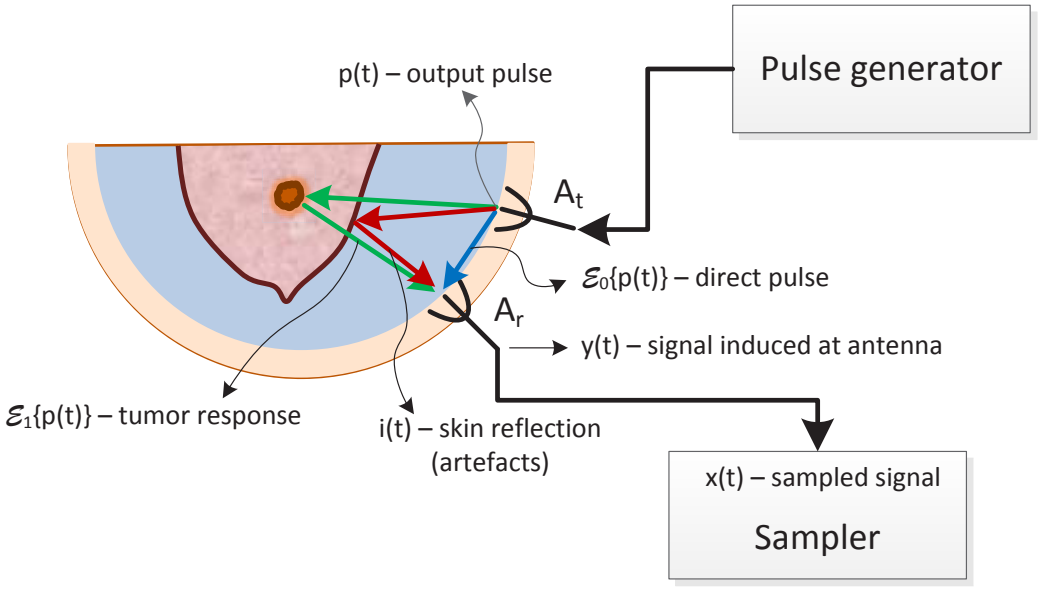

Fig. 3.1 A typical data acquisition scenario for beast cancer detection.

As mentioned in chapter 2, the goal of MWI is to build an image representing the internal structure of the breast, which potentially enables the detection and localization of tumors therein.

A short-duration pulse $p(t)$ generated by a pulse generator is transmitted by the antenna A_t. It is assumed that antennas transmit with a wide beam pattern. Thus, the transmitted pulse propagates from antenna A_t toward the breast, as well as directly toward other (receiving) antennas A_r (direct pulse). The direct pulse contributes to the

overall received signal and this contribution is denoted by $\mathcal{E}_0\{p(t)\}$. After the transmitted pulse has experienced scattering and propagation through the tissues, the received signal contains the following components: reflection from skin and other artifacts (including external electromagnetic interference), $i(t)$; reflections from tumors inside the breast, $\mathcal{E}_q\{p(t)\}, q = 1, \ldots, Q$; reflections from heterogeneous glandular structures inside the breast, clutter $c(t)$.

Thus, the total field at antenna A_r is modeled as:

$$E(t) = \sum_{q=0}^{Q} \mathcal{E}_q\{p(t)\} + i(t) + c(t) \tag{3.1}$$

The induced signal at the input of the sampler will be a function of the EM field at the input of antenna A_r, i.e.:

$$y(t) = \mathcal{H}_a\{E(t)\} \tag{3.2}$$

Here function $\mathcal{H}_a$ models the transformation associated with the characteristics of antenna A_r.

Signal $y(t)$ received by the antenna A_r is sampled with period T_s in $n = 1, \ldots, N$ samples. The moment when the receiver starts sampling is denoted by t_0 (which is the propagation delay in cables and other equipment in the path from the antenna A_r to the sampler input) and its error by random variable e_t (the triggering time error). The digitized version of the signal $x[n]$ will contain uncertainties associated with the data acquisition system (measurement noise), which are combined in a random variable $e_v[n]$:

$$x[n] = y(t_0 + e_t + nT_s) + e_v[n] \tag{3.3}$$

It is assumed in (3.3) that the triggering time error e_t is constant throughout one collected waveform of N samples, i.e. that, after the first sample, the next samples will be collected with constant time interval T_s.

In order to highlight the tumor within a formed three-dimensional image of the breast, a sequential method of building the image is applied. In particular, a scan geometry is defined

as a three-dimensional block with dimensions W_x, W_y and W_z, and spatial resolution h_x, h_y, h_z. This results in images of size $[W_x/h_x, W_y/h_y, W_z/h_z]$ and total number of voxels $L = W_x/h_x \cdot W_y/h_y \cdot W_z/h_z$. Each of the voxel values $I_\ell,\ \ell = 1, \ldots, L$ is associated with spatial location $\mathbf{r}_\ell = \{x_\ell, y_\ell, z_\ell\}$. The voxel values are computed independently from each other. Their values depend on the algorithm applied. Further in this chapter imaging algorithms that follow the sequential imaging method are described.

3.2 Signal pre-processing

Before any imaging algorithm can be applied, the collected signals have to be pre-processed to compensate for unwanted artifacts $i(t)$, direct pulses $\mathcal{E}_0\{p(t)\}$ as well as measurement-related noise e_v and e_t.

Compensation for measurement noise is specific to a particular data acquisition system. Section 5.2 of this thesis presents the analysis of the noise related to the experimental system of the research group at McGill University. A method to minimize the phase noise of the microwave sampler is described in section 5.3.

In order to remove the direct pulse, previously recorded baseline signals (i.e. the signals recorded without the tumor inserted in the phantom) are subtracted from the signals that are collected from patients (as in [94]). Skin-breast artifact removal is an essential part of the breast cancer detection time-domain UWB radar signal pre-processing. The artifact removal step is applied to both numerically-simulated and experimentally-recorded signals. Several methods of the skin-breast artifact removal have been described in the literature, applied to the following imaging scenarios:

1) Breast shape is close to hemispherical. This makes all the reflection signals look the same and thus the reflection pulse can be estimated as the average between all the collected time-domain signals. This averaged signal is then subtracted from all the collected signals, which leaves signals only with tumor response and clutter. The details of this method can be found in [94].

2) Breast shape has regular convex shape close to half-ellipsoid. In this case, the reflections might have slightly different shape and location in the waveform. However, it is assumed that the reflection from the skin can be well localized in time and easily separated from

the region of interest (tumor response). For this scenario, the algorithm based on Wiener filtering [75, 164] provides the best results.

3) Breast has an irregular shape with concave regions. This introduces a significant degree of distortion of the pulse reflected from the skin. In this case, the reflection cannot be separated from the rest of the remaining signal, including the tumor response. Several attempts have been made to address this problem [123, 124, 165], but with little success.

The signals acquired using the experimental system in our research group (see chapter 5) are bandpass-filtered to remove all the frequency contents outside of the frequency range of interest of 2 - 4 GHz.

The digitized signals with the mitigated noise and artifact components have the following model:

$$x[n] = \sum_{q=1}^{Q} \mathcal{E}_q\{p[n]\} + c[n] \qquad , \tag{3.4}$$

where $p[n]$ and $c[n]$ are digitized versions of $p(t)$ and $c(t)$, respectively.

3.3 Signal propagation models

Most of the microwave imaging algorithms can be referred to as "model-based" algorithms since they rely on *apriori* knowledge about the propagation of EM waves in biological materials. This section describes essential properties of human breast tissues.

3.3.1 Modeling dielectric material properties

Propagation of EM waves can be described based on dielectric properties of the propagation media. These are dielectric permittivity and conductivity. The following relationships [166] are used in the models described further:

$$\epsilon = \epsilon' - j\epsilon'' = \epsilon_0 \underbrace{(\epsilon'_r - j\epsilon''_r)}_{\epsilon_r} = \epsilon_0(\epsilon'_r - j\frac{\sigma_e}{\omega\epsilon_0}) = \epsilon_0(\epsilon'_r + \frac{\sigma_e}{j\omega\epsilon_0}) \qquad , \tag{3.5}$$

where the symbols represent the following quantities:

ϵ - complex (absolute) permittivity [F/m];
ϵ' - real-valued permittivity, also known as just "permittivity" (quantifies energy stored within the medium) [F/m];
ϵ'' - imaginary part of complex permittivity (quantifies dissipation (loss) of energy within the medium) [F/m];
ϵ_0 - permittivity of free space, $\epsilon_0 \approx 8.85 \cdot 10^{-12}$ [F/m];
ϵ_r - relative permittivity [unitless];
ϵ'_r - real-valued relative permittivity [unitless]; note: in many literature sources real-valued permittivity is denoted with just ϵ_r omitting the prime sign for simplicity;
ϵ''_r - imaginary part of relative permittivity, also known as "loss factor";
σ_e - effective conductivity [S/m];
$\omega = 2\pi f$ - angular frequency [rad/s];
f - frequency of the propagating wave [Hz].

In order to analytically model dispersive materials in the microwave range, measured dielectric properties can be represented by mathematical models. Several models, such as Cole-Cole and Debye [167], are based on a number of parameters. The research described in this thesis makes use of the Debye model, defined with four coefficients:

$$\epsilon_r(\omega) = \epsilon_\infty + \frac{\Delta\epsilon}{(1 + j\omega\tau)} + \frac{\sigma_s}{(j\omega\epsilon_0)} \quad , \tag{3.6}$$

where:
ϵ_∞ - relative permittivity at infinite frequency [unitless];
$\Delta\epsilon = \epsilon_s - \epsilon_\infty$ - difference between static relative permittivity ϵ_s (at $f = 0$, zero frequency) and relative permittivity at infinite frequency ϵ_∞ [unitless];
σ_s - static conductivity [S/m];
τ - relaxation constant [s].

The model is fit to the data recorded with a probe and a vector network analyzer.

The graphs of real-valued relative permittivity ϵ'_r can be obtained by plotting $Re\{\epsilon(\omega)\}$. Effective conductivity is given by:

$$\sigma_e(\omega) = \omega\epsilon_0\epsilon''_r(\omega) = \omega\epsilon_0 Im\{\epsilon_r(\omega)\} \quad . \tag{3.7}$$

3.3.2 Modeling electromagnetic propagation effects

Delay and attenuation

EM waves propagate in a medium with a velocity of [166]:

$$v_b = \frac{1}{\sqrt{\mu_b \epsilon_b}} = \frac{c}{\sqrt{\mu_{r,b} \epsilon_{r,b}}} \quad , \tag{3.8}$$

where $c \approx 2.998 \cdot 10^8$ [m/s] - speed of light in vacuum, μ_b [H/m] and $\mu_{r,b}$ [unitless] - electromagnetic permeability and relative permeability of the background medium, respectively ($\mu_{r,b} \approx 1$ for non-magnetic materials, such as human tissues); ϵ_b [F/m] and $\epsilon_{r,b}$ [unitless] are permittivity and relative permittivity of the background medium, respectively.

The following equation describes a plane-wave propagating along the $+z$ direction [166]:

$$H_{da}(z) = e^{-\gamma_b z} = e^{-jk_b z} \quad , \tag{3.9}$$

where:
$H_{da}(z)$ - propagation factor describing delay and attenuation due to lossy medium, as the wave propagates along $+z$ axis;
$\gamma_b = jk_b = \alpha_b + j\beta_b$ - propagation constant of the background medium [m^{-1}];
α_b - attenuation constant of the background medium [Np/m];
β_b - phase constant of the background medium [rad/m];
z - propagation distance along $+z$ axis [m];
$k_b = \omega\sqrt{\mu_b \epsilon_b}$ - complex wave number related to the background medium [rad/m].

Expression (3.9) is a frequency-domain model that includes delay and attenuation. If the value of propagating pulse is $P(\omega) = \mathcal{F}(p(t))$ at point $z = 0$ (origin), then the value of the electric field at a distance z from the origin will be:

$$P_z(\omega) = \mathcal{E}\{P(\omega)\} = P(\omega)H_{da}(z) = P(\omega)e^{-jk_b z} \quad , \tag{3.10}$$

If, in addition to the delay and attenuation, (3.10) takes into account frequency-dependent

propagation effects, i.e. dispersiveness of the propagation medium, then the wave number k is also dependent on ω.

In the time domain, propagation delay is represented by a time-shift of the signal and attenuation can be modeled with an additional factor. In particular, a signal pulse $p(t)$ that propagates to point z from origin in the medium defined above can be represented as follows:

$$s(t) = e^{-\alpha_b z} p\left(t - \frac{z}{v_b}\right) = H_a(z) p\left(t - \frac{z}{v_b}\right) \quad , \tag{3.11}$$

where $H_a(z) = e^{-\alpha_b z}$ is the lossy medium attenuation factor, defined in the time-domain model separately from the delay factor. Equation (3.11) is applied only to monochromatic or narrow-band signals or in cases when dispersiveness of the medium can be neglected (i.e. when dielectric properties are approximately constant with frequency).

Spreading

Energy density of an EM wave fades as the wave propagates through free space. The expansion of the wavefront is referred as the "spatial spreading" and in order to model this effect, another factor H_{sp} is introduced. In this work three types of EM wavefronts are considered, which determine how EM waves lose their energy density with the distance.

Spherical wave. In this case, the source is represented by an omnidirectionally radiating sphere or point. The surface area of the wavefront in this scenario is proportional to the square of the propagation distance z [168]. Assuming that the power is uniformly distributed per unit of solid angle, it is inversely proportional to the square of the propagation distance z. Therefore, for a spherical wave, the field amplitude is inversely proportional to the distance z:

$$H_{sp}(z) = \frac{1}{z} \quad . \tag{3.12}$$

This model is employed in scenarios when antennas have compact size (which is the realistic case in the the discussed imaging problem) and can be modeled as point sources.

The antenna performance, such as the radiation pattern and gain can be additionally compensated by characterizing antenna properties from measurements and introducing them into the EM model.

Cylindrical wave. This model is used to describe the wave propagation in two-dimensional space, i.e. when all objects are represented by infinitely long structures elongated along the axis perpendicular to the two-dimensional plane of our model. In this case, the spatial spreading factor can be described as follows:

$$H_{sp}(z) = \frac{1}{\sqrt{z}}. \tag{3.13}$$

This expression is used in numerical two-dimensional scenarios when the analysis of the full three-dimensional space is not feasible due to the computational complexity.

Plane wave. This ideal model is employed when the size of the antenna is relatively big compared to the irradiated geometry. In this case, the emitted wave has a very big wavefront radius and thus can be approximated by a plane. The spreading effect for the plane wave does not apply, which is reflected in:

$$H_{sp}(z) = 1 \qquad . \tag{3.14}$$

EM scattering

When an EM wave encounters a tumor inside the breast, part of its energy is scattered back, another part is transmitted further and the rest is absorbed by the tumor.

In this work, two methods of scatter modeling are considered. A simplified model is described by a scalar factor that shows the amount of energy of the pulse that is scattered/transmitted toward the receiving antenna from a given scatterer:

$$H_{sc}(z) = \sigma. \tag{3.15}$$

The coefficient σ depends on the shape of the tumor, its size and its dielectric properties. It is also known in the literature as the radar cross section.

More advanced scattering model involves analytic solution to the problem of a plane wave scattered by a dielectric sphere. This section summarizes the derivation of a closed form solution for the problem of a plane wave impinging on a dielectric sphere. More details can be found in [168–170].

The derivation begins with the expression for the scattered electromagnetic field for the described problem, given in [168]:

$$E_r^s = -jE_0\cos\phi\sum_{n=1}^{\infty} b_n\left[\hat{H}_n^{(2)\prime\prime}(\beta r)+\hat{H}_n^{(2)}(k_b r)\right]P_n^1(\cos\theta) \tag{3.16a}$$

$$E_\theta^s = \frac{E_0}{k_b r}\cos\phi\sum_{n=1}^{\infty}\left[jb_n\hat{H}_n^{(2)\prime}(k_b r)\sin\theta P_n'^1(\cos\theta)-c_n\hat{H}_n^{(2)}(k_b r)\frac{P_n^1(\cos\theta)}{\sin\theta}\right] \tag{3.16b}$$

$$E_\phi^s = \frac{E_0}{k_b r}\sin\phi\sum_{n=1}^{\infty}\left[jb_n\hat{H}_n^{(2)\prime}(k_b r)\frac{P_n^1(\cos\theta)}{\sin\theta}-c_n\hat{H}_n^{(2)}(k_b r)\sin\theta P_n'^1(\cos\theta)\right] \quad . \tag{3.16c}$$

Here $E_r^s, E_\theta^s, E_\phi^s$ denote the components of the scattered electric field in spherical coordinates r, θ, ϕ; k_b is the wave number of the background medium (relative permeability $\mu_b = 1$); $\hat{H}_n^{(2)}$ is spherical Hankel function of the second kind; $P_n^1(\cos\theta)$ are Legendre functions; $(\cdot)'$ and $(\cdot)''$ denote respectively the first and the second derivatives with respect to the argument of the function. The expressions for the coefficients b_n and c_n depend on the properties of the sphere. For a dielectric sphere with radius a and wave number k_d, the coefficients are given by:

$$b_n = \frac{-k_d\hat{J}_n'(k_b a)\hat{J}_n(k_d a)+k_b\hat{J}_n(k_b a)\hat{J}_n'(k_d a)}{k_d\hat{H}_n^{(2)\prime}(k_b a)\hat{J}_n(k_d a)-k_b\hat{H}_n^{(2)}(k_b a)\hat{J}_n'(k_d a)}a_n \quad , \tag{3.17a}$$

$$c_n = \frac{-k_d\hat{J}_n(k_b a)\hat{J}_n'(k_d a)+k_b\hat{J}_n'(k_b a)\hat{J}_n(k_d a)}{k_d\hat{H}_n^{(2)}(k_b a)\hat{J}_n'(k_d a)-k_b\hat{H}_n^{(2)\prime}(k_b a)\hat{J}_n(k_d a)}a_n \quad , \tag{3.17b}$$

$$a_n = \frac{j^{-n}(2n+1)}{n(n+1)}, \tag{3.17c}$$

where $\hat{J}_n$ denotes nth order spherical Bessel function [168].

In the monostatic scenario, where the receiver and transmitter are located at the same

spatial point, only co-polar component of the scattered E_x is of interest, which is found as:

$$E_x^s = E_\theta^s \cos\theta \cos\phi \,|_{\substack{\theta=\pi \\ \phi=\pi}} = E_\theta^s \,|_{\substack{\theta=\pi \\ \phi=\pi}} \quad . \tag{3.18}$$

Further simplification comes from using the following relationships [169, p.295]:

$$\frac{P_n^1(\cos\theta)}{\sin\theta}\,|_{\substack{\theta=\pi \\ \phi=\pi}} = (-1)^n \frac{n(n+1)}{2} \tag{3.19a}$$

$$\sin\theta P_n^{1\prime}(\cos\theta)\,|_{\substack{\theta=\pi \\ \phi=\pi}} = (-1)^n \frac{n(n+1)}{2} \quad . \tag{3.19b}$$

Thus, for the monostatic case:

$$\begin{aligned} E_x^s\,|_{\substack{\theta=\pi \\ \phi=\pi}} &= \frac{E_0}{k_b r}(-1)\sum_{n=1}^{\infty}\left[jb_n\hat{H}_n^{(2)\prime}(k_b r)(-1)^n\frac{n(n+1)}{2} - c_n\hat{H}_n^{(2)}(k_b r)(-1)^n\frac{n(n+1)}{2}\right] \\ &= \frac{E_0}{k_b r}(-1)\sum_{n=1}^{\infty}(-1)^n\frac{n(n+1)}{2}\left[jb_n\hat{H}_n^{(2)\prime}(k_b r) - c_n\hat{H}_n^{(2)}(k_b r)\right] \quad . \end{aligned} \tag{3.20}$$

Further, (3.20) can be simplified by introducing a new variable: $\tilde{b}_n = -b_n/a_n; \tilde{c}_n = -c_n/a_n$, noticing that $j^{-n} = (-1)^n j^n$ and combining all scaling factors before the sum as $\tilde{E}_0$. Thus, the final expression for the monostatic scenario becomes:

$$E_m^s(r) = \tilde{E}_0\sum_{n=1}^{\infty} j^{n-1}(2n+1)\left[\tilde{b}_n\hat{H}_n^{(2)\prime}(k_b r) + j\tilde{c}_n\hat{H}_n^{(2)}(k_b r)\right] \quad . \tag{3.21}$$

Thus, the overall scattering model based on the dielectric sphere is represented as:

$$H_s(z) = E_m^s(z) \quad . \tag{3.22}$$

In case when a two-dimensional scenario is considered (i.e., when the problem of a plane wave hitting an infinitely-long cylinder is considered), expression (3.21) will be simplified

as follows[169]:

$$E^s_{m2} = \tilde{E}_0 \sum_{n=-\infty}^{+\infty} (-j)^n a_n H^{(2)}_n(k_b r) \qquad , \tag{3.23}$$

where $H^{(2)}_n$ denotes the n^{th}-order cylindrical Hankel function of the second kind and the coefficient a_n is given by:

$$a_n = \frac{\frac{\epsilon_d}{k_d} J_n(k_b a) J_n^{'}(k_d a) - \frac{\epsilon_b}{k_b} J_n(k_d a) J_n^{'}(k_b a)}{-\frac{\epsilon_d}{k_d} H^{(2)}_n(k_b a) J_n^{'}(k_d a) + \frac{\epsilon_b}{k_b} J_n(k_d a) H^{(2)'}_n(k_b a)} \qquad , \tag{3.24}$$

where ϵ_b and ϵ_d are the relative permittivities of the background medium and the dielectric cylinder, respectively; J_n denotes the n^{th}-order Bessel function, and $(\cdot)^{'}$ denotes the derivative with respect to the argument of the function.

Multi-media propagation

In the process of microwave imaging, EM waves emitted from antennas propagate toward the breast through several media, which can include: background (medium where antennas reside), matching medium (e.g. gel-like substance where the breast is placed), skin and breast tissue. The following simplified line-of-sight propagation model is used further in the MWI algorithms. The resulting effect of several media that the EM wave travels through is represented as the product of the propagation models of each of the media:

$$H_{mm} = \prod_{v=1}^{V} H_v(r_v) \qquad , \tag{3.25}$$

where v denotes the medium number; H_v represents the propagating model related to a medium v and r_v denotes the propagation distance in a given medium v.

It should be mentioned that the model in (3.25) holds only for a propagating plane wave. For the microwave breast imaging problem this is a very crude approximation, since the size of the antennas is not negligible compared to the distance that the wave is traveling (i.e., far field assumption does not hold) and antennas are modeled as point sources. However, as shown further in this thesis, the microwave images, produced based on this simplifying

assumption, can offer acceptable image quality to detect breast tumors at early stage.

3.3.3 Parameter estimation

Wave propagation models presented above have several parameters, such as background dielectric wave number k_b, scattering factor σ, tumor tissue wave number k_d and tumor radius a. Multi-media propagation requires the breakdown of the traveled distance into several components, which can be learned from the geometry of the breast. These parameters are usually unknown for each new patient and should be estimated beforehand by either taking some *apriori* known average value or learned by analyzing the recorded signals from a new patient. The methodology to estimate these parameters has been addressed in the literature and can be found in [113, 117, 121, 171–174].

3.4 Signal array model

As a general case, a multistatic imaging scenario is considered further in this thesis. Each of the $m = 1, \ldots, M$ antennas acts as a receiver and transmitter. This results in the array of $M \cdot M$ recorded signals for full multistatic scenario and an array of $M(M-1)$ for bistatic-only scenario (i.e., without monostatic signals when the same antenna cannot act as a transmitter and receiver at the same time).

Further in the derivations index m will be used to denote a channel number, which is represented by a combination of active transmitter/receiver pair of antennas. For most imaging algorithms, it is convenient to represent the signal model in a matrix form. In further formulations, the following three different representations will be used.

3.4.1 Time-domain sample-related representation

For a detection-theoretic approach it is convenient to represent the array of collected signals grouping samples in vectors as follows:

$$\mathbf{x}_m = \sum_{\ell=1}^{L} \alpha_\ell \mathbf{s}_{\ell,m} + \mathbf{c}_m \quad , \tag{3.26}$$

where $\mathbf{x}_m \in \mathbb{R}^{N\times 1}$ is a vector of N samples recorded at antenna m; $\mathbf{s}_{\ell,m} = \mathcal{E}_{\ell,m}\{p[n]\}$ - vector of the same size that represents modeled response from a potential tumor at location ℓ ($\mathbf{s}_{\ell,m}$ are further referred to as "signal templates"); $\mathbf{c}_m$ represents clutter and all other types of noise of the received waveforms. Parameter α_ℓ signifies the presence of a tumor response in the recorded signal ($\alpha_\ell = 0$ if no tumor is present at location ℓ and $\alpha_\ell \neq 0$ otherwise).

3.4.2 Time-domain channel-related representation

Another representation of the signal model is more appropriate for time-domain beamforming algorithms. This representation groups channels together allowing to work with samples separately.

Each of the M received time-domain signals $\mathbf{x}[n], n = 1, \ldots, N$ can be represented as follows:

$$\mathbf{x}[n] = \sum_{\ell=1}^{L} \alpha_\ell \mathbf{s}_\ell[n] + \mathbf{c}[n] \qquad , \tag{3.27}$$

where $\mathbf{x}[n] \in \mathbb{R}^{M\times 1}$ is a vector representing recorded signals at the M antenna elements at time instances nT_s with T_s denoting the sampling period; $\mathbf{s}_\ell[n]$ is a vector of the same size that represents the tumor response (deterministic signal); and $\mathbf{c}[n] \in \mathbb{R}^{M\times 1}$ is the signal component that represents the combination of the interference (clutter) and the rest of the noise. Parameter α_ℓ signifies the presence of a tumor response in the recorded signal coming from a possible location ℓ. It should be noted that the difference in representation between (3.26) and (3.27) in the matrix form would consist only in the transposition of the matrix forming the complete signal array.

3.4.3 Frequency-domain representation

The following frequency-domain representation of the signal model will be used for the MWI algorithms that are formulated entirely in frequency domain.

The frequency domain model of the recorded signal $Y_m(\omega)$ at channel m, related to the

bi-static antenna pair A_t (transmitter) and A_r (receiver) can be described as follows:

$$Y_m(\omega) = \sum_{\ell=1}^{L} A_{\ell,m}(\omega)\alpha_\ell S(\omega) + N_m(\omega) \qquad , \tag{3.28}$$

where $A_{\ell,m}(\omega)$ represents the element of the focusing vector related to channel m and frequency ω. $A_{\ell,m}(\omega)$ can be also viewed as the frequency response of the channel m, which includes propagation-related effects of the path from antenna A_t to location ℓ and from location ℓ to antenna A_r. In the equation above α_ℓ denotes the tumor presence at location ℓ, being equal to "one" in case a tumor is present at location ℓ and equal to "zero" otherwise. Noise introduced in a channel is denoted by $N_m(\omega)$, and $S(\omega)$ represents a frequency component related to frequency ω of the source signal. It should be noted here that only responses from tumor locations are taken in expression (3.28). This means that when the value of the image voxel related to location ℓ is computed, it is assumed that no reflections are coming from other locations than location ℓ. In reality, this is not true and the responses from other tissues within the breast are unavoidable. However, these reflections are expected to be much weaker, which is in the agreement with the physical properties of the tissues in microwave range. These reflections are usually referred to as clutter and in (3.28) they are incorporated in $N_m(\omega)$.

The focusing vector $\mathbf{A}_{\ell,m}$ can be modeled according to the assumed EM propagation model described in section 3.3. For example, to model the EM propagation in the scenario with the experimental acquisition system, the delay and attenuation, spreading and simple scattering model is considered, described by the following expression:

$$A_{\ell,m}(\omega) = H_{da,m,\ell}(\omega)H_{sp,m,\ell}(\omega)H_{sc,m,\ell}(\omega) \qquad . \tag{3.29}$$

The first term $H_{da,m,\ell}$ describes the attenuation due to lossy medium (real part) and the phase delay due to finite propagation speed in the medium (imaginary part). The second term is related to the attenuation due to the wave spherical spreading. Finally, the third term $H_{sc,m,\ell}$ describes the scattering effect from the tumor.

3.5 Detection-theoretic algorithm based on hypothesis testing

By design, breast cancer detection algorithms may address the complete task of detecting breast cancer, without the requirement of image analysis by an expert. However, the task of automatic detection task can be significantly more complicated than imaging, which poses additional challenges to signal processing algorithm design. Since detection algorithms usually provide an image map of the probabilities of tumor presence, they can be compared to imaging algorithms by comparing the quality of the output images in terms of the defined metrics (section 3.7).

One approach to the microwave detection of breast cancer is to test the presence of tumor at each location inside the breast. This approach is a good trade-off: on the one hand, it provides means for automatic detection of tumor presence, and, on the other hand, it still generates an image that can be evaluated by a human.

As mentioned previously, the research described in this thesis follows a sequential approach to build an image. The detection-theoretic approach applied to microwave breast cancer detection considers testing multiple hypotheses of a tumor presence at a finite set of locations $\ell = 1, \ldots, L$ inside the breast. As the result, this will produce an image that will represent the probability of tumor presence at these locations.

In the derivations of the detection theoretic algorithm, signal model (3.26) is employed, with make the following rearrangements. It is more convenient to stack vectors $\mathbf{x}_m$ to produce long column-vector $\mathbf{x} = [\mathbf{x}_1^T \ldots \mathbf{x}_M^T]^T$ of length $M \cdot N$. Similarly, concatenating vectors $\mathbf{s}_m, \mathbf{c}_m$, the resulting signal model is represented as follows:

$$\mathbf{x} = \sum_{\ell=1}^{L} \alpha_\ell \mathbf{s}_\ell + \mathbf{c} \qquad . \tag{3.30}$$

It can be seen that $\mathbf{x}$ in (3.30) consists of multiple possible reflections from potential tumors with $\alpha_\ell \neq 0$. In the detection approach only one hypothesis will be tested at a time, in particular the hypothesis that a tumor is present at the scan location ℓ. Thus, for a given test location ℓ only one term of the summation in (3.30) is considered. Thus, a model for

a given test location ℓ can presented as follows:

$$\mathbf{x} = \alpha_\ell \mathbf{s}_\ell + \mathbf{c} \quad , \tag{3.31}$$

where signal amplitude α_ℓ is treated as a deterministic unknown parameter equal to zero in case there is no tumor at location ℓ. Signal templates $\mathbf{s}_\ell$ are considered as deterministic and dependent on the set of parameters related to the EM propagation model applied for the test location ℓ, which are not always known exactly. Noise component related to clutter $\mathbf{c}$ is modeled as Gaussian with zero mean and covariance $\sigma_{\mathbf{x}}^2 \mathbf{R}_{\mathbf{x}}$, where matrix $\mathbf{R}_{\mathbf{x}}$ captures the structural properties of the covariance, and scalar $\sigma_{\mathbf{x}}^2$ specifies the noise power. The noise components are assumed to be independent between the channels. The noise covariance matrix $\mathbf{R}_{\mathbf{x}}$ can be estimated using training data sets containing responses from a number of cases free from signal component (i.e. with $\alpha_\ell = 0, \forall \ell = 1, \ldots, L$).

A binary hypothesis testing at each test location ℓ is formulated as follows:

$$\mathcal{H}_0 : \ \alpha_\ell = 0 \text{ vs. } \mathcal{H}_1 : \alpha_\ell \neq 0 \quad . \tag{3.32}$$

The signal model described by (3.26) and the assumptions listed above result in the detection problem of a known signal (up to a scaling factor) with the noise of unknown parameters. To address this challenge, a theoretical framework has been previously developed and is known as the Generalized Likelihood Ratio Test (GLRT) [175, 176].

Prior to the application of the GLRT, the input signals $\mathbf{x}$ are whitened using the estimated clutter covariance matrix:

$$\widetilde{\mathbf{x}} = \hat{\mathbf{R}}_{\mathbf{x}}^{-1/2} \mathbf{x} \quad . \tag{3.33}$$

In order to compensate for the distortion introduced by whitening, the signal templates are exposed to the same whitening procedure, which produces vector $\widetilde{\mathbf{s}}$. The tilde sign ("$\sim$") above $\mathbf{x}$ and $\mathbf{s}$ is further omitted for simplicity.

The GLRT performs the comparison of the generalized likelihood ratio $L_G(\mathbf{x})$ against some threshold η:

$$L_G(\mathbf{x}) \underset{\mathcal{H}_0}{\overset{\mathcal{H}_1}{\gtrless}} \eta \quad . \tag{3.34}$$

The expression for $L_G(\mathbf{x})$ and further derivations of the GLRT are given in [175, Ch. 9].

The resulting hypothesis testing rule can be represented as follows:

$$T_\ell(\mathbf{x}) = (NM-1)\,\frac{\mathbf{x}^H\mathbf{P}_\ell\mathbf{x}}{\mathbf{x}^H\mathbf{P}_\ell^\perp\mathbf{x}} \underset{\mathcal{H}_0}{\overset{\mathcal{H}_1}{\gtrless}} \gamma \qquad , \tag{3.35}$$

where $\mathbf{P} = \mathbf{s}\left(\mathbf{s}^H\mathbf{s}\right)^{-1}\mathbf{s}^H$ and $\mathbf{P}^\perp = \mathbf{I}-\mathbf{P}$ are projection matrices that project a vector onto the signal and noise subspaces, respectively.

In order to perform the automated test of the tumor presence inside the whole breast domain, the threshold γ can be selected by fixing the false-alarm rate to some value P_{FA} and based on the distribution of the test statistic under the null-hypothesis:

$$\gamma = \mathrm{CDF}^{-1}\left(1-P_{FA}\right) \qquad , \tag{3.36}$$

where CDF denotes the cumulative distribution function of the test statistic. Another approach is to use the false discovery rate control procedure as was proposed by Benjamini et al. in [137].

In addition to the automated detection test, for which threshold γ is required, images of $T_\ell(\mathbf{x})$ will be used to compare the algorithm with other imaging algorithms, as described at the beginning of this section. In this case, I_ℓ will be used in place of $T_\ell(\mathbf{x})$.

3.6 Beamforming image-formation algorithms

Beamforming imaging algorithms have been widely used in the areas of aerial radar, underwater sonar, ground-penetrating radar, and telecommunications. The basic idea of the beamforming is synthetic focusing of the incoming EM waves, which helps localizing their source. Applied to microwave breast imaging, this approach helps avoid solving the computationally-demanding inverse-scattering problem, which is the basis of microwave tomography.

The relationship of the beamforming approach to the hypothesis-testing described earlier in section 3.5 can be viewed as follows. The hypothesis-testing approach compares the received signals $\mathbf{x}$ with their corresponding theoretical signal templates $\mathbf{s}$ modeled for every test location ℓ with the assumption that a tumor exists at the given test location. The degree

of the similarity (the test statistic T_ℓ) represents the probability of the tumor presence at location ℓ. In contrast, in the beamforming approach, while scanning each test location, the recorded signals are being modified to compensate for the effects of propagation from a given transmitting antenna A_t toward a test location ℓ and from the test location ℓ to a receiving antenna A_r, thereby assuming that a reflector (potential tumor) exists at location ℓ. This compensation is further referred to as spatial focusing[1]. After compensating for the propagation effects, the following properties should be observed:

1. When a tumor is present at test location ℓ:
   - Similarity between the focused signals;
   - High degree of matching between the focused signals and the emitted signal;
2. When tumor is not present at test location ℓ the two properties mentioned in item 1 do not hold.

All beamforming algorithms are based on these properties. The next step after the spatial focusing is the computation the beamformer output, which is carried out by coherent summation of the focused signals. When a tumor is present and the focused signals sum-up coherently, the resulting power ("beamformer output power") will be high compared to the beamformer output power when no tumor is present at the synthetic focus location ℓ.

Notes on terminology

In the further derivations of the beamforming algorithms, a hemispherical antenna array is considered. In contrast to the conventional radar-theory problem definition with a linear array of antennas and an incident plane wave, the interest is not in the direction of arrival of the wave, but in the energy coming from a particular spatial point. Thus, the operation of the presented beamformer will be "focusing" rather than "steering". Therefore, for the discussed problem, the term "focusing vector" is used instead of "steering vector". Next, the continuous beamformer output is not important, i.e. the assumption is made that the system under analysis is static. Physically, this means that

[1]Spatial focusing, depending on the applied model, can be carried out by simple time-alignment of the signals and/or multiplying by a compensation factor

the patient is lying motioneless and the breast is not moving with respect to the antennas and the radome. These assumptions explain the choice of the signal models used in the derivations of the beamforming algorithms. The time-domain beamformers described further, use signal model given by (3.27). The frequency-domain algorithms employ signal model given in (3.28). The beamforming approach computes scattered signal power and does not consider scattering effects of the tumor or it assumes that the scattering effect is the same in the signals relative to all of the antenna elements.

3.6.1 Conventional spatial focusing: delay-and-sum beamforming

The Delay-And-Sum (DAS) beamforming applied to microwave breast imaging is also known as the confocal microwave imaging algorithm. It is the first time-domain algorithm applied to microwave breast imaging [94, 177].

The DAS beamforming is a time-domain algorithm. It is based on the assumption that the breast material is non-dispersive. To represent this algorithm, signal model in (3.27) is employed. Depending on the considered scenario, EM wave-propagation effects will be modeled by using one of the propagation models presented in section 3.3.2.

One iteration of the DAS algorithm to compute the value of a voxel, corresponding to test location ℓ, is represented in Fig. 3.2.

First, all recorded signals $\mathbf{x}$ are synthetically focused to a focal point ℓ by applying time-alignment and compensation for attenuation:

$$\widetilde{x}_{m,\ell}[n] = H^{-1}_{a,m,\ell} H^{-1}_{sp,m,\ell} x[n + \tau_{m,\ell}] \quad , \tag{3.37}$$

where $H_{a,m,\ell}$ is the lossy medium attenuation factor computed as defined in (3.11) for test location ℓ and channel m (propagation distance z is taken as the sum of the distances from transmitting antenna A_t to location ℓ and from location ℓ to receiving antenna A_r); $H_{sp,m,\ell}$ is the spatial spreading factor as defined in (3.12), (3.13) or (3.14) depending on the considered EM model; and $\tau_{m,\ell}$ is the propagation delay defined as follows:

$$\tau_{m,\ell} = \frac{z_{m,\ell}}{v_{ts}} \quad , \tag{3.38}$$

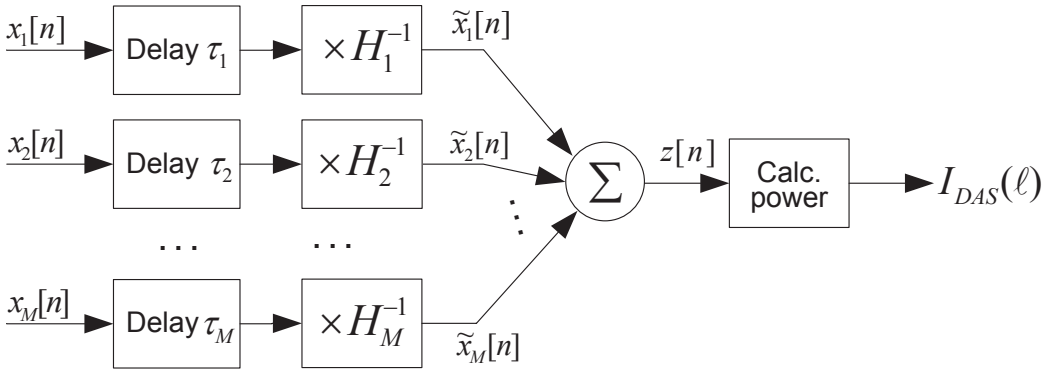

Fig. 3.2 Delay-and-sum beamformer block-diagram.

where v_{ts} (propagation speed in breast tissues) is defined as in (3.8).

Next, the focused signals are summed together producing the beamformer output:

$$z_\ell[n] = \frac{1}{M}\sum_{m=1}^{M} \widetilde{x}_{m,\ell}[n] \quad . \tag{3.39}$$

Finally, the beamformer output power is computed and stored as the image voxel value $I_{DAS}(\ell)$:

$$I_{DAS}(\ell) = \frac{1}{N}\sum_{n=1}^{N} (z_\ell[n])^2 \quad . \tag{3.40}$$

Several variations of the DAS algorithm have been presented in the literature. For example, Li et al. [94, 177] employ specific shape of the transmitted pulse (differentiated Gaussian), which has a zero-crossing at the focal point. In order to make use of the coherent summation, as in (3.39), the focused signals are first integrated over time. Then, only the values of the integrated signals at focal points are summed across the channels, disregarding all other values of the waveforms. The research described in this thesis follows the traditional beamforming approach, described by equations (3.39) and (3.40).

Additional improvement for the DAS and other beamforming algorithms can be reached if the focused signals are time-gated before summation to isolate the reflection at the focal point. This windowing technique helps reduce the contributions of the noise outside of the window.

The compensation delay $\tau_{m,\ell}$ defined in (3.38) is, in general, a real value. Since digital imaging algorithms are considered, there are two ways to apply the time-delay compensation:

1. Coarse time-alignment: the real value of the τ is rounded to the nearest integer and the signal is shifted by the rounded number of samples. This type of alignment is used in the DAS algorithms with the **s**ample-by-sample coarse time alignment (DASs).

2. Fine time-alignment: in order to obtain the delayed version of the signals signal interpolation is applied, which yields the DAS algorithm with the **i**nterpolation time-alignment (DASi). This technique is beneficial when the sampling rate of the recorded signals is not high. Interpolation procedure usually significantly increases the computation time.

Delay-multiply-and-sum beamforming

The Delay-Multiply-And-Sum (DMAS) algorithm [127] is a version of the DAS algorithm, which performs coupled cross-multiplication on the recorded signals $\mathbf{x}$. It has been demonstrated that this technique helps reduce clutter in the microwave images, thereby improving the signal-to-noise ratio and tumor detection performance.

After compensation (3.37) has been applied to focus the signals to the focal point ℓ, the signals are cross-multiplied prior to the summation and (3.39) becomes:

$$z_\ell[n] = \frac{1}{M(M-1)} \sum_{m=1}^{M} \sum_{\substack{k=1 \\ k \neq m}}^{M} \widetilde{x}_{m,\ell}[n] \widetilde{x}_{k,\ell}[n] \quad . \tag{3.41}$$

The beamformer output power for the DMAS is computed using equation (3.40). Further, in chapter 6.2.1 an optimized mathematical expression is presented that significantly improves the computational efficiency of the DMAS and brings the order of computations down to

that of the conventional DAS algorithm.

3.6.2 Spatial focusing with compensation: filter-and-sum beamforming

One significant limitation associated with the DAS algorithm is that it cannot take into account frequency-dependent properties of dispersive propagation media. This drawback can be addressed by a Filter-And-Sum beamforming (FAS) (also known as space-time beamforming). The algorithm is depicted in Fig. 3.3.

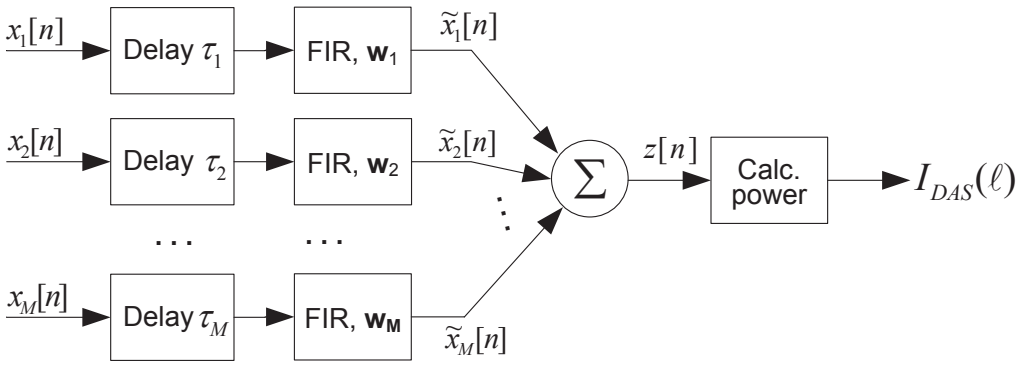

Fig. 3.3 Filter-and-sum beamformer block-diagram.

The essential difference from the DAS algorithm is that the amplitude compensation in (3.37) is augmented or replaced with FIR filtering. The FIR filter is designed to compensate the effects of attenuation (due to spreading and lossy medium), dispersion of the medium as well as to mitigate the effects of coarse time-alignment. Equation (3.37) for FAS beamformer then becomes:

$$\widetilde{x}_{m,\ell}[n] = \sum_{k=n-K}^{n+K} w_m[k-n]x[k+\tau_{m,\ell}] \qquad , \tag{3.42}$$

where w_m are FIR coefficients and $2K+1$ is the filter length. The FIR filter weights w_m are found as the solution to the wide-band problem to equalize path length dependent attenuation and dispersion, mitigate errors introduced by the coarse-time alignment, and

bandpass-filter the signals, as described in [75]. The authors in [75] report that the filtering procedure effectively compensates the effects of dispersion for broad-band processing and improves the imaging result.

The disadvantages of the FAS beamforming include the increased computational resources associated with the filter design for each focal point ℓ. Next, the regularization procedure, required to compute the filter weights, produces results far from optimal since the regularization constants are fixed. In essence, the FAS algorithm is an improved DAS algorithm with the additional compensation of some of its drawbacks, rather than an algorithm that is built on a different principle.

3.6.3 Robust beamforming

Data-independent beamformers rely only on *apriori* known information, often not available in completeness, about the propagation environment and other system properties. In order to obtain high detection performance, imaging algorithms to be employed in the experimental system, thus, must be robust to the uncertainties of the parameters.

As before, the signals are first pre-processed to remove the direct pulse and the skin-breast artifact. Then the compensation is applied as shown in Fig. 3.3. Further, the following signal model is considered. Each signal $\mathbf{x}_m$ is represented as a sum of a backscattered signal $s[n]$, scaled by a focusing vector $\mathbf{a}$, and error $\mathbf{e}$, comprised of both interference (primarily due to clutter) and noise. The focusing vector $\mathbf{a}$ is assumed to be equal to a unit-vector $[1, 1 \ldots 1]$ since all of the signals are aligned. However, due to uncertainties in propagation parameters there are errors in the calculation of the time shift $\tau_m(\mathbf{r})$ and the assumed focusing vector $\tilde{\mathbf{a}}$ is, thus, slightly deviated from $\mathbf{a}$.

Deviations of an assumed focusing vector $\tilde{\mathbf{a}}$ from the actual $\mathbf{a}$ may cause significant degradation of the resulting beamforming performance. Thus, the robust beamforming approach seeks to find optimal values of $\mathbf{a}$ and to adjust the filtering coefficients $\mathbf{w}$ appropriately, in order to compensate for these uncertainties.

Several formulations of the robust beamformers applicable to UWB breast imaging have been proposed in the literature.

Lorenz and Boyd in [178, Chapter 1] formulate the Robust Minimum-Variance Beamformer (RMVB), which is based on the adaptive Capon's method, also known as Standard Capon Beamformer (SCB). The beamformer weights are obtained by solving an optimization task to minimize the weighted power output of the array in the presence of uncertainties in $\mathbf{a}$ limited by a hyper-ellipsoid $\mathcal{E}$:

$$\begin{aligned} &\text{minimize} \quad \mathbf{w}^H \mathbf{R}_x \mathbf{w} \\ &\text{subject to} \quad Re\{\mathbf{w}^H \tilde{\mathbf{a}}\} \geq 1 \; \forall \; \tilde{\mathbf{a}} \in \mathcal{E} \end{aligned} \quad , \tag{3.43}$$

where $\mathbf{R}_x$ is a sample covariance matrix estimated from the last P received samples as follows:

$$\mathbf{R}_x = \frac{1}{P} \sum_{n=N-P+1}^{N} \mathbf{x}(n)\mathbf{x}^H(n) \; \in \mathcal{C}^{M \times M} \quad . \tag{3.44}$$

The solution to this problem can be given by Lagrange multiplier method [178, Chapter 1].

Gershman et al. [178, Chapter 2] follow similar approach by setting the optimization task to maximize the output beamformer Signal-to-Interference-and-Noise Ratio (SINR), estimated by:

$$SINR = \frac{\sigma_s^2 \|\mathbf{w}^H \tilde{\mathbf{a}}\|^2}{\mathbf{w}^H \mathbf{R}_x \mathbf{w}} \quad . \tag{3.45}$$

Bounding the norm of the variation of the focusing vector $\boldsymbol{\delta} = \tilde{\mathbf{a}} - \mathbf{a}$ to some pre-defined constant ϵ, the worst-case SINR is maximized:

$$\max_{\mathbf{w}} \min_{\boldsymbol{\delta}} \frac{\sigma_s^2 \|\mathbf{w}^H (\tilde{\mathbf{a}} + \boldsymbol{\delta})\|^2}{\mathbf{w}^H \mathbf{R}_x \mathbf{w}} \quad \text{subject to } \|\boldsymbol{\delta}\| \; \leq \; \epsilon \quad . \tag{3.46}$$

The solution to this task is given by:

$$\mathbf{w} = \left(\mathbf{R}_x + \frac{\epsilon}{\|\mathbf{w}\|} \mathbf{I} \right)^{-1} \tilde{\mathbf{a}} \quad , \tag{3.47}$$

where $\|\mathbf{w}\|$ can be found by applying an eigenvalue decomposition and Newton-Raphson methods as described in [178, Chapter 2]. This leads to the robust variation of the

Minimum-Variance Distortion-less Response (MVDR) beamformer.

Stoica et al. [178, Chapter 3], in contrast to the spatial filtering formulation of SCB considered in two previous approaches, couple the covariance fitting formulation of SCB with ellipsoidal or spherical uncertainty sets to obtain Robust Capon Beamformer (RCB). Several formulations of the RCB have been proposed so far, which differ in the types of constraints.

The covariance fitting formulation of SCB considers maximization of the beamformer output power $\sigma^2 = \mathbf{w}^H \mathbf{R}_x \mathbf{w}$ while limiting the residual sample covariance matrix to be positive semidefinite:

$$\max_{\sigma^2} \sigma^2 \quad \text{subject to } \mathbf{R}_x - \sigma^2 \mathbf{a}\mathbf{a}^H \geq 0 \qquad , \tag{3.48}$$

where the notation $\mathbf{A} \geq 0$ denotes that $\mathbf{A}$ is positive semidefinite ($\mathbf{A}$ is an arbitrary matrix).

Robust version of the beamformer above is given by including $\tilde{\mathbf{a}}$ as an optimization parameter and applying additional constraint to the focusing vector of one of the following types:

- Single Constraint Robust Capon Beamformer (SCRCB): in case of non-degenerate ellipsoidal uncertainty approach the additional constraint is $(\mathbf{a} - \tilde{\mathbf{a}})^H \mathbf{C}^{-1} (\mathbf{a} - \tilde{\mathbf{a}}) \leq 1$. Flat ellipsoidal uncertainty set introduces the following constraint: $\mathbf{a} = \mathbf{B}\mathbf{u} + \tilde{\mathbf{a}}$, $\|\mathbf{u}\| \leq 1$, where $\mathbf{B}$ is an $M \times L$ matrix ($L < M$) with full column rank and $\mathbf{u}$ is an $L \times 1$ vector.

- Norm Constraint Robust Capon Beamformer (NCRCB) explicitly limits the norm of the weight vector: $\|\mathbf{w}\|^2 \leq \zeta$. The first constraint in this case is considered from the spatial filtering formulation, as $\mathbf{w}^H \tilde{\mathbf{a}} = 1$.

- Double Constraint Robust Capon Beamformer (DCRCB): Spherical uncertainty set is considered and the norm of the focusing vector is limited to an arbitrary constant:

$$\begin{aligned} \|\mathbf{a} - \tilde{\mathbf{a}}\|^2 &\leq \epsilon \quad , \\ \|\mathbf{a}\|^2 &= M \quad . \end{aligned} \tag{3.49}$$

Solutions to the described optimization problems are given in [178, Chapter 3]. It is claimed that the RCB is simpler and computationally more efficient than its equivalent counterparts presented in [178, Chapter 1-2]. Moreover, in contrast to the formulations of RMVB and the robust MVDR, RCB provides a simple way of eliminating the scaling ambiguity while estimating the power of the desired signal.

The RCB approach with the spherical uncertainty set has been applied to the microwave breast cancer detection problem in [141] and extended to multistatic scenario in [143]. The results demonstrate increased performance of this method compared to previously studied non-robust methods. It is also noted [178, Chapter 3] that DCRCB is the preferable beamformer for the applications demanding high SINR, while RCB is the favored one for the applications requiring accurate signal power estimation.

3.7 Performance metrics

Quantitative comparison of the imaging algorithm performance is not possible without appropriate metrics. In the here-reported work, the following metrics will be used to assess the algorithms.

Correct Detection is a binary measure which shows if the location emphasized by the algorithm (image maximum) is associated with the reflections from tumor rather than from the clutter. In order to verify this, the image of the healthy breast model is subtracted from the image of the breast model with a tumor inside. If the peak of the resulting image is within the 10-mm radius circle around the one detected by the algorithm in the tumorous image, the detection is treated as correct. Otherwise, it is assumed that the resulting image provides a misleading detection and is omitted in the subsequent analysis. Metrics presented further are only valid and computed in the cases of the correct detection.

Signal-to-Interference-and-Noise Ratio (SINR) - This metric is defined as

$$\mathrm{SINR} = 20 \log \left(I_{\max,s} / I_{\max,n} \right) \quad , \tag{3.50}$$

where $I_{\max,s}$ and $I_{\max,n}$ correspond to the peak amplitudes of the tumorous and healthy images, respectively. The SINR is an important metric for the detection purpose which

shows the capability of the algorithms to discriminate tumorous breasts from healthy breasts.

Localization error (E_l) - Shows the distance between the true tumor location $\mathbf{c}$ and the one estimated by the algorithm $\hat{\mathbf{c}}$:

$$E_l = \|\mathbf{c} - \hat{\mathbf{c}}\| \quad . \tag{3.51}$$

Peak-to-SideLobe Ratio (PSLR) - This metric is defined as

$$\mathrm{PSLR} = 20 \log \left(I_{\max,s} / I_{sl} \right) \quad , \tag{3.52}$$

where I_{sl} is the most significant sidelobe amplitude of a tumorous image.

PSLR shows the level of artifacts surrounding the main lobe, corresponding to the tumor. It can be useful to estimate the amount of distortion (the "sidelobe" level) introduced by an imaging algorithm. The sidelobes can deteriorate the overall performance by amplifying the clutter effects at the locations of sidelobes.

Maximum-Size-at-Half-Maximum (MSHM) - This metric is defined as the distance between two furthest points on a contour of the main lobe at -3 dB level in a tumor-containing image. MSHM is a metric to evaluate the resolution achievable by the imaging algorithms. Larger values of MSHM evidence for lower resolution as the tumor appears more "smeared" in the output image, thereby reducing the capability of the algorithm to distinguish between two closely located scatterers. It is expected for the MSHM to increase while the dielectric contrast is being reduced.

3.8 Chapter summary

This chapter presented the general problem of microwave breast cancer detection and imaging. Several models of the recorded microwave signals were discussed.

Further, a theoretical background of wave propagation models in lossy media was provided, followed by the description of the associated physical effects, such as delay, attenuation, spreading and scattering.

In order to present imaging algorithms, several array signal models were introduced, each convenient for a particular type of algorithm set.

The main part of the chapter described the MWI algorithms. In particular, a detection-theoretic approach was presented with the GLRT formulation. Next, beamforming algorithms were discussed, such as the DAS beamformer, FAS beamformer, the DMAS beamformer and the RCB beamformer.

Finally, performance metrics used for the algorithm performance assessment were defined.

Chapter 4

Microwave radar and microwave-induced thermoacoustics: dual-modality approach for breast cancer detection

Several promising microwave breast cancer detection techniques, intended to complement conventional methods such as X-ray mammography and Magnetic Resonance Imaging (MRI), have been under development for the past decade. In addition to the evolution of the Ultra**w**ide-Band (UWB) Micro**w**ave Radar (MWR) described in the previous chapter, another kind of imaging that utilizes microwaves has been under investigation. Micro**w**ave-Induced Thermoacoustics (MWIT) [94, 179] imaging exploits the contrast in the conductive loss between malignant and healthy tissue and holds the promise of a high spatial resolution due to the short acoustic wavelength [179, 180]. Similarly to MWR, MWIT technique is based on illumination of the breast with microwaves. However, in contrast to MWR, the microwaves are used to achieve selective heating of tumorous areas due to the contrast in the conductive loss. This leads to expansion of these areas, which produces acoustic waves, recorded with transducers. Processing of the collected signals gives the images, representing the absorption of microwave energy inside the breast.

The research work described further in this thesis demonstrates that the combination of

these two modalities can potentially provide better detection performance than each of the above techniques alone. This chapter describes the methodology and the results of the developed microwave dual-modality detection technique.

A number of significant steps have been made to address the essential problems related to both MWR and MWIT technologies. To summarize, Fear et al. proposed one of the early microwave radar breast cancer detection systems in [94]; the delay-and-sum algorithm was used for imaging and detection. Bond et al. developed beamforming algorithms [75] and Davis et al. developed hypothesis testing algorithms [76]. Williams et al. developed complementary processing techniques including artifact removal and skin surface identification [114]. Klemm et al. [181] described an experimental system and reported on its evaluation on realistic breast models and patients. Xie et al. strived to improve the robustness of detection for the MWR method in [143]; a similar methodology was applied to the MWIT modality in [95]. Xu and Wang demonstrated the feasibility of the MWIT technique for imaging biological tissues in [180], and Kruger et al. described the first hardware device for MWIT-based breast imaging in [179].

Recent experimental works show that certain challenges related to both MWR and MWIT imaging remain unresolved or resolved only partially, which demands further investigations in the field of microwave breast cancer detection. For example, a major problem associated with the MWR method is high level of tissue heterogeneity, which leads to increased amount of clutter in the recorded signals and results in low tumor detection rates. Uneven heating related to the MWIT technique introduces high degree of uncertainty and increases false positives.

No attempts have been made to fuse the MWR and MWIT modalities together into a single imaging system, which is the purpose of this research study. Further discussion is based on the assumption that the measurement noises, experienced when applying these two techniques, are independent because they rely on different physical characteristics. This work develops a methodology to process the input signals jointly based on a hypothesis testing framework and proposes two different test statistics. In order to set the threshold for detection, the distributions of the test statistics are derived. The proposed methodology is evaluated on numerically simulated signals acquired by applying the FDTD method to a set of two-dimensional breast models. These models have a realistic distribution of tissue derived from MRI images. The results of the dual-modality detection method demonstrate

significant improvement in the detection performance.

The rest of the chapter is organized as follows. Section 4.1 presents the dual-modality detection scheme and defines the problems to be addressed. The details of the proposed methodology are provided in section 4.2. The numerical simulation process is described in section 4.3. Implementation details and the results are discussed in section 4.4. Finally, a summary of the chapter is presented in section 4.5.

4.1 Problem statement

In the problem of dual-modality breast cancer detection, a scenario discussed in section 3.1 is considered. A patient lies on a test-bed in a prone position with the breast naturally hanging down into a radome with antennas and acoustic transducers surrounding the breast. Fig. 4.1 shows a simplified dual-modality detection scheme as a coronal slice of one of the breasts of the patient and one of the antennas/acoustic transducers.

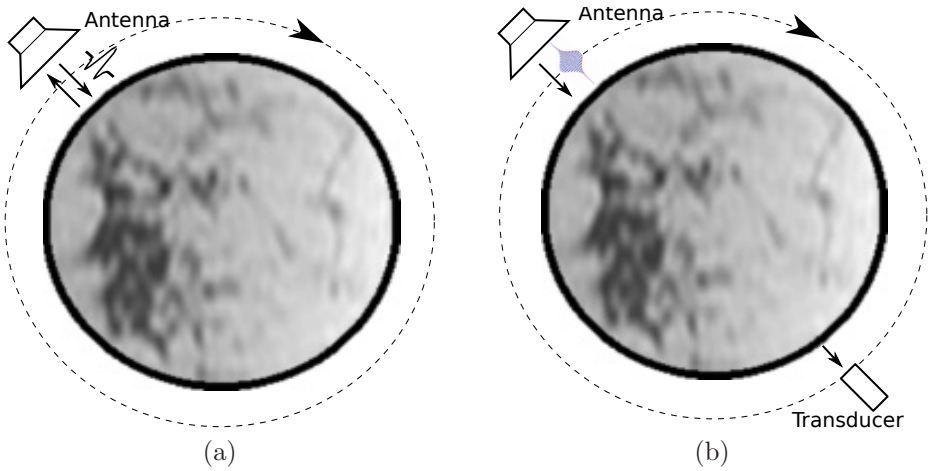

Fig. 4.1 Schematic representation of the proposed dual-modality breast cancer detection method: a) Microwave radar mode; b) Micorwave-induced thermoacoustics mode.

A two-stage monostatic data acquisition system is considered. At the first stage the system works in the MWR mode (Fig. 4.1a): sequentially for each of M_1 antennas, a wideband microwave pulse is radiated toward the breast and the reflected signal is collected with the same antenna (recorded in N_1 samples).

At the second stage (MWIT mode), 800 MHz microwave modulated pulses of a microsecond duration are radiated to heat the breast from M_2 angles. The induced acoustic signals are received by the transducer on the opposite side of the breast (N_2 samples). The MWIT mode requires a relatively large acoustic transducer to receive the signals; the alternative, simpler scenario can be implemented with just one microwave antenna and one acoustic transducer at the opposite side of the breast (as suggested in Fig. 4.1b), rotated mechanically around the breast.

Signals recorded for both MWR and MWIT modes have several components. In the MWR case, signals contain direct pulses (see chapter 3), reflections from the skin-breast interface, reflections from the internal tissue (clutter) as well as the measurement noise. Similar components are relevant for the MWIT signals, except for the direct pulse, since the MWIT signals are induced rather than reflected. The incident antenna pulses are removed from the MWR signals by subtracting the known calibration signal (recorded beforehand without the patient on the test-bed).

In this study, the removal of the skin-breast artifact for both MWR and MWIT signals is accomplished by a modification of the algorithm described by Bond et al. in [75]. The pre-processing procedures yield a set of column-vectors $\mathbf{x}_i = [x_{i,1}, \ldots, x_{i,N_1}]^T$, $i = 1 \ldots M_1$ which represent the MWR signals and another set of column-vectors $\mathbf{u}_j = [u_{j,1}, \ldots, u_{j,N_2}]^T$, $j = 1 \ldots M_2$ for the MWIT signals. A case with $N_1 = N_2 = N$ and $M_1 = M_2 = M$ is considered further in this work and indices i, j are replaced further with common channel index m for convenience.

This research work adopts the detection-theoretic approach of hypothesis testing, based on the analysis of a test statistic. The goal of this study is to develop an optimal way to process the signals $\mathbf{x}$ and $\mathbf{u}$ jointly. A test statistic for the dual-modality approach is derived and its null-hypothesis distribution is analyzed, for the purpose of setting a threshold for detection. For assessment purposes, MWR and MWIT single-modality test statistics are also computed. The dual-modality approach is evaluated on a set of signals acquired from numerical simulations of the described test-bed. Structurally-realistic breast models with multiple settings of the dielectric tissue properties are constructed for the simulations to examine the impact of low contrast and high clutter.

4.2 Methodology

4.2.1 Signal models and assumptions

Signal model described in (3.27) is considered for both MWR and MWIT signals:

$$\mathbf{x}_m = \sum_{\ell=1}^{L} \alpha_\ell \mathbf{s}_{\ell,m} + \boldsymbol{\xi}_m \quad ; \tag{4.1}$$

$$\mathbf{u}_m = \sum_{\ell=1}^{L} \eta_\ell \mathbf{d}_{\ell,m} + \boldsymbol{\zeta}_m \quad . \tag{4.2}$$

In the expression above, $\mathbf{d}_{\ell,m}$ is the induced pressure signal in contrast to $\mathbf{s}_{\ell,m}$, which is the back-scattered microwave pulse. Other variables are explained in section 3.4.2.

The GLRT algorithm, described in section 3.5, is applied to both of the signals (4.1) and (4.2), which results in the images of the following test statistics:

$$U(\mathbf{x}) = \frac{\mathbf{x}^H \mathbf{P}_\mathbf{s} \mathbf{x}}{\mathbf{x}^H \mathbf{P}_\mathbf{s}^\perp \mathbf{x}} \quad ; \qquad V(\mathbf{u}) = \frac{\mathbf{u}^H \mathbf{P}_\mathbf{d} \mathbf{u}}{\mathbf{u}^H \mathbf{P}_\mathbf{d}^\perp \mathbf{u}} \quad , \tag{4.3}$$

where U denotes the test statistic for MWR modality, V denotes the test statistic for the MWIT modality and matrices $\mathbf{P}$, $\mathbf{P}^\perp$ are described in section 3.5.

In order to fuse MWR and MWIT methods together, the noise components $\boldsymbol{\xi}_m$ and $\boldsymbol{\zeta}_m$ are modeled as jointly Gaussian with zero means and covariances $\sigma_{\boldsymbol{\xi}}^2 \mathbf{R}_{\boldsymbol{\xi}}$ and $\sigma_{\boldsymbol{\zeta}}^2 \mathbf{R}_{\boldsymbol{\zeta}}$, where matrices $\mathbf{R}_{\boldsymbol{\xi}}$ and $\mathbf{R}_{\boldsymbol{\zeta}}$ capture the structural properties of the covariance, and scalars $\sigma_{\boldsymbol{\xi}}^2$ and $\sigma_{\boldsymbol{\zeta}}^2$ specify the noise powers. The noise components are assumed to be independent between the channels and between the MWR and MWIT methods. It is assumed that $\mathbf{R}_{\boldsymbol{\xi}}$ and $\mathbf{R}_{\boldsymbol{\zeta}}$ can be estimated using a training data set containing responses from a number of healthy breasts.

As discussed in section 3.5, the concatenation of vectors $\mathbf{x}_m$ is further represented in the form of a single NM-length vector $\mathbf{x}$. Similarly, vectors $\mathbf{u}$, $\mathbf{s}$, $\mathbf{d}$ represent NM-length vectors of concatenated vectors $\mathbf{u}_m$, $\mathbf{s}_m$, and $\mathbf{d}_m$, respectively.

4.2.2 Hypothesis testing and generalized likelihood ratio test

In as similar way as described in section 3.5, at each scan location $\ell = 1, \ldots, L$, a binary hypothesis test of a tumor presence is performed (hypothesis $\mathcal{H}_\ell^{(1)}$) versus null-hypothesis ($\mathcal{H}_\ell^{(0)}$) for the joint MWR/MWIT breast tumor detection as follows:

$$\mathcal{H}_\ell^{(0)}: \ \alpha_\ell, \eta_\ell = 0 \qquad \text{vs.} \qquad \mathcal{H}_\ell^{(1)}: \ \alpha_\ell, \eta_\ell \neq 0 \quad . \tag{4.4}$$

The detection problem is defined in the same way as in section 3.5 and the signals are whitened accordingly:

$$\widetilde{\mathbf{x}} = \hat{\mathbf{R}}_{\boldsymbol{\xi}}^{-1/2}\mathbf{x} \quad ; \qquad \widetilde{\mathbf{u}} = \hat{\mathbf{R}}_{\boldsymbol{\zeta}}^{-1/2}\mathbf{u} \qquad . \tag{4.5}$$

The clutter covariance matrices are estimated from a training set of (available) ten tumor-free breasts, using the averaging. For simplicity, further discussion will use variables $\mathbf{x}$ and $\mathbf{u}$ assuming these signals are whitened. Further, the derivations for one given location are considered, and the index ℓ is omitted.

The dual-modality GLRT performs the comparison of the generalized likelihood ratio $L_G(\mathbf{x}, \mathbf{u})$ against a threshold γ:

$$L_G(\mathbf{x}, \mathbf{u}) \underset{\mathcal{H}_0}{\overset{\mathcal{H}_1}{\gtrless}} \gamma \quad . \tag{4.6}$$

$L_G(\mathbf{x}, \mathbf{u})$ can be factorized under the assumption that the noises are independent:

$$L_G(\mathbf{x}, \mathbf{u}) = \frac{p(\mathbf{x}|\hat{\alpha}_1, \hat{\sigma}^2_{\boldsymbol{\xi},1}, \mathcal{H}_1) p(\mathbf{u}|\hat{\eta}_1, \hat{\sigma}^2_{\boldsymbol{\zeta},1}, \mathcal{H}_1)}{p(\mathbf{x}|\hat{\sigma}^2_{\boldsymbol{\xi},0}, \mathcal{H}_0) p(\mathbf{u}|\hat{\sigma}^2_{\boldsymbol{\zeta},0}, \mathcal{H}_0)} \qquad , \tag{4.7}$$

where variables with the hat symbol and sub-indices 0 and 1 denote Maximum Likelihood Estimates (MLE) under null- and alternative hypotheses respectively, which are given by [175, Appendix 9A]:

$$\hat{\alpha}_1 = \left(\mathbf{s}^H\mathbf{s}\right)^{-1}\mathbf{s}^H\mathbf{x} \quad ; \qquad \hat{\eta}_1 = \left(\mathbf{d}^H\mathbf{d}\right)^{-1}\mathbf{d}^H\mathbf{u} \qquad , \tag{4.8}$$

$$\hat{\sigma}^2_{\boldsymbol{\xi},1} = \frac{1}{NM}\mathbf{x}^H\left(\mathbf{I} - \mathbf{P}_\mathbf{s}\right)\mathbf{x} \quad ; \qquad \hat{\sigma}^2_{\boldsymbol{\xi},0} = \frac{1}{NM}\mathbf{x}^H\mathbf{x} \qquad , \tag{4.9}$$

$$\hat{\sigma}^2_{\boldsymbol{\zeta},1} = \frac{1}{NM}\mathbf{u}^H\left(\mathbf{I} - \mathbf{P}_\mathbf{d}\right)\mathbf{u} \quad ; \qquad \hat{\sigma}^2_{\boldsymbol{\zeta},0} = \frac{1}{NM}\mathbf{u}^H\mathbf{u} \qquad . \tag{4.10}$$

In these expressions $\mathbf{I}$ denotes the identity matrix and $\mathbf{P_s} = \mathbf{s}\left(\mathbf{s}^H\mathbf{s}\right)^{-1}\mathbf{s}^H$ and $\mathbf{P_d} = \mathbf{d}\left(\mathbf{d}^H\mathbf{d}\right)^{-1}\mathbf{d}^H$ represent projection matrices that project a vector onto the signal subspace.

Making use of the MLE expressions in (4.7) and considering Gaussian distributions, results in the following likelihood ratio:

$$\begin{aligned} L_G(\mathbf{x},\mathbf{u}) &= \left(\frac{\hat{\sigma}^2_{\boldsymbol{\xi},0}}{\hat{\sigma}^2_{\boldsymbol{\xi},1}}\right)^{\frac{NM}{2}} \times \left(\frac{\hat{\sigma}^2_{\boldsymbol{\zeta},0}}{\hat{\sigma}^2_{\boldsymbol{\zeta},1}}\right)^{\frac{NM}{2}} \\ &= \left(\frac{\mathbf{x}^H\mathbf{x}}{\mathbf{x}^H\left(\mathbf{I}-\mathbf{P_s}\right)\mathbf{x}}\right)^{\frac{NM}{2}} \times \left(\frac{\mathbf{u}^H\mathbf{u}}{\mathbf{u}^H\left(\mathbf{I}-\mathbf{P_d}\right)\mathbf{u}}\right)^{\frac{NM}{2}} \\ &= \left(\Lambda(\mathbf{x}) \times \Lambda(\mathbf{u})\right)^{\frac{NM}{2}} \quad . \end{aligned} \tag{4.11}$$

Substituting this into (4.6) and noting that $(\cdot)^{\frac{NM}{2}}$ is a monotonically increasing function, results in the following decision rule:

$$\tilde{Z}(\mathbf{x},\mathbf{u}) = \Lambda\left(\mathbf{x}\right)\Lambda\left(\mathbf{u}\right) \underset{\mathcal{H}_\ell^{(0)}}{\overset{\mathcal{H}_\ell^{(1)}}{\gtrless}} \tilde{\gamma} \qquad , \tag{4.12}$$

For a fixed probability of false alarm, the threshold $\tilde{\gamma}$ can be determined from the inverse Cumulative Distribution Function (CDF) of the test statistic $\tilde{Z}(\mathbf{x},\mathbf{u})$ (see section 4.2.4).

It can be shown that $\tilde{Z}(\mathbf{x},\mathbf{u})$ can be expanded as follows:

$$\tilde{Z}(\mathbf{x},\mathbf{u}) = 1 + U\left(\mathbf{x}\right)V\left(\mathbf{u}\right) + U\left(\mathbf{x}\right) + V\left(\mathbf{u}\right) \qquad . \tag{4.13}$$

In order to eliminate the bias term in $\tilde{Z}$, the constant "1" is subtracted from (4.13), which results in:

$$Z(\mathbf{x},\mathbf{u}) = U\left(\mathbf{x}\right)V\left(\mathbf{u}\right) + U\left(\mathbf{x}\right) + V\left(\mathbf{u}\right) \qquad . \tag{4.14}$$

4.2.3 Heuristic test statistic

This work also considers a heuristic alternative to $Z(\mathbf{x},\mathbf{u})$. Since U and V are likelihood ratios, it is intuitive to multiply them to fuse the results of the MWR and MWIT modes:

$$W(\mathbf{x},\mathbf{u}) = U(\mathbf{x})\,V(\mathbf{u}) \quad . \tag{4.15}$$

Later, in section 4.4, it is shown that the $W(\mathbf{x},\mathbf{u})$ statistic provides higher clutter and sidelobe suppression performance than the derived $Z(\mathbf{x},\mathbf{u})$.

4.2.4 Distributions of the test statistics

The distribution of $U(\mathbf{x})$ and $V(\mathbf{u})$ up to a scaling constant under $\mathcal{H}_0$ is given in [175] and is identified to be the central-F with the same degrees of freedom, $c_1 = c_2 = 1$ for the numerator and $d_1 = d_2 = (NM-1)$ for the denominator. Detailed derivation for the CDFs of $W(\mathbf{x},\mathbf{u})$ and $Z(\mathbf{x},\mathbf{u})$ is available in [182].

In brief, the expression for the CDF of $Z(\mathbf{x},\mathbf{u})$ is obtained by considering $Z(\mathbf{x},\mathbf{u})$ in the form of (4.12) and representing it as a product of two identically distributed random variables Z_i of the form $Z_i = (Y_i + X_i)/Y_i$ with $Y_i = \mathbf{x}_i^H \mathbf{P}_{\mathbf{s}_i}^{\perp} \mathbf{x}_i$ and $X_i = \mathbf{x}_i^H \mathbf{P}_{\mathbf{s}_i} \mathbf{x}_i$. Under $\mathcal{H}_0$ they are independent, central chi-square distributed random variables with c_i and d_i degrees of freedom, respectively.

By considering the joint distribution of numerator $\omega = X + Y$ and denominator $\alpha = Y$ and using the Jacobian method for the random variable transformation, the probability density function of Z_i can be represented in terms of Meijer's G-function, as follows [182]:

$$p_{Z_i}(z_i) = \frac{\Gamma(\frac{c_i}{2} + \frac{d_i}{2})}{\Gamma(\frac{c_i}{2})} G_{1,1}^{0,1}\left(z_i \,\middle|\, \begin{matrix} -\frac{c_i}{2} \\ -\frac{c_i}{2} - \frac{d_i}{2} \end{matrix} \right) \quad , \tag{4.16}$$

where Γ denotes the Gamma-function and G is Meijer's G-function [183].

Applying the Jacobian technique again and using the G-function integrating formulas from

[183], it can be shown that the CDF of $Z = Z_1 Z_2$ is:

$$P_Z(z) = \frac{\Gamma(\frac{c_1}{2}+\frac{d_1}{2})\Gamma(\frac{c_2}{2}+\frac{d_2}{2})}{\Gamma(\frac{c_1}{2})\Gamma(\frac{c_2}{2})} \times G_{3,3}^{0,3}\left(z \left| \begin{matrix} 1-\frac{c_1}{2} & , & 1-\frac{c_2}{2} & , & 1 \\ 1-\frac{c_1}{2}-\frac{d_1}{2} & , & 1-\frac{c_2}{2}-\frac{d_2}{2} & , & 0 \end{matrix} \right.\right) \quad . \tag{4.17}$$

The distribution of $W(\mathbf{x}, \mathbf{u})$ under $\mathcal{H}_0$ is the distribution of the product of two centered F-distributed random variables, which can also be expressed in terms of chi-square distributions. The procedure of the derivations uses similar techniques to the ones employed for the $P_Z(z)$ derivation. The moment generating function for W can be expressed in terms of Meijer's G-functions as follows [182]:

$$M_W(\omega) = \frac{G_{3,2}^{2,3}\left(\frac{d_1 d_2}{c_1 c_2 \omega} \left| \begin{matrix} 1, 1-\frac{c_1}{2}, 1-\frac{c_2}{2} \\ \frac{d_1}{2}, \frac{d_2}{2} \end{matrix} \right.\right)}{\Gamma(d_1/2)\Gamma(d_2/2)\Gamma(c_1/2)\Gamma(c_2/2)}, \tag{4.18}$$

where c_1, c_2, d_1, d_2 are the degrees of freedom of the four chi-square random variables.

The inverse Laplace transformation of (4.18) and application of the formulas from [183] give the expression of the CDF:

$$P_W(w) = \frac{G_{3,3}^{2,3}\left(\frac{d_1 d_2}{c_1 c_2} w \left| \begin{matrix} 1-\frac{c_1}{2} & , & 1-\frac{c_2}{2} & , & 1 \\ \frac{d_1}{2} & , & \frac{d_2}{2} & , & 0 \end{matrix} \right.\right)}{\Gamma(d_1/2)\Gamma(d_2/2)\Gamma(c_1/2)\Gamma(c_2/2)} \quad . \tag{4.19}$$

4.2.5 Signal templates

Variables $\mathbf{s}$ and $\mathbf{d}$ in (4.1) and (4.2) represent signal templates, i.e. theoretically derived signals obtained by modeling EM wave propagation in dielectric media. The MWR signal templates $\mathbf{s}$ are obtained using the EM model (3.23). The frequency-domain representation

of the theoretical signal template is modeled by:

$$\mathbf{S}_m(\omega) = G(j\omega)\frac{e^{-2jk_b(\omega)d_{b,m}}}{\sqrt{d_{b,m}}}e^{-jk_{ts}(\omega)(d_{ts,i}+a)} \times \sum_{n=-\infty}^{+\infty}(-j)^n a_n H_n^{(2)}(k_{ts}(\omega)d_{ts,m}) \quad , \tag{4.20}$$

where $G(j\omega)$ denotes the frequency spectrum of the incident wideband Gaussian modulated pulse, the second (rational) term describes the two-way propagation in the background, the third (exponential) term denotes the forward propagation of a plane wave in the tissue, and the fourth (summation) term denotes the scattering by a tumor modeled as a dielectric cylinder [169]. Variables d_b and d_{ts} denote the propagation distances in the background medium and tissue, respectively, and k_b and k_{ts} denote their frequency-dependent wave numbers, respectively. Here, $H_n^{(2)}$ denotes the n^{th}-order cylindrical Hankel function of the second kind, and the coefficient a_n is given by:

$$a_n = \frac{\frac{\epsilon_d}{k_d}J_n(k_{ts}a)J_n^{'}(k_d a) - \frac{\epsilon_{ts}}{k_{ts}}J_n(k_d a)J_n^{'}(k_{ts}a)}{-\frac{\epsilon_d}{k_d}H_n^{(2)}(k_{ts}a)J_n^{'}(k_d a) + \frac{\epsilon_{ts}}{k_{ts}}J_n(k_d a)H_n^{(2)'}(k_{ts}a)} \quad , \tag{4.21}$$

where a is the tumor radius and k_d is the tumor wave number. ϵ_{ts} and ϵ_d are the relative permittivities of the healthy tissue and tumor, respectively, J_n denotes the n^{th}-order cylindrical Bessel function, and $(\cdot)^{'}$ denotes the derivative with respect to the argument of the function. The effect of the skin is not included in the model due to the small electrical size of the skin. This frequency-domain signal template is sampled with a 60 GHz sampling frequency and transformed to the time domain (512 samples).

For the MWIT signal template, it is assumed that the tissue and the matching medium have the same acoustic properties. The acoustic propagation properties include the estimated average acoustic attenuation α_a and acoustic speed c_a. In order to model the finite sizes of the tumor and the acoustic transducer, the induced pressure is integrated among tumor region Ω and the transducer aperture Ψ, respectively. The time-domain signal template models the delay and attenuation [95]:

$$\mathbf{D}_m(t) = \int_{\Psi}\int_{\Omega}\frac{e^{-\alpha_a(d_{b,m}+d_{ts,m})}}{\sqrt{d_{b,m}+d_{ts,m}}}I\left(t - \frac{d_{b,m}+d_{ts,m}}{c_a}\right)d\Omega d\Psi \quad , \tag{4.22}$$

where $I(t)$ is the signal modulating the sinusoidal plane wave.

4.3 Numerical simulations

4.3.1 Breast models

The study described in the chapter considers two-dimensional circular numerical breast models with 80-mm diameter tissue enclosed by a 2.0-mm thick skin as shown in Fig. 4.1. The choice of the two-dimensional models is dictated by the limited computational resource: the simulations required for the MWIT modality are too time-consuming to consider three-dimensional realistic breast models.

Human breast has irregular geometrical shape, which poses challenges for both the skin-breast artifact removal and the estimation of the distances of microwave propagation in each medium. Thus, the circular breast shape is adopted in this work so that the study can focus on the detection problem and leave the problem of irregular breast shape for future research. The dielectric properties of the tissue are derived from ten MRI images [27] and are described by the one-pole Debye model (3.6) with the relative permittivity for infinite value of frequency ϵ_∞, the difference between the infinite and static relative permittivity $\Delta\epsilon$, the static conductivity σ_s, and the relaxation time constant τ.

In order to cover a range of possible average dielectric properties of the healthy breast tissue, $N_s = 9$ series of numerical breast models are considered, with the EM tissue properties defined by the Debye model in [184]. Table 4.1 contains the parameters of the models: Δ_ϵ and τ have been fixed to constant values while ϵ_∞ have been assigned values by linearly mapping the grey-scale MRI pixel intensity as:

$$\epsilon_\infty(p) = \epsilon_{\infty,b}\left(1 + \frac{\nu}{2} - \frac{M(p) - \min(M)}{\max(M) - \min(M)}\nu\right) \quad , \tag{4.23}$$

where p is the pixel number in the MRI image M; ν denotes the percent of variation, which defines the level of heterogeneity (Table 4.1). Exactly the same expression applies to map σ_s. Table 4.2 depicts the exact values of the tissue properties that are used for modeling [185]. The last four columns of Table 4.1 represent the resulting statistics of the generated material maps: the minimum and maximum ratios of the dielectric properties of malignant

to benign tissues evaluated at the central frequency 6.85 GHz using the Debye model. In the considered scenario the breast is immersed in an oil-like coupling medium with $\epsilon_r = 4.8$.

Table 4.1 Tissue properties for data series

Series #	Debye model parameters				$\nu \times 100$	$\min(\epsilon_{r,m}/\epsilon_{r,b})$	$\max(\epsilon_{r,m}/\epsilon_{r,b})$	$\min(\sigma_m/\sigma_b)$	$\max(\sigma_m/\sigma_b)$
	$\epsilon_{\infty,b}$	$\sigma_{s,b}$ (S/m)	Δ_ϵ	τ (ps)					
1	3.1	0.05	1.6	13	7	10.6	11.1	24.8	25.1
2	4.0	0.08	3.5	13	30	6.4	7.7	11.5	11.9
3	4.0	0.08	3.5	13	40	6.3	8.0	11.5	12.0
4	13.0	0.4	24.4	13	30	1.4	1.6	1.7	1.8
5	13.0	0.4	24.4	13	50	1.3	1.7	1.7	1.8
6	13.0	0.4	24.4	13	70	1.3	1.7	1.7	1.8
7	13.8	0.7	35.6	13	10	1.1	1.2	1.2	1.2
8	13.8	0.7	35.6	13	30	1.1	1.2	1.2	1.2
9	14.2	0.8	40.5	13	10	1.0	1.1	1.0	1.0

Five acoustic and thermal properties associated with the breast models have been compiled from [27, 186, 187] and are listed in Table 4.2. Density ρ, acoustic attenuation α_a, heat capacity c_p, and volume expansion coefficient α are assumed constant for each of the propagation media. Acoustic speed c_a is variable to capture the acoustic heterogeneity of the breast tissue. In this study, c_a is mapped from the MRI pixel intensities using (4.23) with $\nu = 0.1$ and $c_{a,b} = 1510$ m/s.

Ten (N_t) different realizations of tissue structure (H1,...,H10) have been used for each of the nine series. H2,...,H10 have been utilized as the training set to capture the distribution of the tissue clutter while H1 has been left to build two tumorous breast models by placing a circular tumor (radius $R = 3$ mm) inside the breast tissue at two positions relative to the center of the breast: [-20 mm;8 mm] (P1) and [15 mm;-15 mm] (P2). These are chosen to illustrate an easier imaging scenario (adipose-dominant area) and a more difficult one (tumor location for P1 has a higher tissue density, which decreases the dielectric contrast and makes the detection task more difficult). Overall, $N_s \times N_t = 9 \times 10 = 90$ healthy and $N_s \times 2 = 9 \times 2 = 18$ tumorous breast models have been considered in this study. An example of the distribution of the permittivity and conductivity for series #8 (tumor location P2) is shown in Fig. 4.2.

Table 4.2 Material parameters, where "-" denotes a pixel-wise mapping from the MRI pixel intensity values to the physical properties. For the background, ϵ_r is given in place of ϵ_∞

	Unit	Background	Skin	Tissue	Tumor
ϵ_∞	unitless	ϵ_r =4.8	15.93	-	6.75
σ_s	(S/m)	0.0	0.831	-	0.79
$\Delta\epsilon$	unitless	N/A	23.83	-	48.35
τ	(ps)	N/A	13	13	10.47
c_a	(m/s)	1452	1615	-	1550
α_a	(dB/m)	95	35	45	41
ρ	(kg/m^3)	950	1100	1020	1182
c_p	J/(kg·K)	1800	3680	2220	3500
α	1/K	$6.3 \cdot 10^{-4}$	$3.0 \cdot 10^{-4}$	$3.0 \cdot 10^{-4}$	$3.0 \cdot 10^{-4}$

4.3.2 Microwave radar simulations

In the MWR simulation, as shown in Fig. 4.1a, transverse-magnetic Gaussian-modulated sinusoidal plane waves polarized in the $+x$ direction (directed from the paper towards the reader as in Fig. 4.1a), with a 3-dB bandwidth of 7.5 GHz, are launched towards a breast model at $M = 36$ equally-spaced angles. The FDTD method is used to solve Maxwell's equations and simulate the plane wave propagation using the analytic field propagator method [188]. The spatial increment is set to 0.4 mm, which leads to 475×450 Yee's cells (the unit element of the spatial grid of the finite-difference computation [189]). In order to truncate the scattered field region, 10 perfectly-matched layers are placed at the boundaries. Each simulation has a time-span of 8.0 ns to ensure that all the scattered microwave energy has left the simulation domain. The result is a vector of scattered signal recorded at each of the M antennas working in the receiving mode.

4.3.3 Microwave-induced thermoacoustic simulations

In the MWIT simulation, as shown in Fig. 4.1b, plane waves at 800 MHz are launched towards the breast model at $M = 36$ angles. Each simulation runs for 8 periods to reach the time-harmonic steady state. The two-point estimation method [190] is applied in order

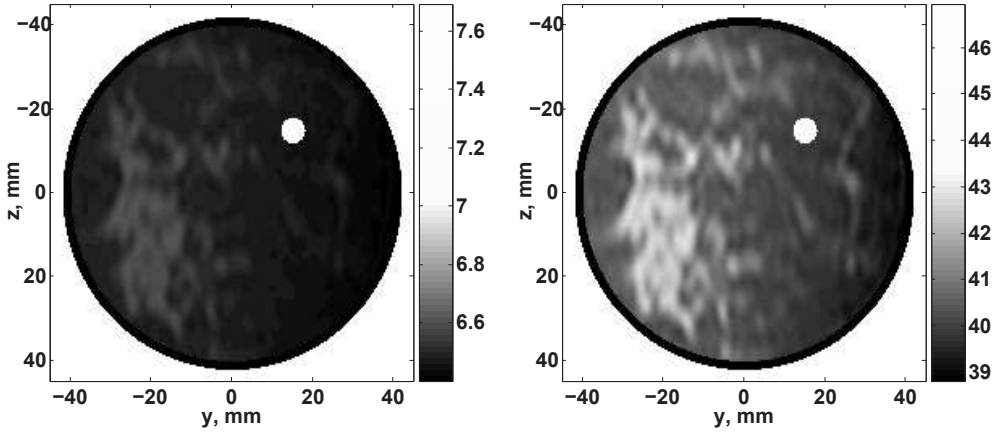

(a) Conductivity, [siemens/meter] (b) Relative Permittivity, [unitless]

Fig. 4.2 Dielectric properties of the numerical breast models evaluated at 6.85 GHz (series #8, tumor at location P2).

to calculate the amplitude of the electric field E_x. The following expression is used to calculate the point-wise Specific Absorption Rate (SAR):

$$S(\mathbf{r}) = \frac{\sigma(\mathbf{r})|E_x(\mathbf{r})|^2}{2\rho(\mathbf{r})} \quad , \tag{4.24}$$

Where $\sigma(\mathbf{r})$ and $\rho(\mathbf{r})$ denote, respectively, the conductivity and density of the breast tissue at location $\mathbf{r}$. The wavelength at 800 MHz in the coupling medium is 171 mm, which is two times larger than the dimension of the breast models. The non-uniform heating due to the comparable electric size of the breast is inherently included in this simulation. The calculation performed by our research group show that the variability of the SAR across the breast domain reaches 15dB.

The SAR is interpolated from the coarse grid for the electromagnetic simulations to the dense grid for the acoustic simulations. The thermoacoustic wave equation is

$$\nabla^2 p - \frac{1}{c_a^2}\frac{\partial^2 p}{\partial t^2} = -\frac{\alpha}{c_p}\frac{\partial}{\partial t}S(\mathbf{r})I(t) \quad , \tag{4.25}$$

where p denotes pressure. The right-hand side of this equation is the spatially dependent SAR multiplied by the temporal envelope $I(t)$, which is a Gaussian function with a 10 dB bandwidth of 1.1 MHz. The spatial increment is set to 0.1 mm, which leads to 1600×1600

Yee's cells. The simulation domain is truncated with 20 perfectly-matched layers. Each acoustic simulation captures a time-span of 150 μs. In order to simulate the finite size of the transducer aperture, the induced acoustic signals are averaged on a 1-cm line tangential to the transducer placement circle, on the side opposite to the incident plane wave.

In order to reflect realistic measurement equipment, Gaussian measurement noise is added to the acquired signals (on the order of -60 dB relative to the signal maximum).

4.4 Results and discussion

For evaluation purposes, this study uses the Peak-to-Sidelobe Ratio (PSLR) metric, defined in section 3.7.

Each of the considered series $1, \ldots, 9$ comprises two tumorous cases (P1 and P2) and a corresponding healthy scenario (H1). Four images of test statistics, one for each of these cases, are computed as described in section 4.2.2: $U(\mathbf{x})$, $V(\mathbf{u})$, $Z(\mathbf{x}, \mathbf{u})$, $W(\mathbf{x}, \mathbf{u})$. Fig. 4.3 illustrates examples of images obtained as the output of the GLRT algorithm corresponding to the breast models depicted in Fig. 4.2. The pixels represent the test statistic values at locations $\ell = 1, \ldots, L$ on the grid with spatial resolution of 1 mm. With the 1-mm grid, around 5100 test locations inside the breast region have been assigned values.

The difference in the spatial distribution of clutter between U and V test statistics is noticeable, which is the principal property that the fusion benefits from. The W test statistic displays considerable clutter suppression (Fig. 4.3c). The clutter- and sidelobe-reduction effects of the W test statistic are also evident in the PSLR metric (Fig. 4.4). The W test statistic provides high clutter-reduction performance for series 2 - 8.

Figure 4.5 depicts the maximum values of the test statistics, obtained for the tumorous (i.e., under hypothesis $\mathcal{H}_1$) and healthy ($\mathcal{H}_0$) cases. An improved detection performance can be observed for the W test statistic with respect to the MWR test statistic U (series 4,5,6 and 8 fall under or very close to the red line γ_{min} that denotes the maximum value of the test statistic across the series under $\mathcal{H}_0$ hypothesis) and V (series 2 and 3 go below γ_{min}) while preserving the detection capability for other series.

The next stage of the tumor detection technique is the thresholding. The thresholds are set based on an estimated distribution for the healthy cases with the goal of minimizing the

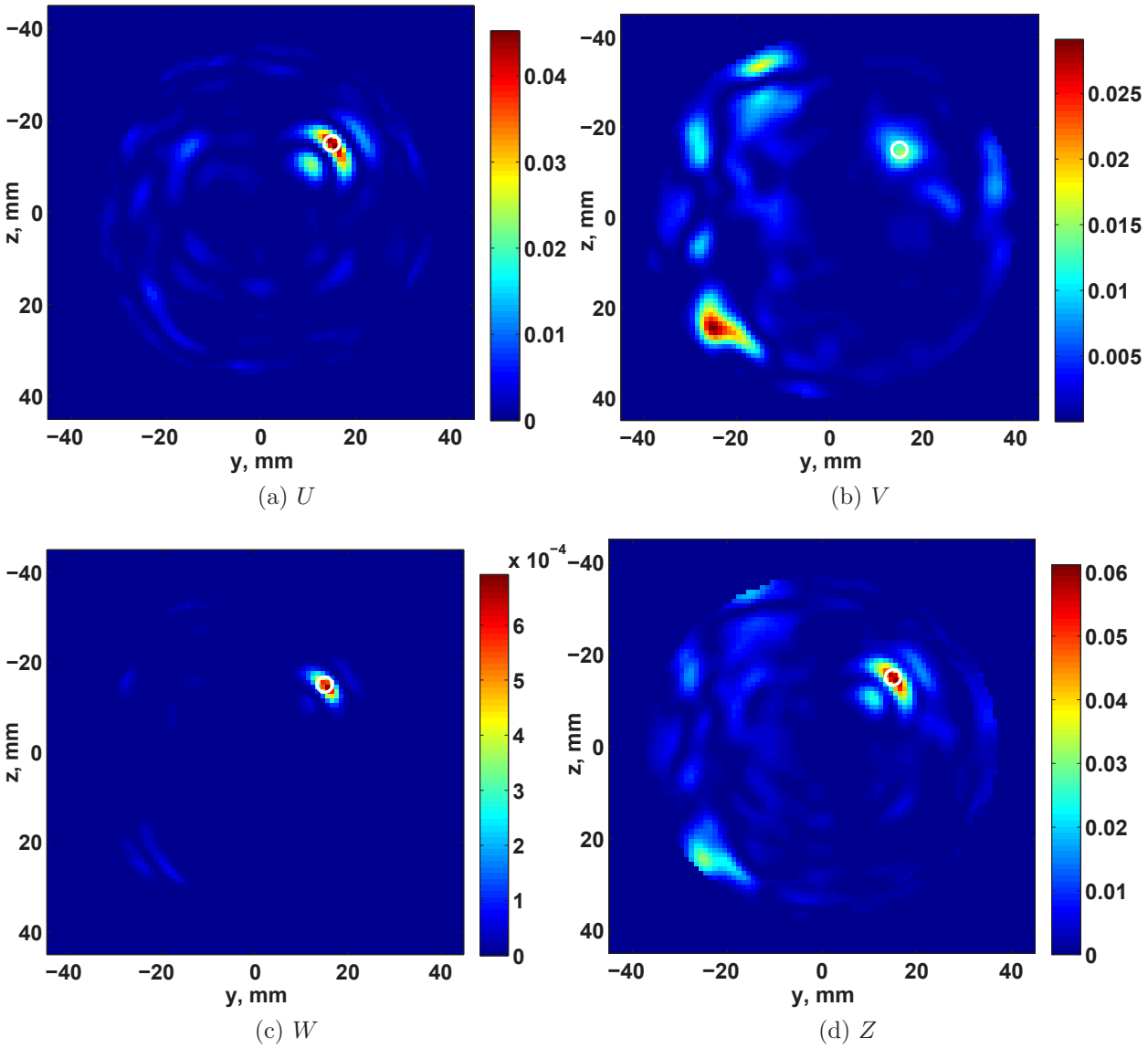

(a) U (b) V

(c) W (d) Z

Fig. 4.3 Examples of images for the four types of test statistics (unitless). Note improvement in clutter suppression for W. Actual tumor location is shown by a circle (tumor position P2).

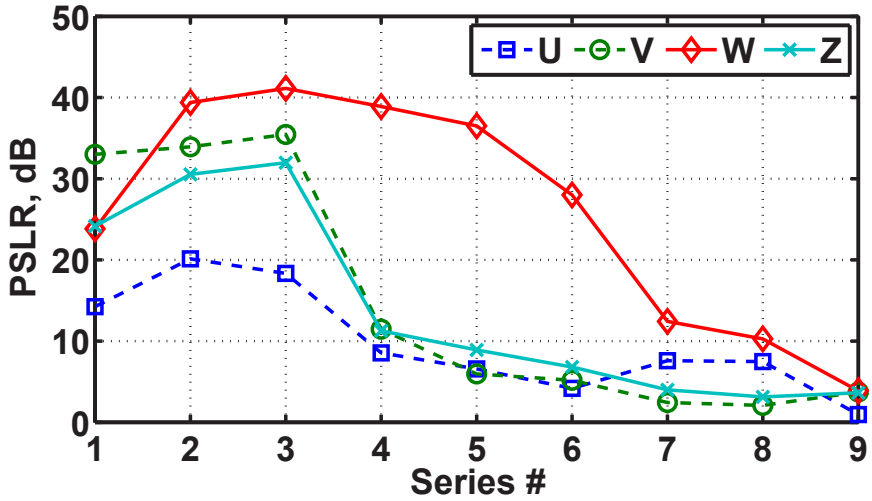

Fig. 4.4 Averaged peak signal-to-sidelobe ratio versus the series number (Table 4.1). The W test statistic provides high performance to reduce the effects of clutter for series 2...8.

Table 4.3 Detection performance for the thresholds given by the qvality tool. The results correspond to tests on 90 healthy cases and 18 tumorous cases

	U	V	W	Z
False alarms	2	1	0	0
Misses	6	8	5	5

False Discovery Rate (FDR). The software package qvality [191] was used to estimate the FDR with respect to the test statistics. For one healthy and two tumorous cases available for each series, the leave-one-out approach was used to set the threshold, i.e., first the threshold was estimated based on the values of the test statistics for cases P2,H2,...,H10 and applied to the test cases P1 and H1; next, the threshold was obtained from P1,H2,...,H10 cases and applied to the test cases P2 and H1. The value of the test statistic with minimum positive q-value was used as the threshold.

Table 4.3 summarizes the detection performance achieved using the described methodology. The values in the table were obtained as follows. Thresholds calculated for each series and mode were applied to the corresponding two tumorous cases and one healthy case. If in the resulting images, pixels of the test statistic in the tumorous area remained above the threshold, this case was considered as a "hit". Otherwise, the result was considered as a "miss". Similarly, if after thresholding of cases H1 (with the two thresholds) some pixels

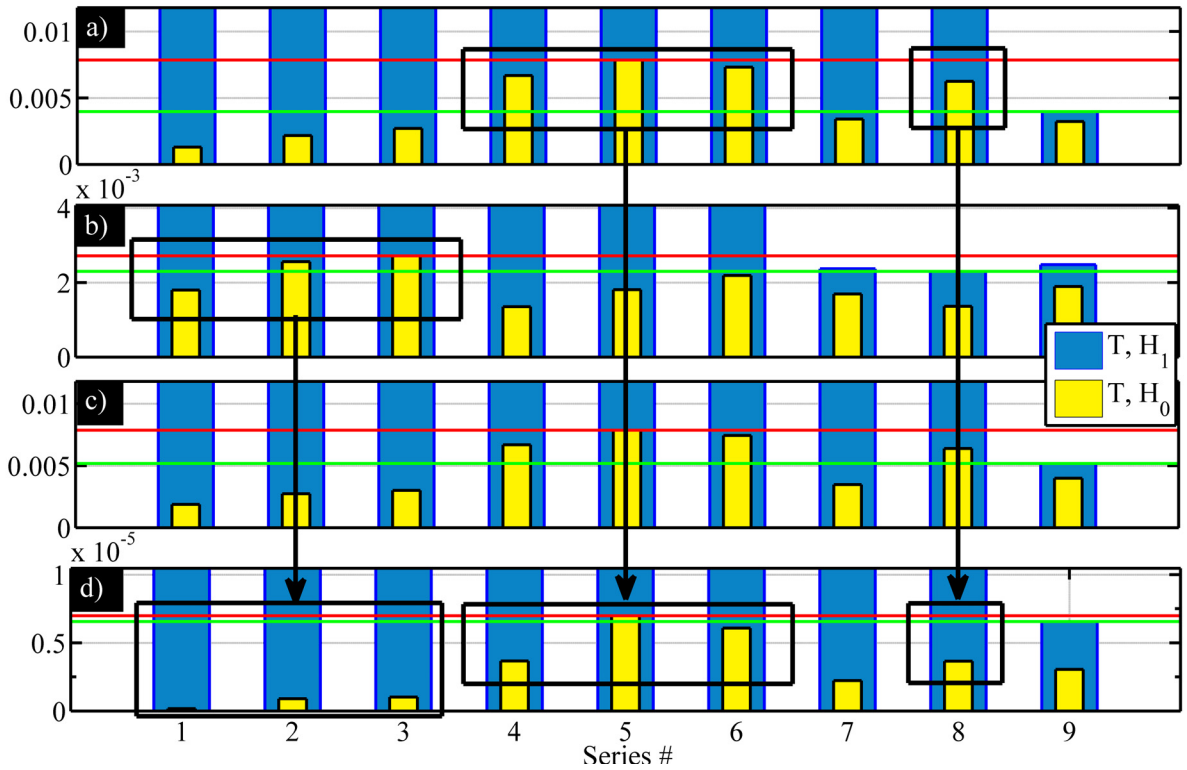

Fig. 4.5 Test statistics maximum values under $\mathcal{H}_1$ and $\mathcal{H}_0$ hypotheses for each series: a)U; b)V; c)Z; d)W. Maximum values of test statistics across the series under $\mathcal{H}_0$ and $\mathcal{H}_1$ hypotheses are shown as the red and green lines, respectively.

remained above the thresholds, it was considered as a false alarm. The tumorous area was defined as follows: the circle of 10 mm radius around the image maximum in case of correct localization; or the same circle around the actual tumor location in case the localization was not correct for a given case. The localization was defined as correct when the image maximum was within the 10 mm radius from the actual tumor location. The total number of misses along all the series for P1 and P2 cases was calculated and inserted into Table 4.3. The total number of false alarms summed up along the series is shown in the corresponding columns. Improvement in detection performance for both W and Z test statistics can be seen. It is important to emphasize that the 5 misses occur for series 8 and 9 when the tumor is located in glandular tissue. In these cases, the dielectric contrast is substantially lower than in the majority of previous simulation studies reported in the literature.

Since the FDR is penalized, the number of false alarms is lower than the number of misses.

However, both the number of misses and the number of false alarms are less for the fusion approach than for any of the component approaches, as follows from Table 4.3. This demonstrates the utility of the proposed approach. If another criterion is used to set the threshold, for example, minimization of the probability of type II error (probability of a miss), better results could be achieved in the number of misses, but the number of false alarms could increase. The investigation of the different thresholding approaches will be considered in future work.

4.5 Chapter summary

This chapter described a dual-modality approach to fuse data from the methods of MWR and MWIT. In the dual-modality hypothesis testing framework, two test statistics were considered, one based on the GLRT and one heuristic. Null-distributions of these statistics were derived to enable the selection of thresholds. The performance of the proposed dual-modality detection method was evaluated using FDTD-simulated signals. The fusion approach can decrease the number of "false alarms" (detection of tumor when it is not present) and "misses" (failure to detect tumor that is present). Although limited in statistical significance, these results indicate that it is potentially beneficial to use the MWR and MWIT modalities jointly, in a manner that allows fusion of their signals.

Chapter 5

Experimental device prototype for microwave breast cancer detection: signal acquisition and pre-processing methods

During the past decade, research in microwave breast cancer detection has advanced to experimental validation. Several experimental systems have been developed by research groups worldwide. The results that have been published so far suggest that the microwave method can be a viable solution for mass-screening. However, the current experimental prototypes require further improvement and testing before their usage in a clinical setting.

Several challenges need to be addressed in order to bring the microwave breast cancer detection technology to the market. Advancement of data acquisition systems plays crucial role in the overall system success. This chapter focuses on challenges and solutions related to the signal-recording system.

First, the design of the experimental device prototype considered by the research group at McGill University is presented. The signals that this device collects are characterized. Next, the factors that can introduce uncertainties into the collected signals are identified and methods to mitigate these factors are discussed. Finally, the chapter describes a method to compensate for the phase uncertainties in the signals, associated with the microwave

sampling mechanism. Phase errors are one of the factors that reduce the resulting image quality. This factor is crucial in "differential" imaging, when previously collected signals are subtracted from the newly acquired signals in the time domain.

5.1 Requirements for the microwave data acquisition system

This research study focuses on a scenario when a patient lies on a bed with a breast placed in a radome, as shown in Fig. 5.1. An array of antennas is integrated into the radome. One antenna emits an electromagnetic pulse and all the other antennas record the signal scatter. This process is repeated for each antenna taking its turn as a transmitter, producing an array of recorded signals. These signals are pre-processed and passed into an imaging algorithm, which constructs an image to highlight possibly present tumors in the breast.

The microwave imaging system consists of the following components:

1. RF pulse generator;
2. Circuits that condition the RF pulse and deliver it to one of the antennas;
3. Switching matrix that selects one of the antennas as a transmitter and one as a receiver;
4. Array of antennas;
5. Recording device for sampling RF signals (oscilloscope);
6. Control system, based on a Micro**c**ontroller Unit (MCU);
7. Personal Computer (PC) that implements high-level data collection functions, signal processing, imaging and visualization.

The recorded signals have the pattern shown in Fig. 5.2.

It is expected that the major component in the recorded signals is the pulse propagating directly from one antenna to another. Another strong contribution to the signal can be the reflection from the skin associated with the dielectric interface between the skin and the matching medium outside of the breast. The power of the skin reflection depends on the

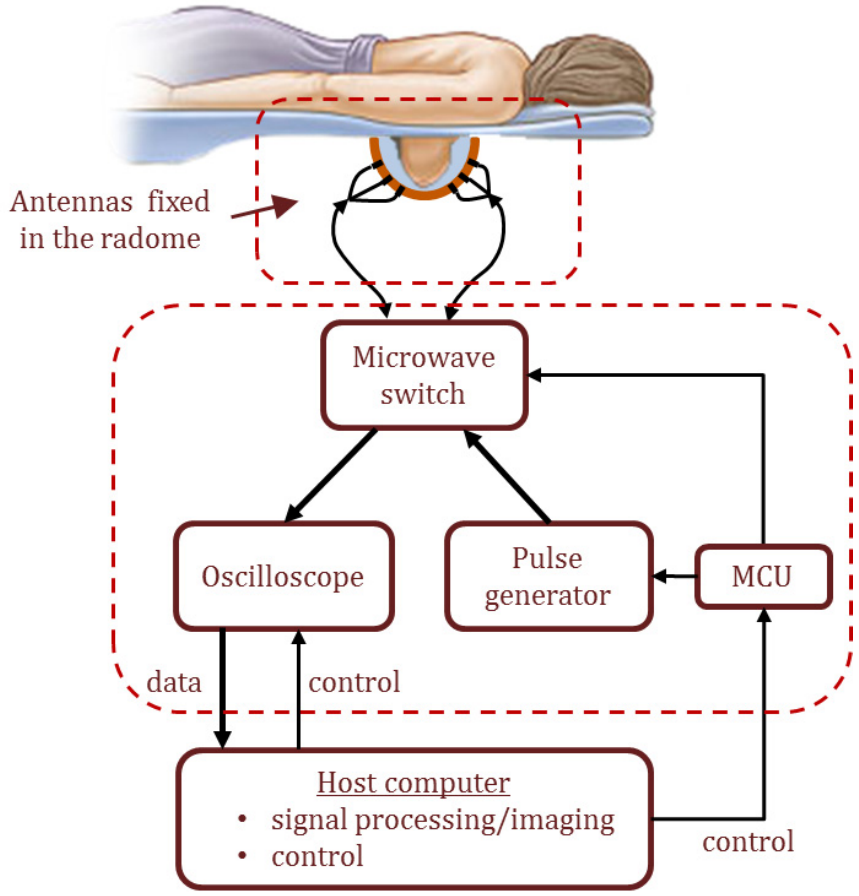

Fig. 5.1 Schematic representation of the designed experimental system (clinical trials).

mismatch in the dielectric properties between the skin/breast and the matching medium. In order to minimize this reflection, the radome is filled with appropriately selected coupling material. The signal of interest (a reflection coming from a possible tumor) is buried in reflections from heterogeneous structures inside the breast ("clutter"). Finally, the recorded waveform has noise associated with the measurement equipment and external interference.

In order to successfully detect tumors present inside the breast, the major requirement is to maximize the Signal-to-Noise Ratio (SNR) of the collected signals. The requirements to the data acquisition system can be summarized in the following list:

- Powerful transmitter. The power of the transmitted signal should be as high as possible, while within the limits of safety regulations [91, 93].

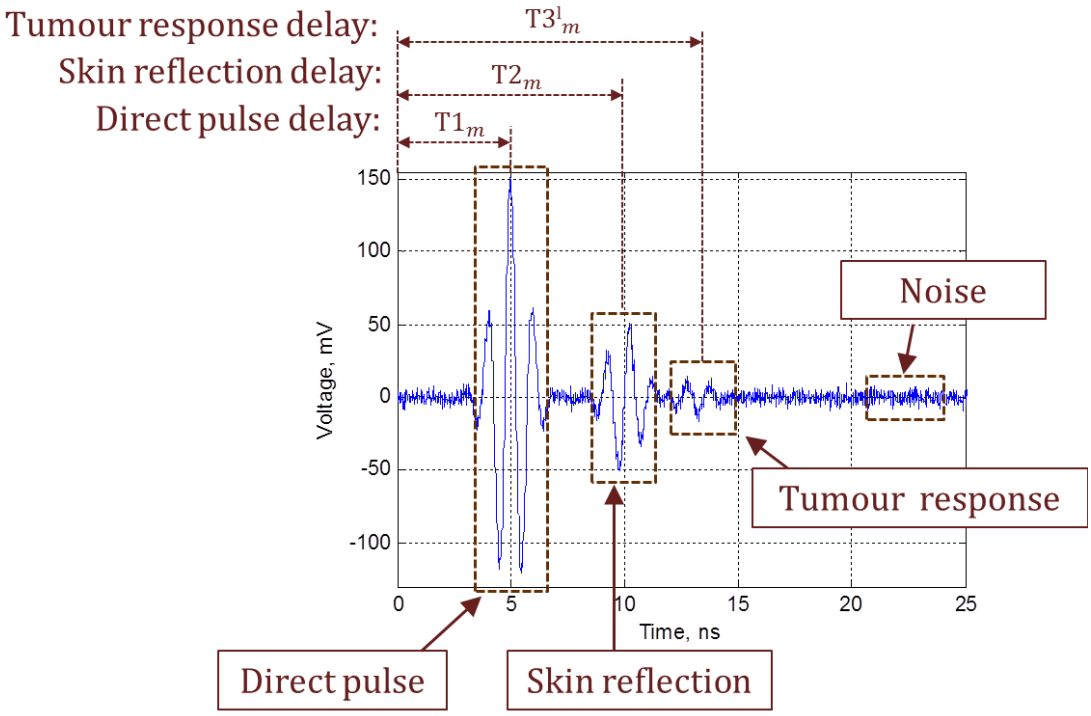

Fig. 5.2 Experimental signal model - components.

- Antennas must be optimized in terms of: a) radiation efficiency in a chosen frequency band; b) physical size; c) beam pattern and d) mutual coupling.
- RF circuits, delivering the pulse between the signal generator/receiver and the antennas need to provide low attenuation and cross-talk.
- The switching matrix should introduce as little cross-talk between the channels as possible, yet providing low insertion loss.
- RF receiver should be sensitive to a very weak tumor response.
- RF sampler needs to provide sufficient bandwidth to capture the required frequency content. The dynamic range of the sampler shall be sufficient to accommodate both strong direct pulses and weak reflections from small tumors.
- Number of sensors should be optimized to meet the trade-off between sufficient gathered information and minimizing the cross-talk and excessive system complexity implied by excessive number of antennas.

- Switching time between the channels must be minimized to reduce the overall data acquisition time.
- All RF circuits and elements need to be well matched between each other to avoid power loss and distortion of the signals.
- All RF elements of the system should be shielded to avoid external interference.

Numerous hardware design techniques can be applied to increase the SNR of the measurement equipment. However, some effects that introduce artifacts can be mitigated in software, as it is demonstrated further in this chapter.

5.2 Experimental device prototype

Fig. 5.3 represents the block-diagram of the implemented data acquisition system.

A generic RF pulse, approximately Gaussian in shape, is generated by an RF pulse generator Picosecond Model 3600 [192]. The generated signal passes through a Synthesized Broadband Reflector (SBR) circuit that shapes the pulse to localize its energy in the range of 2-4 GHz [99]. Next, the pulse is amplified by 35dB with a microwave amplifier Mini-Circuits ZVE-3W-83+ [193].

The amplified pulse is passed through a custom-built 2×16 blocking switching matrix and fed into one of the 16 TWTL antennas [3]. The block-diagram of the switching matrix is shown in Fig. 5.4. The antennas are inserted into the slots of the radome made of Al_2O_3 [194]. The signal is transmitted through the breast and surrounding materials in the radome and a portion of it is received by other antennas. The signal from a receiving antenna is passed back through the receive path of the switching matrix and recorded by PicoScope PS9201A. The oscilloscope implements a sequential equivalent-time sampler with 16-bit resolution and equivalent sampling rates of 80 Gs/s and higher. The analogue bandwidth of the oscilloscope is limited to 12 GHz [195]. The system is triggered by a 1 MHz square-wave from a clock generator Tektronix GigaBERT 1400 [196]. For the purpose of compensating the time-domain phase uncertainties in the sampled RF signals, the clock signal is recorded at the second channel of the oscilloscope (see further in this chapter).

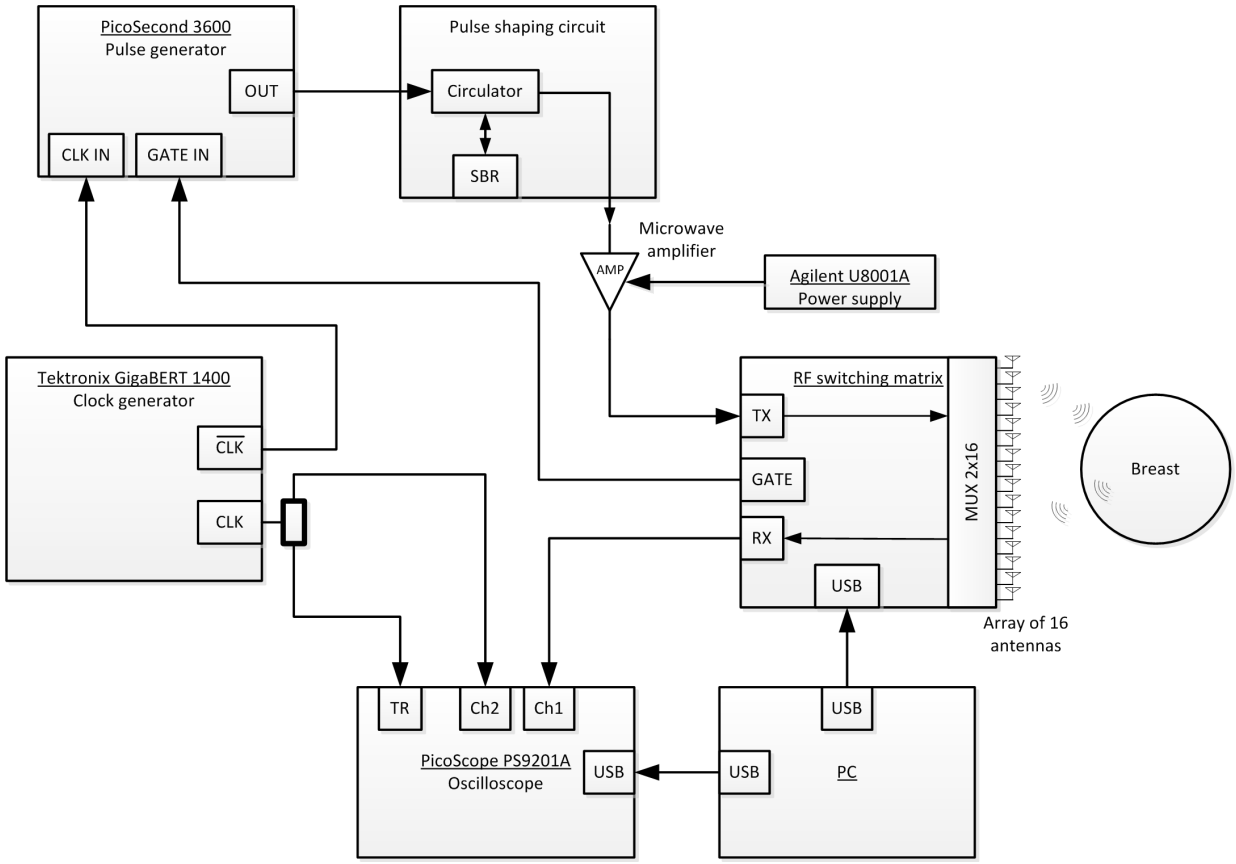

Fig. 5.3 Measurement system block diagram.

The pulse generator, the switching matrix and the oscilloscope are controlled by a data acquisition software running on a PC. The interface between the PC and the external components is implemented with a microcontroller ST Microelectronics STM32F4 [197]. Imaging algorithms are implemented in Matlab and applied to the recorded signals separately from the recording software. Fig. 5.5 depicts the assembled data acquisition system as connected for testing.

5.2.1 Analysis of experimental signals and factors of uncertainty

Signals, acquired by the microwave sampler, possess undesired contributions, which are referred to as artifacts and noise. Prior to applying imaging algorithms to the recorded signals, these signal components should be removed or minimized. These undesired

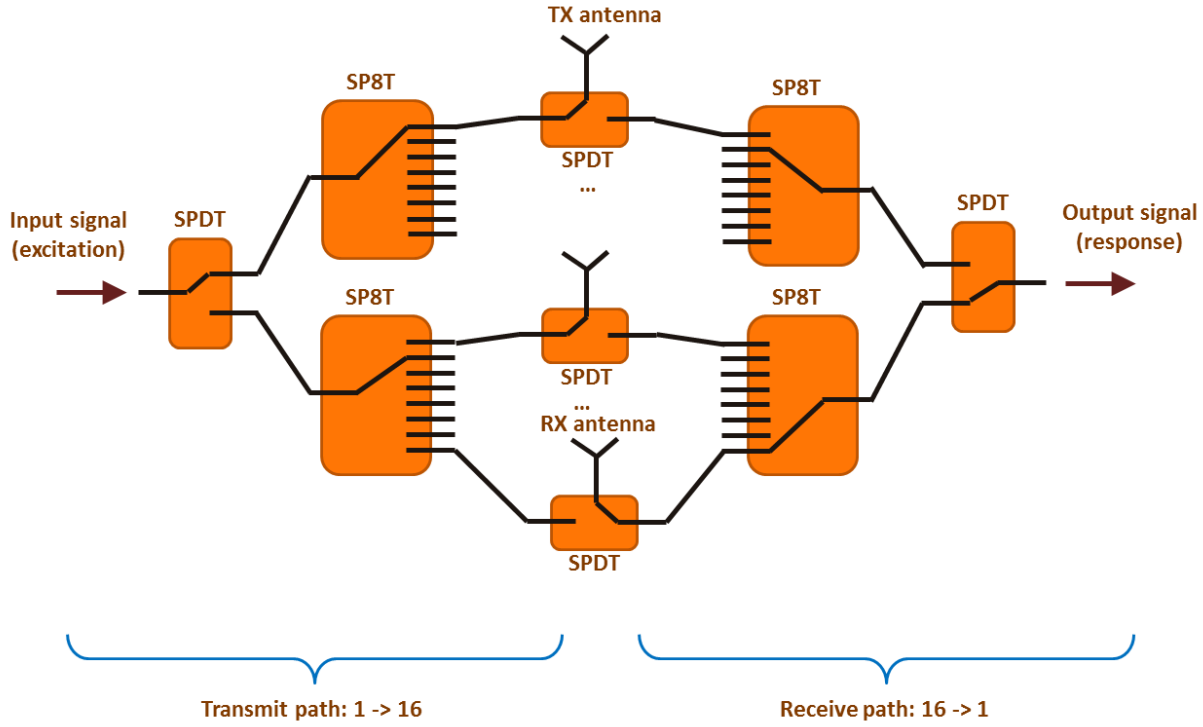

Fig. 5.4 Switching matrix block diagram.

contributions are determined by the factors identified in [198] and are summarized below.

Noise and artifacts related to measurement equipment

When the signal passes through the measurement equipment, it can suffer from several types of additive (vertical) noise/interference, which include: all the noise accumulated at the RF paths, multiple reflections from such components as circulators and power splitters, as well as ADC sampling noise. Vertical noise can be mitigated by using appropriate components and cables, as well as band-pass or low-pass filtering.

Horizontal noise (phase uncertainties) introduces random variable component in the beginning of waveform sampling time. This uncertainty might dramatically decrease the quality of the microwave images. A method to compensate for the horizontal noise is presented further in this chapter.

The described imaging system involves multiple signal paths (switching matrix and

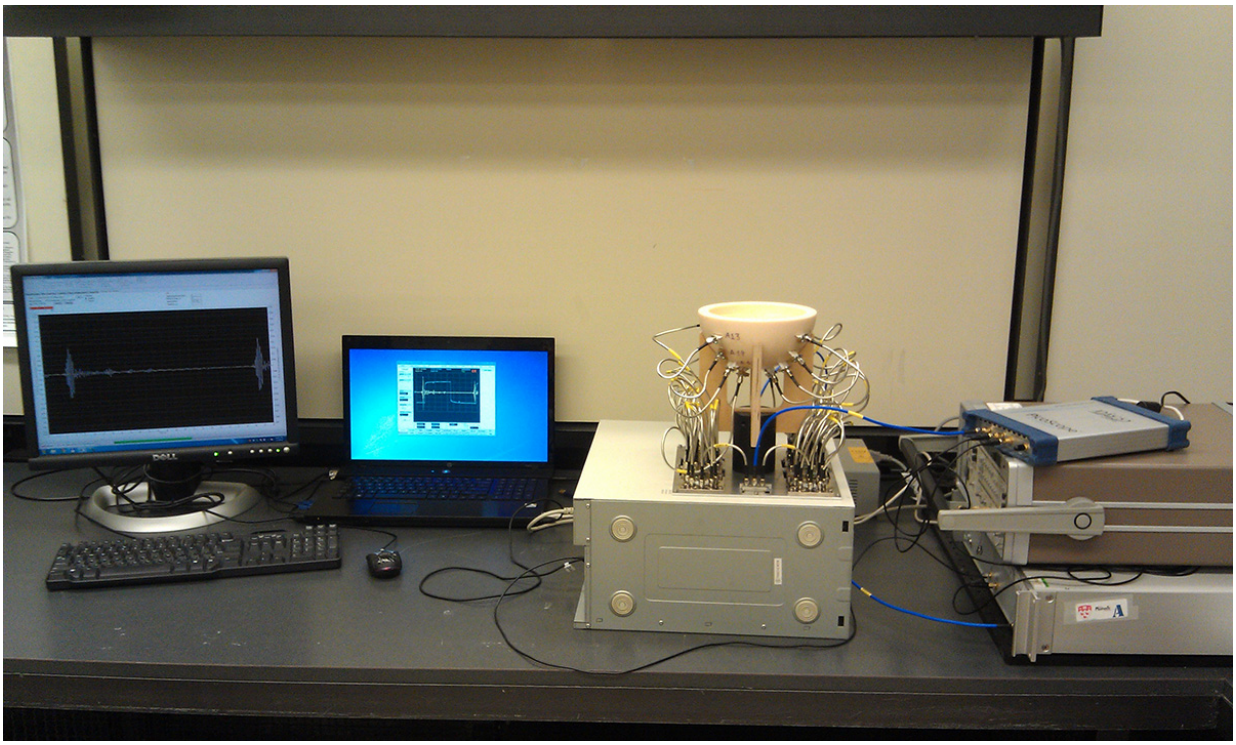

Fig. 5.5 Implemented data acquisition system (patient table not shown).

antennas), which is another source of variability. Both antennas and the RF cables/switches are made with limited precision. One of the methods to compensate for this source of variability is to measure the paths with high-precision measurement instruments and to apply corresponding compensation in software.

Artifacts related to EM signal propagation

There are several contributions to the recorded signals from the physical environment. As it has been mentioned above, pulses from transmitting antennas propagate to the receiving antennas directly. These "direct" pulses are removed by using differential imaging approach: previously recorded signals are subtracted from the newly acquired data. The direct pulses are not related to the tumor response, so they can be subtracted directly in time domain, assuming no phase uncertainty between the corresponding subtracted signals. This subtraction procedure is referred to as "calibration".

Reflections from the skin can be subtracted either during the calibration procedure and/or

by applying techniques described in section 3.2.

Figure 5.6 shows a model of a signal after pre-processing.

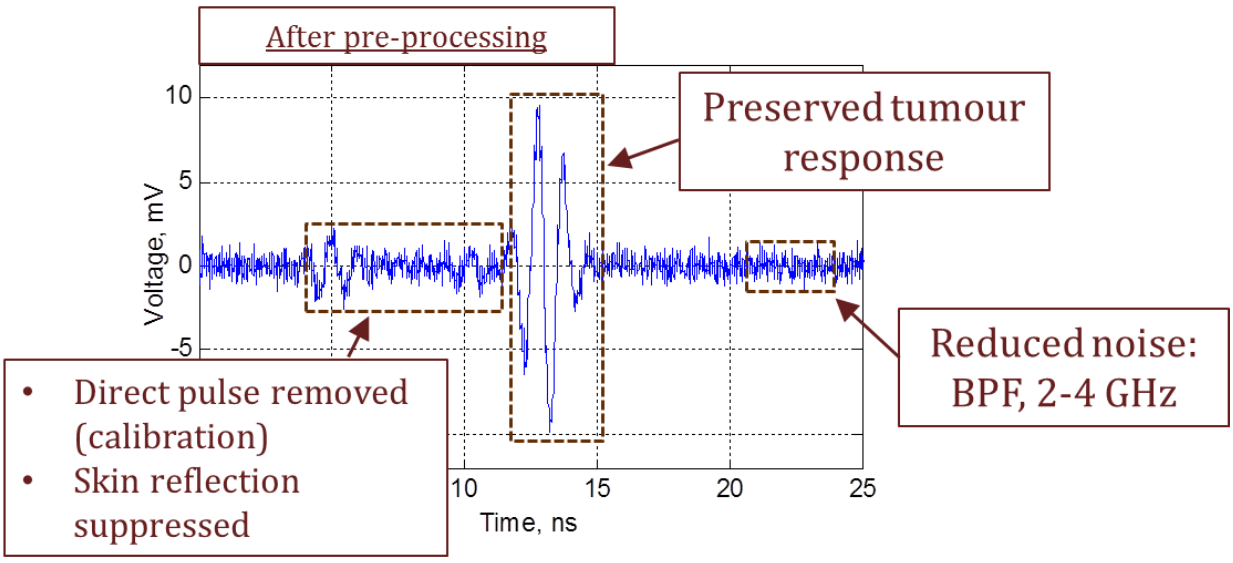

Fig. 5.6 Recorded signal after pre-processing.

5.3 Compensation for phase errors in a microwave sampler

As mentioned earlier, the experimental system employs a sequential equivalent-time sampling oscilloscope to record microwave signals in time domain. Experimental studies described further show that the recorded signals often suffer from a significant phase jitter and drift with respect to the trigger signal. This uncertainty in phase, not being an issue for other applications, can result in a significant problem for the differential imaging approach.

In the differential imaging signals, recorded at different times from the same patient at different times, are subtracted from each other. The differential signals are then used to identify the differences in the scattered EM field and to detect possible tumor reflections. Slight shifts in time domain between the two pulses that are subtracted leaves a residual pulse, that might hinder a weak tumor response. Thus, compensation for the trigger phase errors is essential.

This section presents an approach to reduce the residual pulse with the help of a "reference" signal, recorded at the second channel of the oscilloscope. The "reference" signal is used to detect phase shifts between the recordings. The values of these phase shifts are then used to adjust the phase of the corresponding microwave signals, recorded at the first channel of the oscilloscope. The clock signal that triggers the data acquisition system is used as the reference signal.

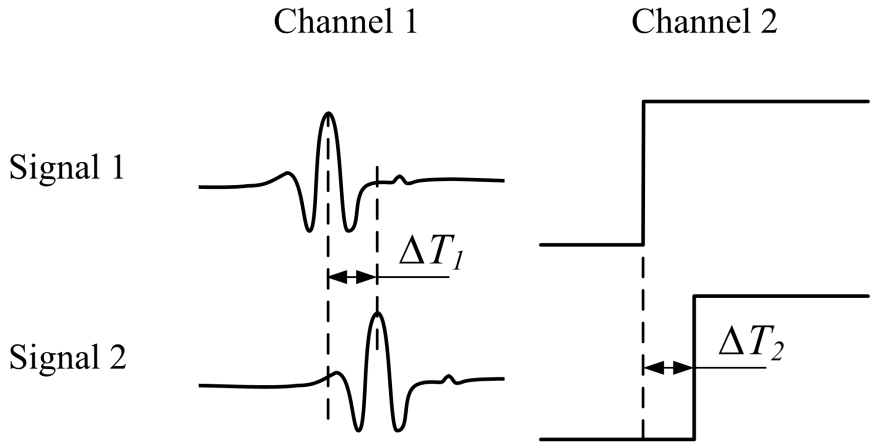

Fig. 5.7 Time alignment based on reference signals.

Figure 5.7 demonstrates the idea of the described time alignment. It represents two sets of recorded signals, each having a microwave pulse (channel 1) and a reference signal (channel 2). The phase differences between the signals are denoted as ΔT_1 and ΔT_2 for channel 1 and channel 2, respectively. Since signals in channel 1 change depending on the imaging scenario (e.g. varying antenna pairs), but reference signals on channel 2 have fixed shape, ΔT_2 between all the recordings can be estimated. Next, assuming $\Delta T_1 = \Delta T_2$, compensation for the phase difference in channel 1 can be performed using estimated ΔT_2. The assumption of $\Delta T_1 = \Delta T_2$ does not hold in reality. However, as will be shown further, there is a significant correlation between ΔT_1 and ΔT_2, which enables compensating the phase delay partially. This compensation statistically improves the overall signal alignment.

The rest of this section is organized as follows. First, problem statement is presented in section 5.3.1. Next, the methodology to estimate the phase delay between reference signals, as well as the technique to efficiently align microwave signals are described (section 5.3.2). Finally, the results of the experiments and the discussion are presented in section 5.3.3).

5.3.1 Problem statement

Figure 5.8 displays typical signals, recorded with the data acquisition system, described in section 5.2. The two signals are recorded from the same antenna pair one day after another. The green signal represents a signal without a tumor response and the blue signal has a weak reflection from a tumor phantom, inserted into the breast phantom.

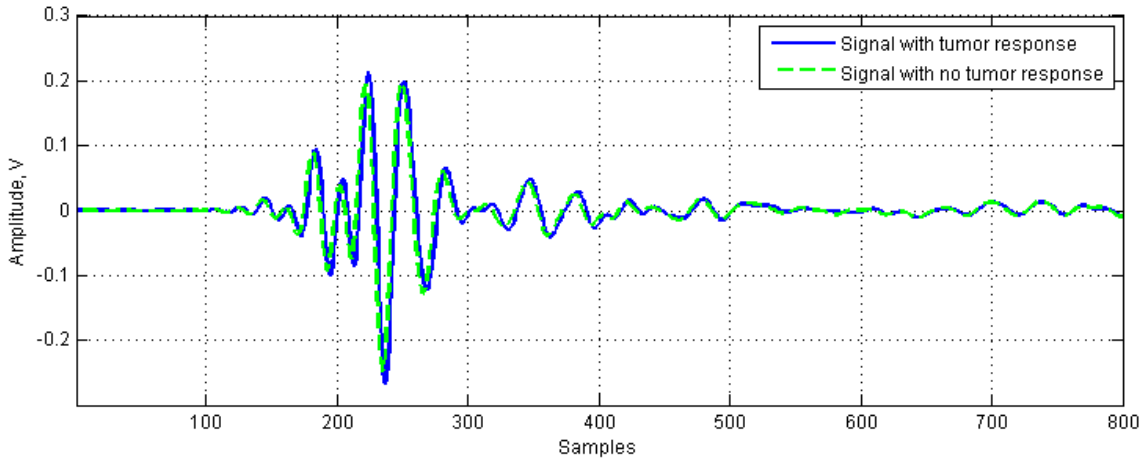

Fig. 5.8 Recorded signals (after band-pass filtering): green - signal without tumor response (baseline); blue - signal with tumor response

It can be seen that the signals are almost identical in shape due to the dominant direct pulse, propagating from one antenna to another. The graph also shows that the two signals have a visible phase shift with respect to each other.

In order to remove the direct pulse, a calibration procedure is applied, which subtracts the baseline signal from the signal with the tumor response. The result of the subtraction is represented in Fig. 5.9a.

Since the recorded signals (Fig. 5.8) have a phase offset, their subtraction produces the residual pulse seen at the same location in time as the maximum of the recorded signals (sample range 240 - 250). However, if the baseline is delayed by 2.2 samples prior to calibration, the residual pulse is significantly reduced (Fig. 5.9b). It can be seen that now the maximum of the difference signal has shifted closer to sample range 330 - 340. This is expected, since the tumor response is delayed by several nano-seconds with respect to the direct pulse. In this case, the delay is approximately 1.25 ns (100 samples at sampling

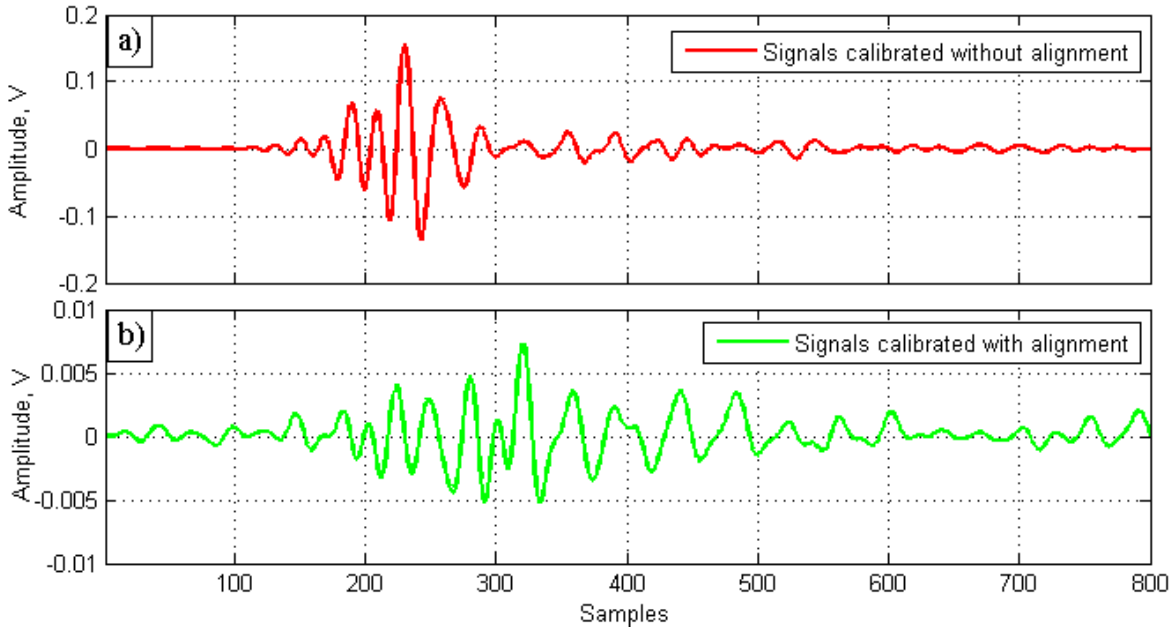

Fig. 5.9 Signals after calibration: a) without alignment; b) with alignment.

period $T_s = 12.5$ ps). This example demonstrates that the calibration procedure, without properly aligned signals, results in the differential signals with the presence of a dominant residual pulse. This pulse is on the order of magnitude higher in amplitude than the tumor response and prohibits successful imaging.

Another concern associated with the phase delays in the recorded signals is that the calibrated difference signals might be still offset across the channels of the imaging system[1]. This can happen if the method to align the recorded signals for calibration is applied only between the pairs "baseline - signal with tumor response". If the offset is still present between the channels, it can result in increased blur of the images, produced by the imaging algorithms.

Thus, the goal of this study is to develop a method to phase-align the recorded signals both between the recorded sets of signals (i.e. between baselines and the signals with the tumor response) and within the recorded sets of signals (i.e. between the channels).

The pairwise phase-alignment of the signals between the sets can be done by applying a cross-correlation method between the baseline and the signals with the tumor response.

[1] A channel of the imaging system is defined by a pair of transmitting and receiving antennas

Since the dominant direct pulse has the same shape in both of the signals, the detection of their phase offset should not be an issue. The method with the cross-correlation, however, does not apply to align the signals within the sets since the direct pulses are different from channel to channel.

In order to overcome this, "reference" signals are recorded at the second channel of the oscilloscope. They will be used to detect the phase difference, as previously mentioned in section 5.3.

The phase delays ΔT_1 and ΔT_2 of the signals, recorded at the two channels of the oscilloscope, may vary. However, since the internal oscilloscope paths of the signals fed to channels 1 and 2 are usually implemented in a similar way (in contrast to the signal path of the trigger), a hypothesis is considered that the variability of the phase between the channels is lower than that between the channels and the trigger event. In other words, the author conjectures that the correlation between ΔT_1 and ΔT_2 is high. If this hypothesis is true, then the discussed alignment method shall help reduce the residual pulse in the difference signals.

In order to develop an efficient signal alignment method for microwave imaging, several steps are considered. First, the above-noted hypothesis should be tested. This task requires an accurate method to estimate phase delays between the reference signals, which will be developed further in this section. Next goal is to make use of the estimated phase delays between the recordings in order to align RF signals and demonstrate that the residual pulse after the calibration is reduced.

5.3.2 Methodology

In order to verify the hypothesis mentioned above, the test setup, depicted in Fig. 5.10, is considered.

A 1 MHz clock signal from the clock generator is routed to both channels of the oscilloscope. Inverted clock signal from the same generator is used as the trigger source. Short cable "3" is used for the trigger input to start recording earlier than the same clock edge enters the RF channels of the oscilloscope. Long cable "1" together with the short cables "2" delay signals to channels 1 and 2 by approximately 40 ns. This delay is necessary to record the same edge of the clock signal that is used to trigger the acquisition (cable "3" introduces

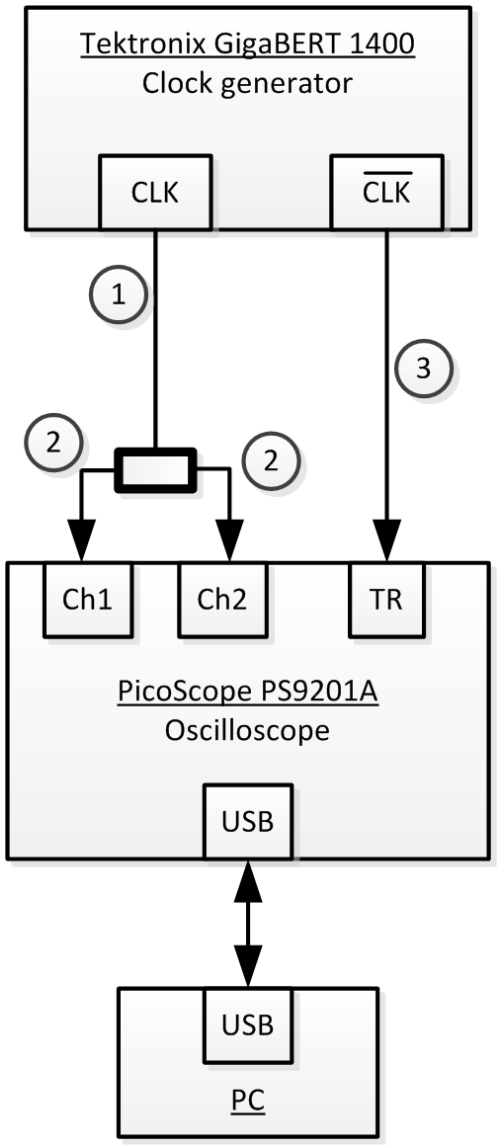

Fig. 5.10 Trigger analysis setup.

the delay of approximately 1 ns). It is essential to record the same edge of the clock since it practically eliminates the jitter of the clock signal, associated with the clock generator (which can be up to 100 ps, according to the specifications [196]).

The timing diagram represented in Fig. 5.11 explains the delays of the system. It is shown that the inverted clock signal arrives at the trigger input of the oscilloscope after delay $\Delta T_T \approx 1$ ns. After another delay $\Delta T_S \approx 37$ ns [195], sampling of the channels begins.

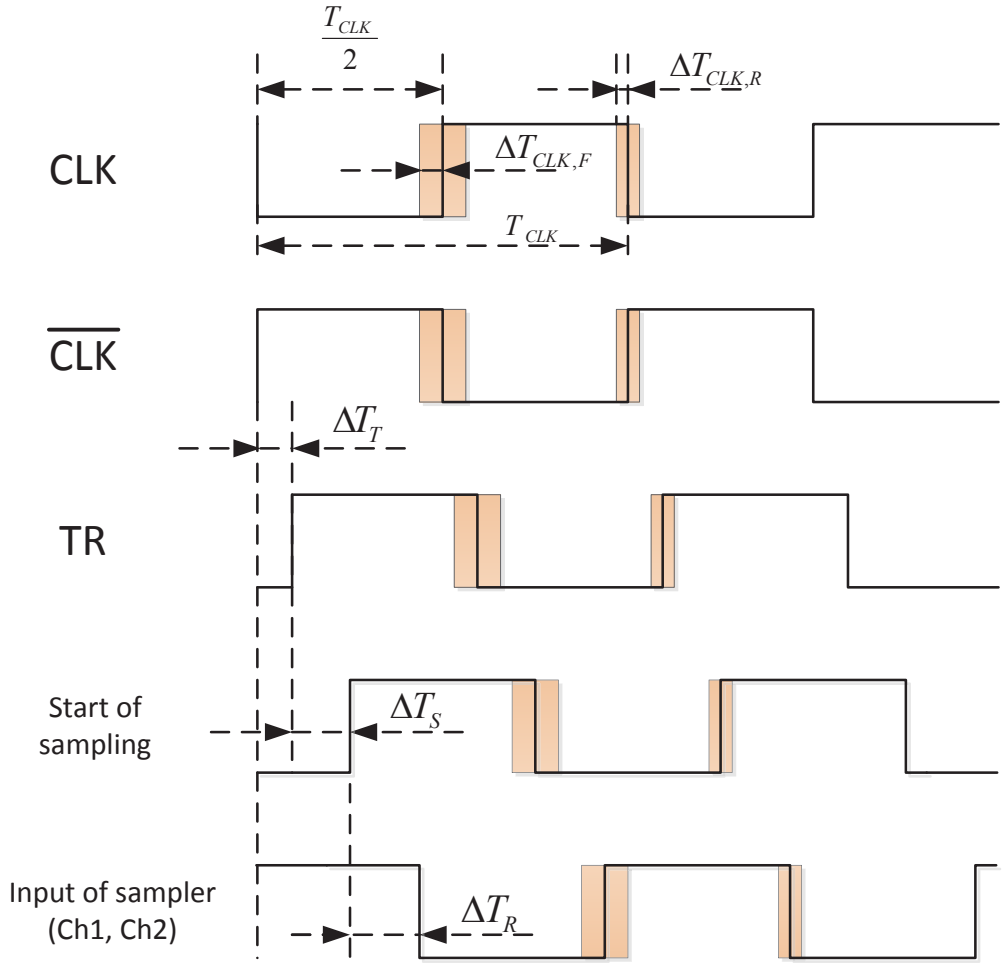

Fig. 5.11 Trigger analysis - delays.

Since the clock signals fed to the channels 1 and 2 are delayed by approximately 40 ns, their delay relative to the start of the recorded waveform is $\Delta T_R \approx 3$ ns.

Delays ΔT_T and ΔT_S are not relevant for the analysis of the phase delay. The delay ΔT_R will be analyzed separately for each of the channels. Thus, the timing diagram represented in Fig. 5.12 is considered.

Random variables $T_1 = t_1 + \Delta t_1$, $T_2 = t_2 + \Delta t_2$ and $T_{12} = t_{12} + \Delta t_{12}$ are introduced, where t_1, t_2, t_{12} are deterministic components and $\Delta t_1, \Delta t_2, \Delta t_{12}$ are random variables. As

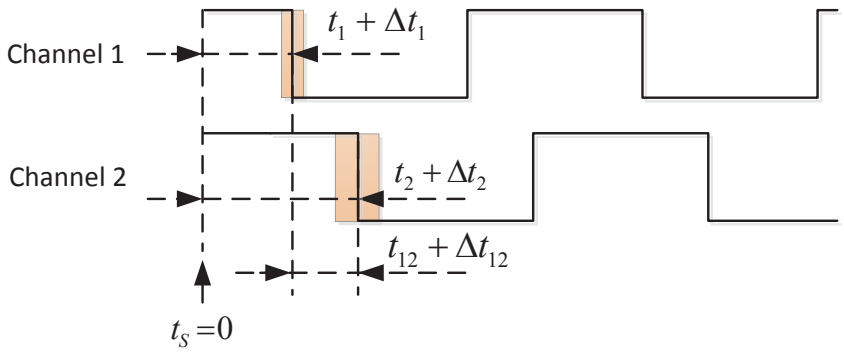

Fig. 5.12 Trigger analysis - delays between the channels (not scaled).

mentioned previously, the considered hypothesis is that $std(\Delta t_{12}) < std(\Delta t_1)$ and $std(\Delta t_{12}) < std(\Delta t_2)$, where $std(\cdot)$ denotes standard deviation of a random variable.

For convenience purposes, phase delays T_1 and T_2 are not estimated. Instead of estimating the delay of the signals with respect to $t_s = 0$, equivalent random variables ΔT_1, ΔT_2 and ΔT_{12} are estimated (Fig. 5.13). First two variables are found as mutual phase delays between the base reference (signal #1, channel 1 for each dataset) and all other signals. Variable ΔT_{12} is computed as a mutual delay between the two channels of the same recording.

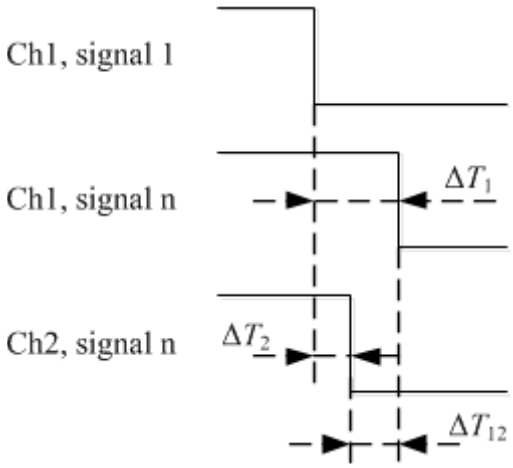

Fig. 5.13 Representation of estimated phase delay variables.

Estimation of the phase delay

In order to demonstrate that the hypothesis is true, the phase delays between the signals need to be estimated. Estimation of these values is not trivial due to the noise in the recorded data. This work considers three methods to estimate mutual phase difference between the signals. Each of these methods has variations, depending on the steps and settings applied, as described further. These methods are further compared to choose one that provides the best performance for the application of the phase uncertainty compensation.

Phase delay estimation in time domain

The time-domain phase difference estimation algorithm is shown in Fig. 5.14. In order to reduce high-frequency noise, the signals are first low-pass filtered. Then, the resulting signals are optionally differentiated to highlight the areas with the slope. Next, the region with the slope is extracted and interpolated by a factor of 100. Finally, mutual cross-correlation between the two signals is computed for multiple lags. Phase shift ΔT is then taken as the lag that maximizes the cross-correlation.

Phase delay estimation in frequency domain

One of the benefits of the frequency-domain processing is the possibility to operate with fractional values of delays directly, without interpolation. This potentially increases the accuracy of phase estimation and reduces the complexity of the algorithms.

The first steps are the same as those applied in the time domain: the signals are low-pass filtered and differentiated. Next, additional optional step is considered for the frequency-domain algorithm: windowing. As shown later, windowing helps avoid artifacts associated with the periodical assumption of input signals, when the Digital Fourier Transform is applied. Next, the signals are transformed to the frequency domain by using the FFT. The resulting spectra is denoted as $Y_1(\omega)$ and $Y_2(\omega)$.

In order to estimate the phase delay based on the spectra of the two signals, the propagation of signal $Y_1(\omega)$ through a linear system $H(\omega)$ is modeled, such that:

$$Y_2(\omega) = H(\omega)Y_1(\omega) \quad , \tag{5.1}$$

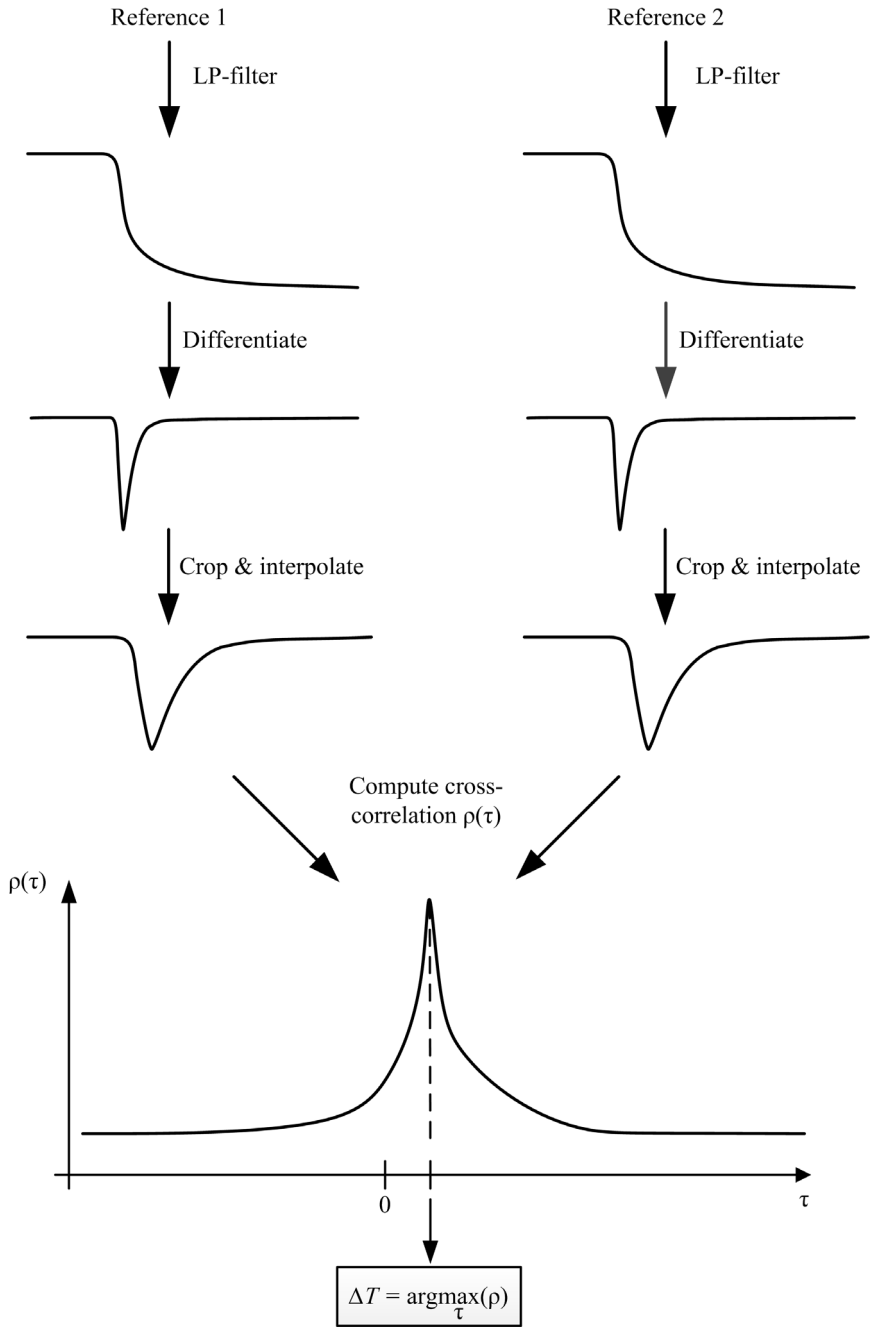

Fig. 5.14 Estimation of phase delay in the time domain with cross-correlation.

Where system $H(\omega)$ is modeled to introduce delay and attenuation as follows:

$$H(\omega) = e^{-j\omega\tau(\omega)} \quad . \tag{5.2}$$

Thus, signal $Y_2(\omega)$ is represented as a delayed and attenuated version of $Y_1(\omega)$:

$$Y_2(\omega) = Y_1(\omega)e^{-j\omega\tau(\omega)} \quad . \tag{5.3}$$

The frequency-domain phase estimation method considers two approaches to compute the value of the delay between the two signals ΔT.

The first approach (Fig. 5.15) is based on weighted averaging of the values of $\tau(\omega)$ across the region of interest of ω. Thus, this approach is referred to as "weighted tau". First,

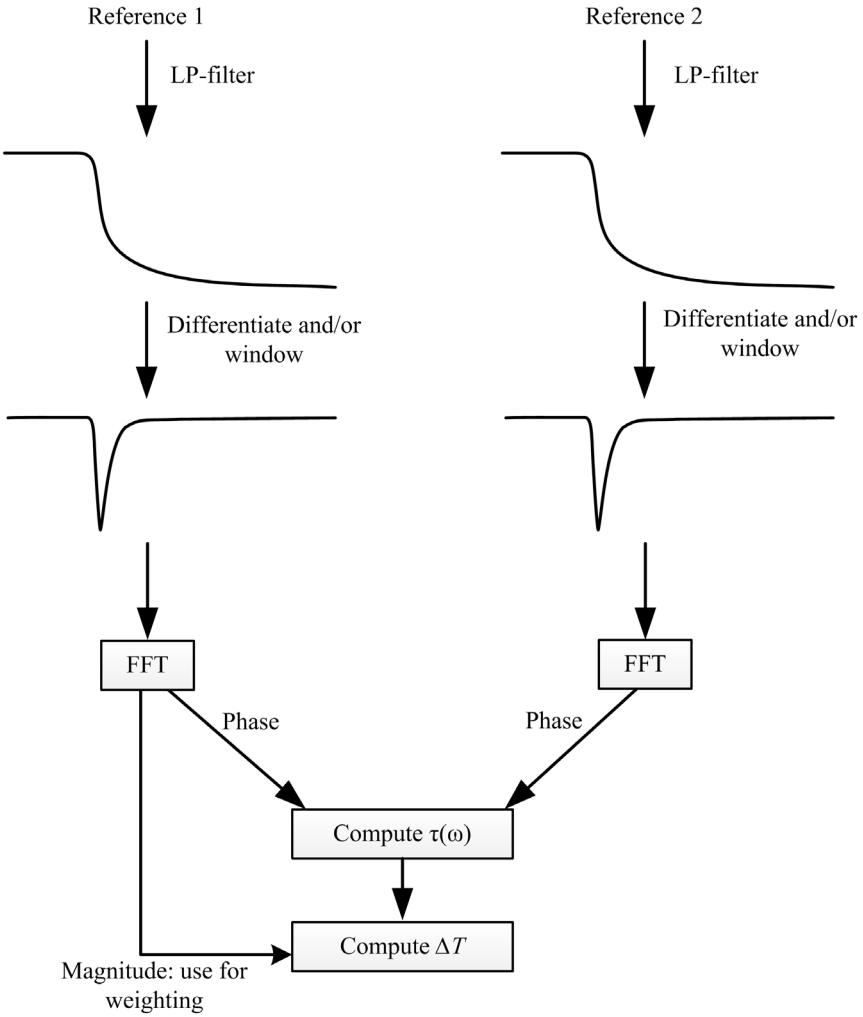

Fig. 5.15 Estimation of phase delay in frequency domain: direct phase computation.

$\tau(\omega)$ is computed as follows:

$$\tau(\omega) = Re\left\{-\frac{1}{j\omega}\ln\left(\frac{Y_1(\omega)}{Y_2(\omega)}\right)\right\} \quad . \tag{5.4}$$

In the above expression, only real part is taken since the imaginary part of the expression is associated with the attenuation, which is not beneficial for the phase estimation.

Next, ΔT is calculated as follows:

$$\Delta T = \sum_{i=1}^{N} \tau(\omega_i) w_i \quad , \tag{5.5}$$

Where $N = N_{FFT}/2$ is the number of frequencies of the spectrum, excluding the DC component and frequencies higher than Nyquist frequency. Weights are represented by w_i, such that $\sum_{i=1}^{N_f} w_i = 1$ and where $N_f \leq N$ denotes the number of frequencies under analysis. Three following three options of weighting are investigated:

a) *Weighting using all frequencies.* Normalized magnitude of one of the signal spectra is used as a weighting function[2]:

$$w_i = \frac{|Y_1(\omega_i)|}{\sum_{j=1}^{N_f} |Y_1(\omega_j)|} \quad . \tag{5.6}$$

In the equation above $N_f = N$.

b) *Top 5% of most powerful frequencies* are taken to form the weighting function. In this case, the same equation (5.6) applies, but N_f is limited to 5% of the total number of

[2]Since the two signals are expected to have very close shape, their magnitude spectrum will be similar. Thus, there is no significant difference which of the signals is taken for the weighting function.

frequencies in the spectrum. All other weights are equal to zero:

$$w_i = \begin{cases} \dfrac{|Y_1(\omega_i)|}{\sum_{j=1}^{N_f} |Y_1(\omega_j)|}, & \forall\ i : |Y_1(\omega_i)| \geq \mathcal{C}(0.05N) \quad , \\ 0, & \text{otherwise} \quad , \end{cases} \tag{5.7}$$

Where $\mathcal{C}$ represents the array of values from $|Y_1(\omega)|$, sorted in descending order.

c) *Single-frequency option.* Most dominant frequency of the spectrum is used to determine ΔT. The weights are determined as follows:

$$w_i = \begin{cases} 1, & \text{if } i = \underset{i}{\text{argmax}}\, |Y_1(\omega_i)| \quad , \\ 0, & \text{otherwise} \quad . \end{cases} \tag{5.8}$$

An alternative approach to compute ΔT is based on the minimization of Mean Squared Error (MSE) (Fig. 5.16). This approach assumes that the value of τ is constant across all the frequencies. The optimum value of τ to fit the model (5.3) based on weighted MSE is then taken as the phase delay between the two signals:

$$\Delta T = \underset{\tau}{\text{argmin}} \sum_{i=1}^{N_f} |Y_2(\omega_i) - Y_1(\omega_i) e^{-j\omega_i \tau}|^2 w_i \quad . \tag{5.9}$$

The expression can be further transformed as follows:

$$\begin{aligned} \Delta T &= \underset{\tau}{\text{argmin}} \sum_{i=1}^{N_f} w_i \left(|Y_2(\omega_i)|^2 + |Y_1(\omega_i)|^2 - Y_1(\omega_i) Y_2^*(\omega_i) e^{-j\omega_i \tau} - Y_1^*(\omega_i) Y_2(\omega_i) e^{j\omega_i \tau} \right) \\ &= \underset{\tau}{\text{argmax}} \sum_{i=1}^{N_f} w_i \left(Y_1(\omega_i) Y_2^*(\omega_i) e^{-j\omega_i \tau} + Y_1^*(\omega_i) Y_2(\omega_i) e^{j\omega_i \tau} \right) \\ &= \underset{\tau}{\text{argmax}} \sum_{i=1}^{N_f} Re\{ Y_1(\omega_i) Y_2^*(\omega_i) e^{-j\omega_i \tau} \} w_i \quad , \end{aligned} \tag{5.10}$$

Where w_i are real-valued weights, computed using the three methods, per (5.6), (5.7) and (5.8).

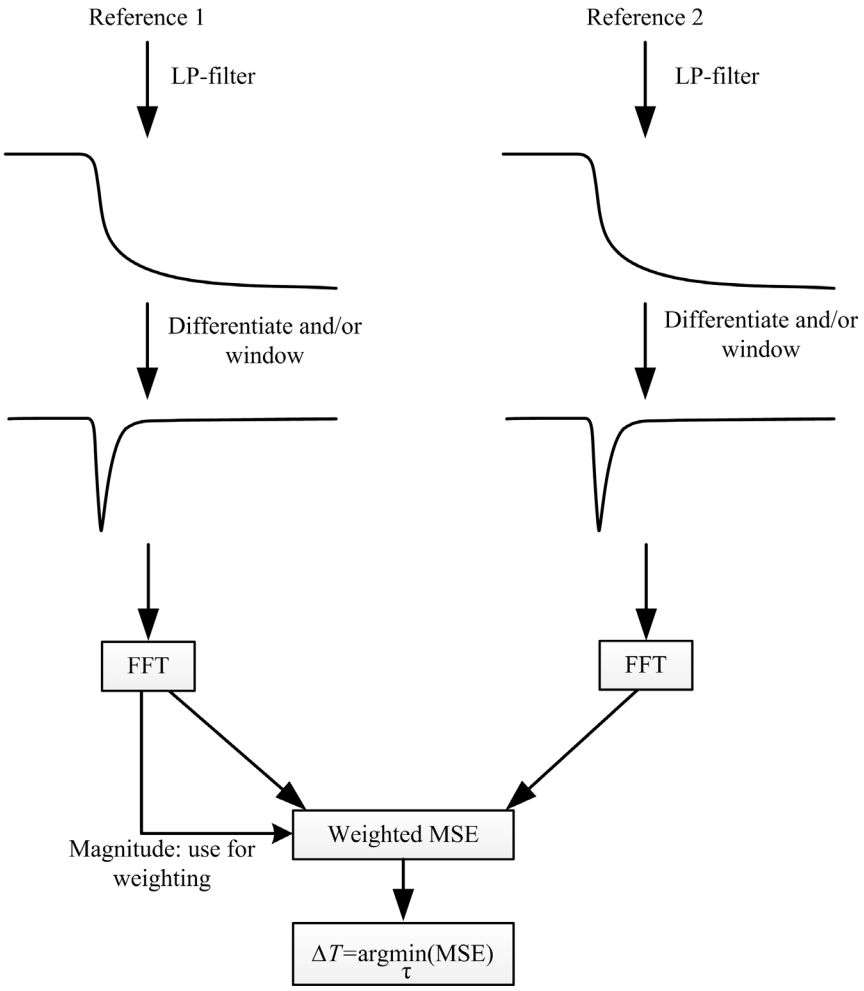

Fig. 5.16 Estimation of phase delay in frequency domain: mean squared error minimization approach.

The optimal value of τ can be found from (5.10) above using already available methods, such as binary search or the Gauss-Newton method.

Time-shifting of microwave signals

Signals recorded from the experimental system (Fig. 5.8) are in the microwave range of several GHz with the dominant pulses positioned closer to the center of the waveforms. Several methods to shift signal with fractional delay are described in the literature [199, 200]. The most popular techniques are based on interpolation. For example, the study in

[200] uses B-spline filtering with interpolation. However, applied to the recorded "step"-like signals with significant noise, methods based on interpolation have proven not to be reliable, since they result in additional numerical artifacts. In order to avoid the artifacts, signal alignment, in the work presented by this thesis, is accomplished in the frequency domain, as shown in Fig. 5.17.

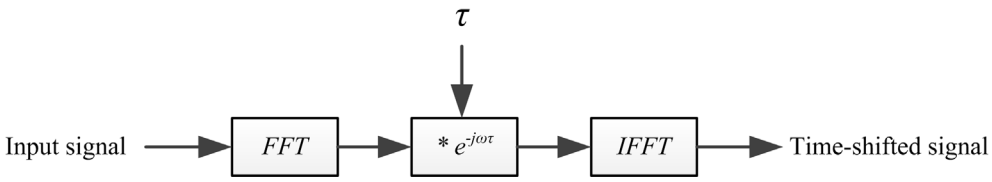

Fig. 5.17 Procedure of time-shifting of microwave signals.

Since the signals are close to zero at the edges, the waveforms are quazi-periodic. This fact allows avoiding using windowing procedure without significant artifacts on signal edges after going through the FFT transformation procedure.

Assessment of signal alignment performance

In order to demonstrate the performance of the developed signal alignment method, a test setup shown in Fig. 5.18 is assembled.

In this experiment, instead of recording clock signal at both channels, the following pairs of signals are recorded: the RF pulse at channel 1 and the clock signal at channel 2. Figure 5.19 depicts two examples of such recordings. It can be seen from the graphs that the signals are not properly aligned. The developed alignment method will be applied to all such recorded pairs. Then, the RF pulses will be subtracted in pairs before and after the alignment. For all the difference signals, their absolute maxima and the overall power will be computed. These two metrics will be used to assess the performance of several variations of the signal alignment method.

5.3.3 Results

This section is structured as follows. First, the results of the phase estimation techniques are presented and one that proves to be the most accurate and reliable is selected for further

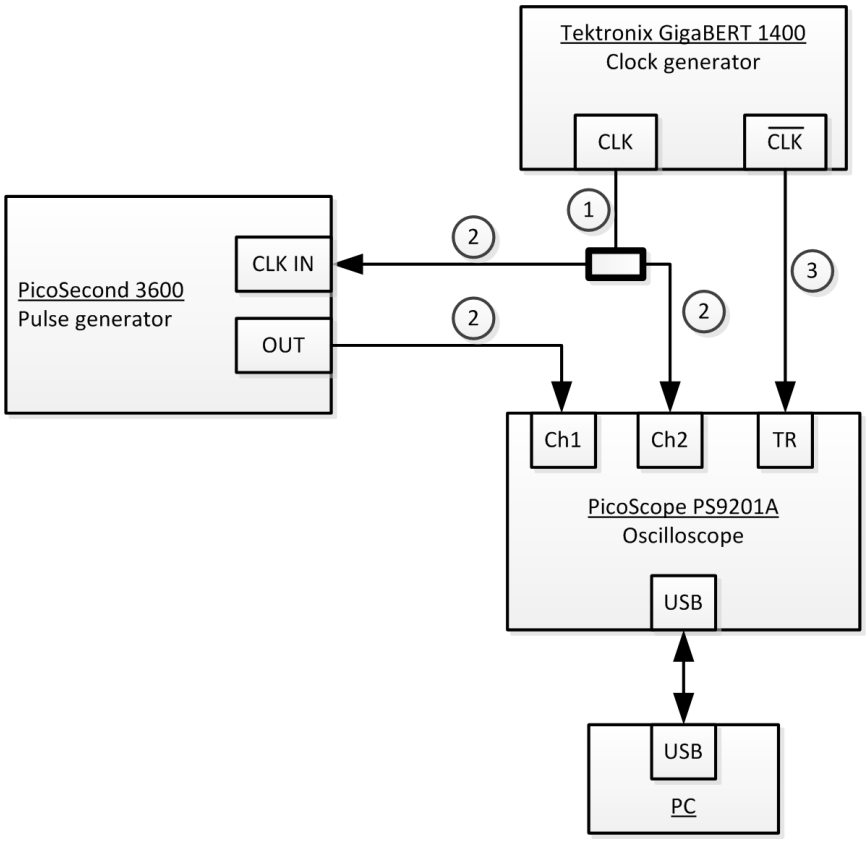

Fig. 5.18 Pulse alignment analysis setup (refer to the beginning of section 5.3.2 for description of components).

use. Next, the section provides the analysis of the phase, associated with the oscilloscope trigger and the two channels. This analysis demonstrates that the hypothesis stated in section 5.3.1 is true. Finally, the results of the assessment of the signal alignment method are discussed.

Estimation of phase delay between reference signals

The phase estimation methods described above are applied to a synthetic negative "step"-like signal, represented in Fig. 5.20. This signal has been generated analytically using the following closed-form expression:

$$e[n] = -0.24 + 0.56e^{-0.19(n-\tau)^{0.47}} \quad . \tag{5.11}$$

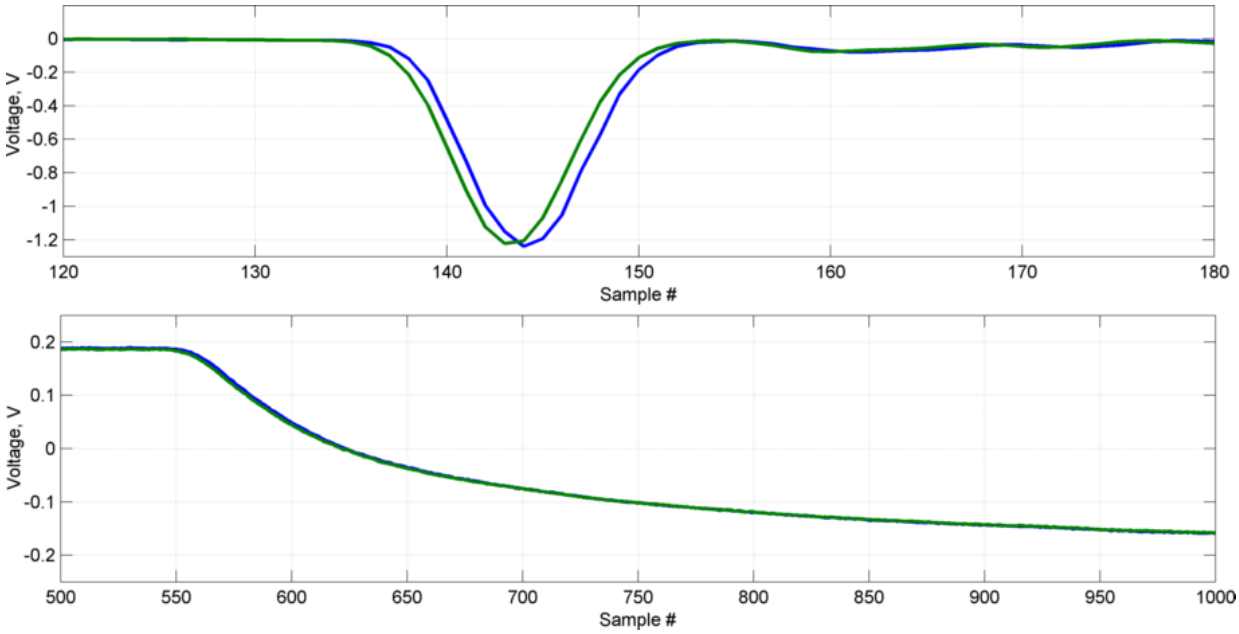

Fig. 5.19 Two pairs of recorded signals (green and blue): microwave pulses in channel 1 (top graph) and reference clock signals in channel 2 (bottom graph).

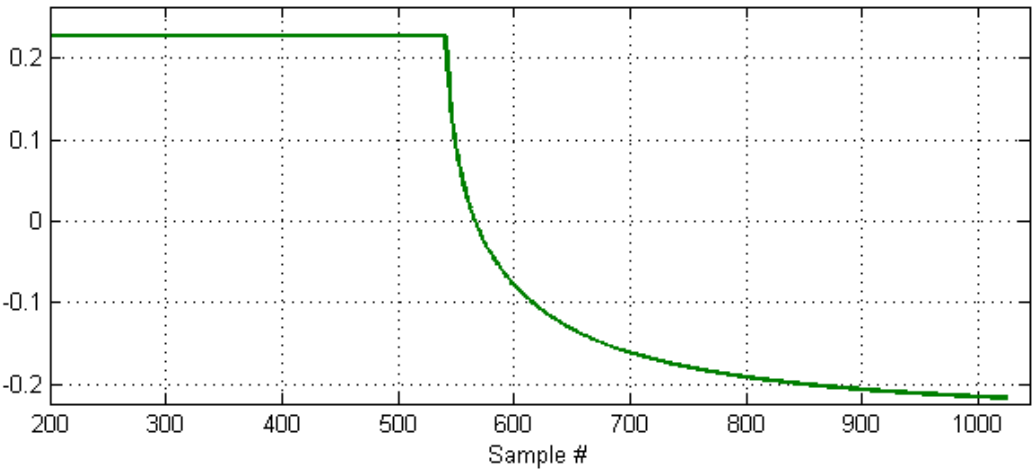

Fig. 5.20 Analytically generated signal used for phase estimation method analysis.

In the expressions above, τ denotes a phase shift in samples. Expression (5.11) has been obtained by fitting the exponential function to the reference signals, collected with the oscilloscope.

1000 pairs of test signals are generated by adding random white noise of -60 dB,-50 dB,-45 dB and -40 dB in power with respect to the signal. The second signal in each pair is analytically delayed by $\tau = 8.59$ samples (the number is chosen arbitrarily) with respect to the first one. The selected noise levels cover the range of noise observed in the experimentally recorded signals at various recording and averaging modes of the oscilloscope. Thus, in total 4 sets of 1000 pairs of signals are considered. In addition, a pair of the above signals without noise is also used in the evaluation.

Multiple combinations of the phase delay estimation methods, described in section 5.3.2, are applied to the signals. The following parameters of the methods are varied:

1. Phase delay estimation methods:
    - Time-domain cross-correlation
    - Frequency-domain "weighted tau" method
    - Frequency-domain MSE method
2. Windowing (only for frequency-domain methods): ON or OFF
3. Differentiation: ON or OFF
4. Weighting type (only for frequency-domain methods, refer to section 5.3.2):
    - "All frequencies" weighting
    - "Top 5%" weighting
    - "Most dominant frequency" weighting
5. Interpolation type (for time-domain methods only, see Fig. 5.14):
    - Linear interpolation
    - Cubic spline interpolation
    - Piecewise cubic Hermite interpolation

Table 5.1 summarizes the results obtained for the time-domain phase estimation method. For each combination of parameters, mean values of the estimated phase delay and standard deviation are presented.

Table 5.1 Time-domain phase estimation results (mean value / standard deviation of estimated phase delay). ND = differentiation is OFF; D = differentiation is ON. "-" denotes failure to correctly estimate the phase delay.

Noise level	Interpolation type					
	Linear		Spline		Hermite	
	ND	D	ND	D	ND	D
No noise	-	8.56/0.00	-	9.00/0.00	-	8.53/0.00
-60dB	-	8.56/0.15	-	8.66/0.48	-	8.54/0.27
-50dB	-	8.54/0.86	-	8.57/0.81	-	8.55/0.82
-45dB	-	7.69/12.10	-	7.96/9.01	-	7.76/12.16
-40dB	-	1.31/31.07	-	2.06/31.05	-	1.61/32.20

The time-domain method, based on maximizing the cross-correlation of two signals with respect to the shift, fails to correctly estimate the phase delay without differentiating the signal. When differentiation is used, linear interpolation provides a better result. However, neither of the variations of the time-domain method is capable of estimating the phase delay at high levels of noise (-45dB and higher) accurately and precisely.

Table 5.2 Frequency-domain phase estimation results: "all frequencies" weighting option (mean value / standard deviation of estimated phase delay). NWND = windowing OFF and differentiation OFF; WND = windowing ON and differentiation OFF; NWD = windowing OFF and differentiation ON; WD = windowing ON and differentiation ON.

Method	Noise level	NWND	WND	NWD	WD
Weighted tau	No noise	1.43/0.00	7.69/0.00	8.53/0.00	8.52/0.00
	-60dB	1.43/0.01	7.69/0.03	8.45/0.08	8.56/0.07
	-50dB	1.43/0.04	7.69/0.01	8.20/0.27	8.55/0.14
	-45dB	1.44/0.07	7.69/0.17	7.93/0.44	8.55/0.23
	-40dB	1.43/0.12	7.69/0.30	7.44/0.71	8.56/0.43
MSE	No noise	2.90/0.00	7.29/0.00	8.57/0.00	8.53/0.00
	-60dB	2.89/0.02	7.29/0.04	8.56/0.05	8.55/0.07
	-50dB	2.89/0.09	7.29/0.11	8.56/0.17	8.55/0.16
	-45dB	2.90/0.14	7.30/0.20	8.57/0.27	8.57/0.27
	-40dB	2.89/0.24	7.28/0.35	8.58/0.55	8.57/0.49

The performance of the frequency domain methods, applied to the realistic "step" signal with the exponential decay transition, is summarized in tables 5.2, 5.3 and 5.4.

Table 5.3 Frequency-domain phase estimation results: "Top 5%" weighting option (mean value / standard deviation of estimated phase delay). NWND = windowing OFF and differentiation OFF; WND = windowing ON and differentiation OFF; NWD = windowing OFF and differentiation ON; WD = windowing ON and differentiation ON.

Method	Noise level	NWND	WND	NWD	WD
Weighted tau	No noise	2.51/0.00	7.68/0.00	8.56/0.00	8.52/0.00
	-60dB	2.50/0.03	7.68/0.03	8.57/0.04	8.55/0.07
	-50dB	2.48/0.06	7.67/0.09	8.57/0.13	8.56/0.14
	-45dB	2.48/0.12	7.68/0.17	8.56/0.23	8.56/0.24
	-40dB	2.48/0.20	7.68/0.31	8.58/0.42	8.56/0.44
MSE	No noise	3.26/0.00	7.29/0.00	8.57/0.00	8.53/0.00
	-60dB	3.26/0.03	7.29/0.04	8.56/0.06	8.55/0.07
	-50dB	3.26/0.08	7.29/0.11	8.56/0.17	8.56/0.16
	-45dB	3.27/0.15	7.30/0.20	8.58/0.30	8.57/0.27
	-40dB	3.25/0.25	7.28/0.35	8.56/0.56	8.57/0.50

Table 5.4 Frequency-domain phase estimation results: "Most dominant frequency" weighting option (mean value / standard deviation of estimated phase delay). NWND = windowing OFF and differentiation OFF; WND = windowing ON and differentiation OFF; NWD = windowing OFF and differentiation ON; WD = windowing ON and differentiation ON.

Method	Noise level	NWND	WND	NWD	WD
Weighted tau	No noise	3.98/0.00	7.62/0.00	8.46/0.00	8.49/0.00
	-60dB	3.98/0.04	7.62/0.05	8.45/0.42	8.54/0.09
	-50dB	3.98/0.12	7.61/0.15	8.45/1.3	8.55/0.15
	-45dB	3.99/0.23	7.61/0.27	8.32/2.5	8.55/0.26
	-40dB	3.97/0.40	7.62/0.49	8.66/4.2	8.58/0.47
MSE	No noise	3.98/0.00	7.62/0.00	8.46/0.00	8.49/0.00
	-60dB	3.98/0.04	7.62/0.05	8.45/0.43	8.53/0.08
	-50dB	3.98/0.13	7.61/0.16	8.33/1.23	8.54/0.17
	-45dB	3.99/0.24	7.61/0.28	7.93/2.05	8.56/0.27
	-40dB	3.98/0.41	7.60/0.49	8.37/1.52	8.56/0.46

Without windowing and differentiation applied, both "weighted tau" and MSE methods fail to correctly estimate the phase delay even for noiseless signals. This failure is related to the fact that the step function is not periodic. Thus, the Fourier transform results in significant artifacts at the edges, which prevent successful phase delay estimation.

Windowing improves the performance, however the estimated phase is still off by around 11% ($(8.59 - 7.62)/8.59 \cdot 100\%$). Differentiation significantly improves accuracy, with the best result achieved using the "top 5%" weighting.

As a conclusion from this experiment, the option with windowing OFF, with differentiation ON and with weighting based on top 5% frequencies provides the combination when most stable performance is achieved with acceptable accuracy. Applied to the exponential decay step signal, "weighted tau" and MSE methods with the combination of the selected options show similar performance. At the same time, "weighted tau" method is simpler in complexity, since it offers a closed-form solution. Thus, this method is chosen for use in the further experiments.

Study of the oscilloscope phase delays

As described in section 5.3.2, pairs of signals with the test setup represented in Fig. 5.10 are recorded. In order to estimate delays ΔT_1, ΔT_2, ΔT_{12} (Fig. 5.13), two sets of 1000 pairs of the signals are recorded during two consecutive days. Next, the frequency-domain "weighted tau" method is applied to compute the values of the delays. This method is used with the options, identified to provide best results in the previous section.

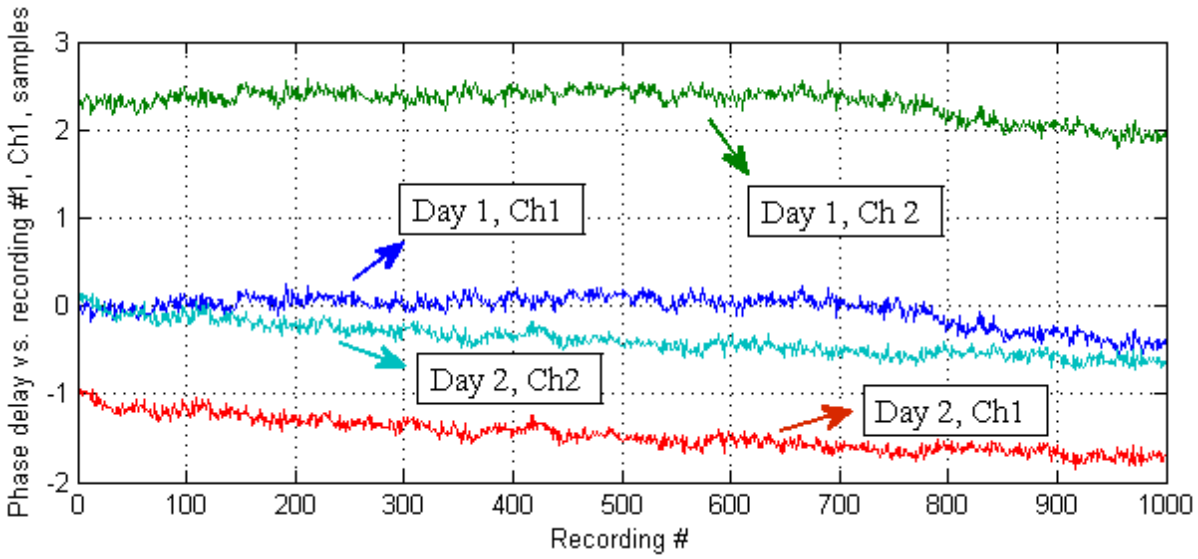

Fig. 5.21 Estimated values of ΔT_1 ("Ch1") and ΔT_2 ("Ch2") for two sets of 1000 recordings during two consecutive days.

Figure 5.21 represents estimated values of ΔT_1 and ΔT_2 for both days with respect to the recording number. From the figure, one may identify the following behavior of the phase: a) the phase jitter in both channels is present and is on the level of 0.2 samples; b) significant drift of the phase delays is seen in both channels; c) the phase drift is synchronous between the channels; d) there is a significant phase offset between the channels; e) the offset significantly varies from day to day, but is constant throughout one recording session[3].

In order to demonstrate property c) and that the offset between the channels is stable during one session, the plot of ΔT_{12} is presented in Fig. 5.22. The flatness of the delay

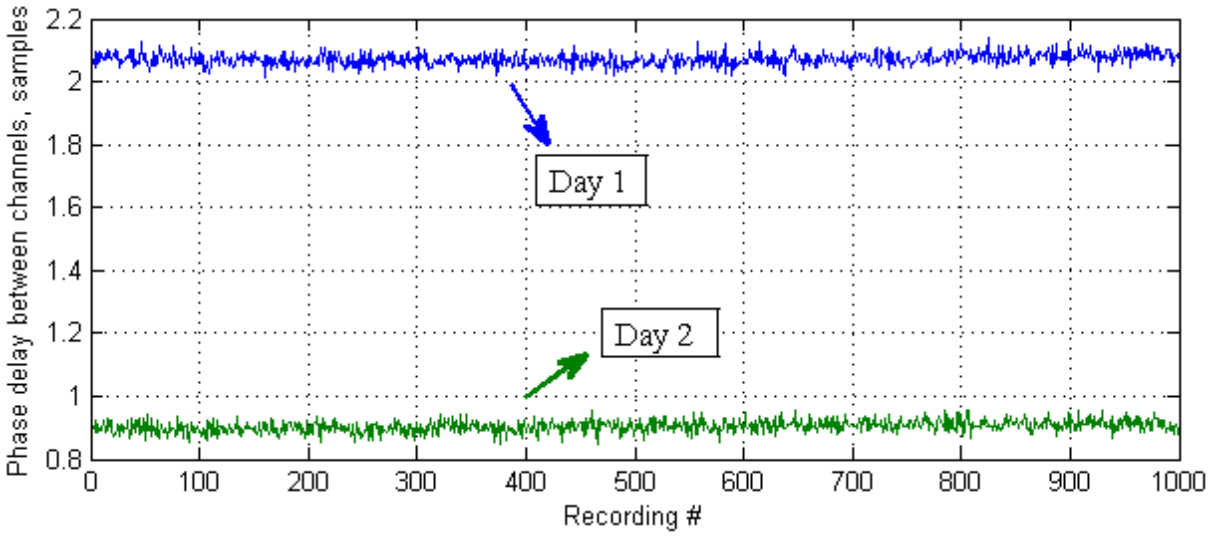

Fig. 5.22 Estimated values of ΔT_{12} for two sets of 1000 recordings during two consecutive days.

between the two channels proves the hypothesis that the ΔT_{12} has only low random jitter and constant offset. However, a significant factor that might prevent efficient phase delay compensation is the varying offset between the channels from session to session. In order to mitigate the effect of the offset, self-calibration of the scope can be augmented with additional cross-channel offset estimation recordings (similar to those discussed in this chapter). The estimated phase delay then can be used to compensate for the overall phase uncertainty in the recordings.

[3]One session is referred to a procedure that includes self-calibration of the oscilloscope at the beginning, followed by multiple signal recordings without re-calibration of the oscilloscope.

Assessment of performance of the alignment method

In order to demonstrate the improvement that the compensation method can provide, two sessions of recordings are performed, one per day, during two consecutive days. At each session 1000 pairs of signals shown in Fig. 5.19 are recorded. For each recording the following parameters are varied:

1. Recording mode of the oscilloscope[4]:
    - "s" - no averaging;
    - "hw2" - hardware "multiple" averaging with 2 averages;
    - "hw16" - hardware "multiple" averaging with 16 averages;
    - "hw32" - hardware "multiple" averaging with 32 averages;
    - "hws2" - hardware "stable" averaging with 2 averages;
    - "hws16" - hardware "stable" averaging with 16 averages;
    - "hws32" - hardware "stable" averaging with 32 averages.
2. Sampling rate:
    - 40 Gs/s;
    - 50 Gs/s;
    - 80 Gs/s;
    - 100 Gs/s.

Thus, in total two sets of 28000 pairs of recorded signals are analyzed. For illustration, the chapter first presents the result of the alignment on two pairs of signals, collected at the highest sampling rate, with 32 averages in the "stable" averaging mode. These recording settings provide the lowest noise among all others, thereby resulting in the signals that are easier to analyze.

Fig. 5.23a and 5.23b represent two recorded reference signals and two RF pulses, respectively. These two pairs of signals come from two different sessions. Phase delay

[4]Refer to [195] for the description of the averaging modes of the oscilloscope

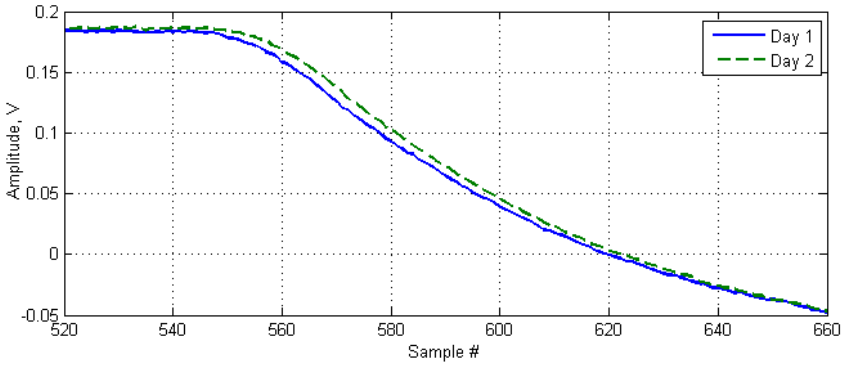

(a)

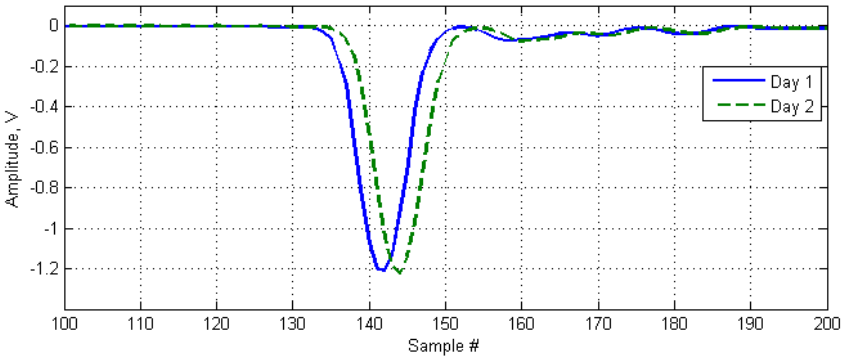

(b)

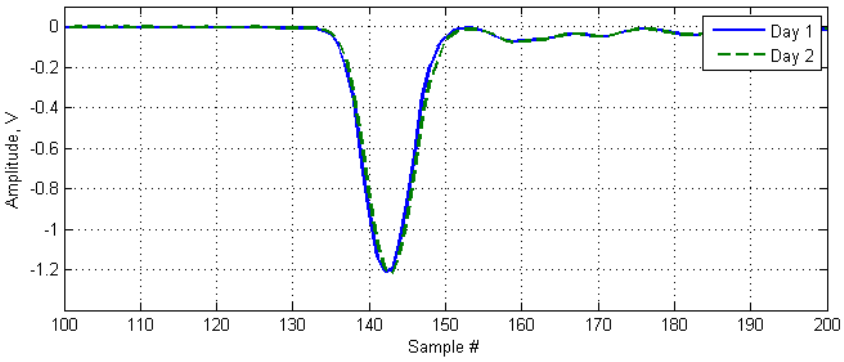

(c)

Fig. 5.23 Recorded reference signals (a) and microwave pulses before alignment (b) and after alignment (c). Recording mode of the oscilloscope: 100 Gs/s, "stable" averaging, 32 averages.

between the RF pulses is clearly seen on the graph 5.23b. The delay between the reference signals is detected and used to align the RF pulses, recorded at channel 1 of the oscilloscope. Fig. 5.23c plots the RF pulses after the alignment. The improvement is clearly observed.

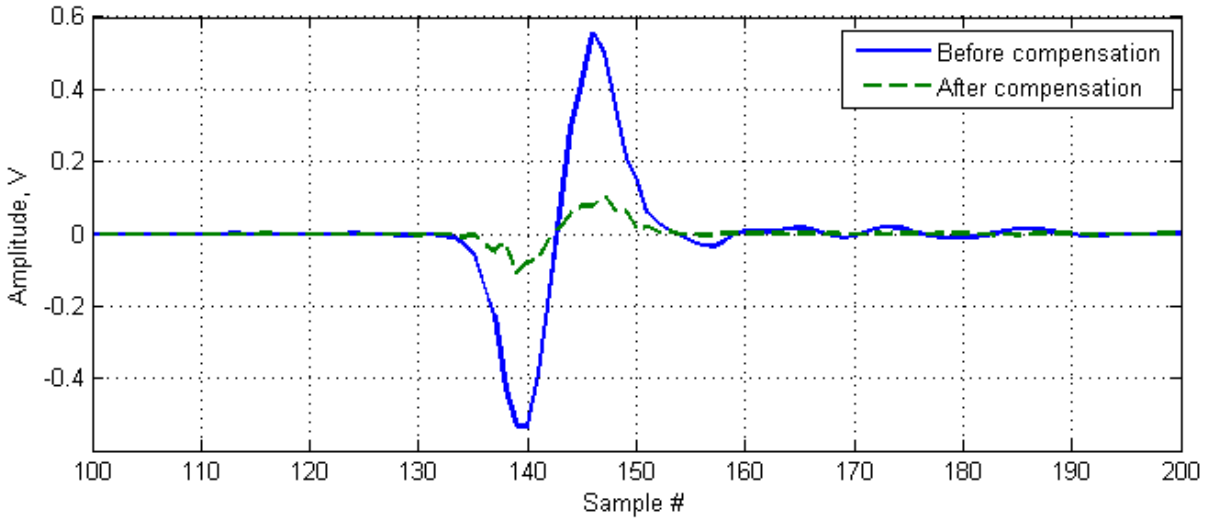

Fig. 5.24 Difference signals after subtracting non-aligned and aligned microwave pulses.

Next, the two recorded pulses are subtracted before their alignment and after the alignment. The result is represented in Fig. 5.24. The absolute maxima of the difference signals are $0.56V$ and $0.11V$ before and after the alignment respectively. The computed power of the pulse is $18 \cdot 10^{-3}$ and $0.57 \cdot 10^{-3}$ (units of the computed power are meaningless since samples are used for the time scale and no load impedance is specified).

The presented alignment case was one of the most successful. The values of the residual pulse absolute maximum and power of all the signals recorded with the oscilloscope settings, mentioned above, are represented in figures 5.25a and 5.25b. The plots demonstrate that the compensation for the phase delay is successful for all signals. It can be also seen from the figures that the phase error between the recorded signals is increasing with time, starting after the oscilloscope calibration. This phenomenon is expected, since the oscilloscope self-calibrates only for the conditions at the beginning of the session. After that time, these conditions slowly change.

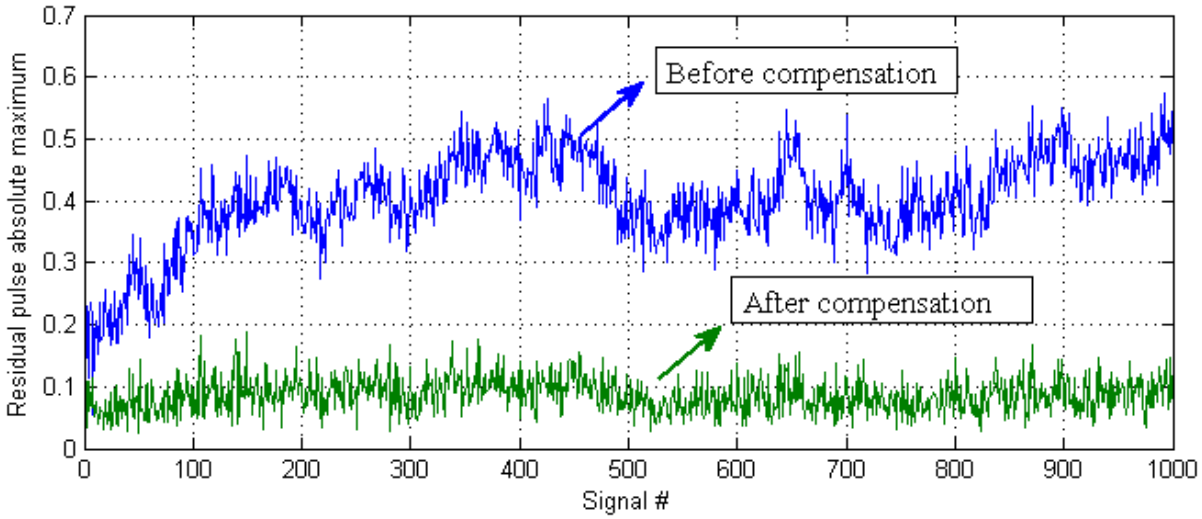

(a) Absolute maxima

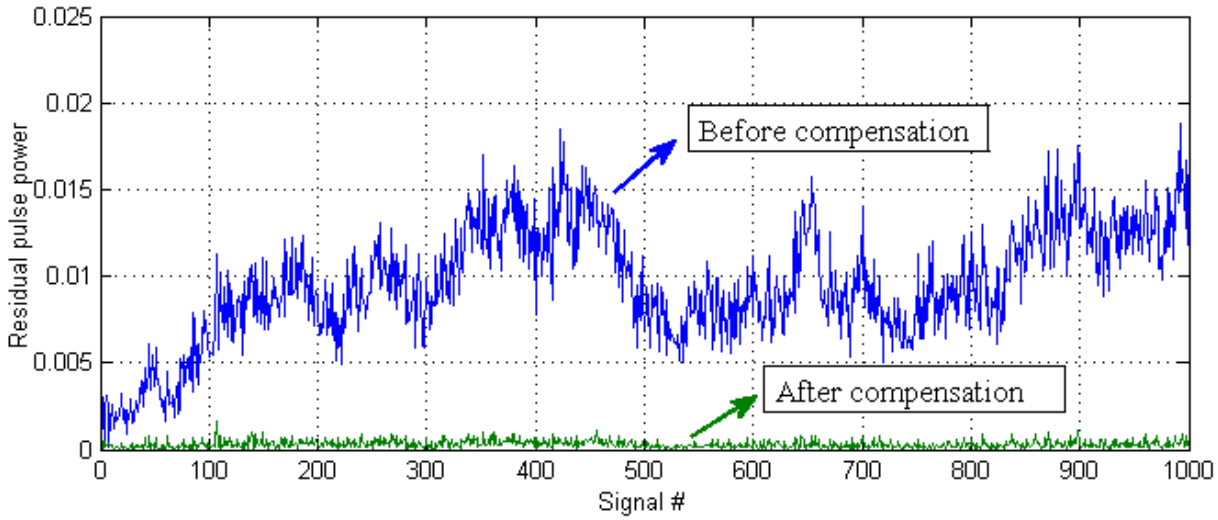

(b) Residual pulse power

Fig. 5.25 Computed metrics of difference signals before and after phase compensation.

The mean values of the residual pulse absolute maxima and the power for all other combinations of the recording modes and the sampling rates have been computed (figures 5.26 and 5.27).

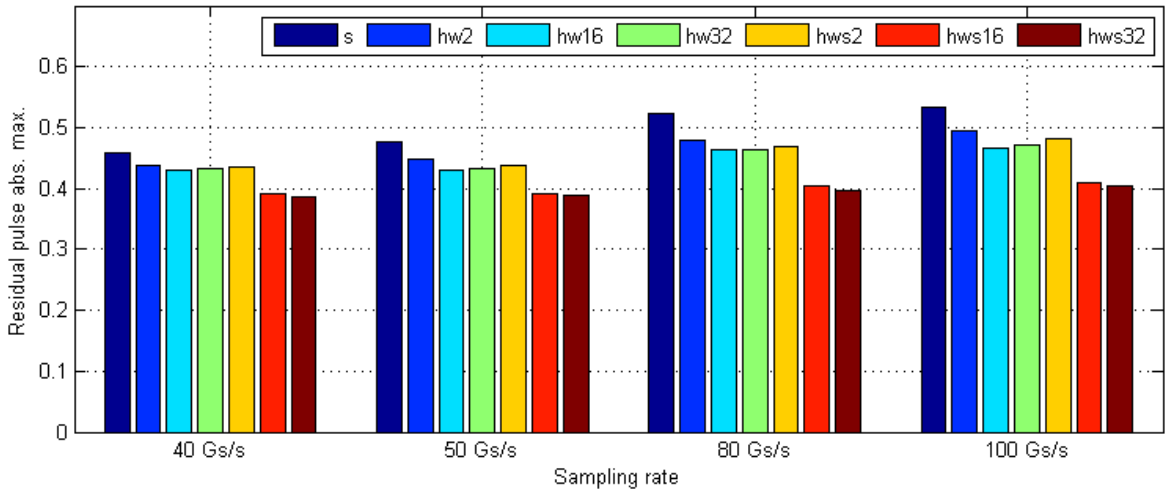

(a) Before alignment

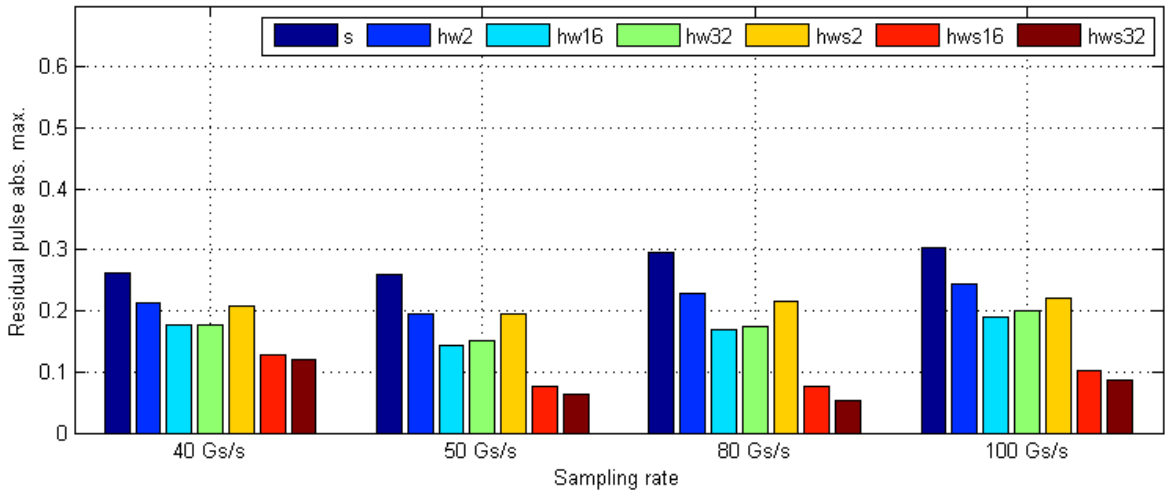

(b) After alignment

Fig. 5.26 Average absolute maxima of difference signals for various recording modes.

It can be seen that both residual pulse power and absolute maxima are higher for modes with higher sampling rates. This is explained by the fact that the peak of the residual pulse is more visible and the pulse contains more samples at higher sampling rates (thus, computed power is higher). Higher number of averages and "stable" averaging mode result in weaker residual pulse for both non-aligned and aligned signals. Next, the graphs show

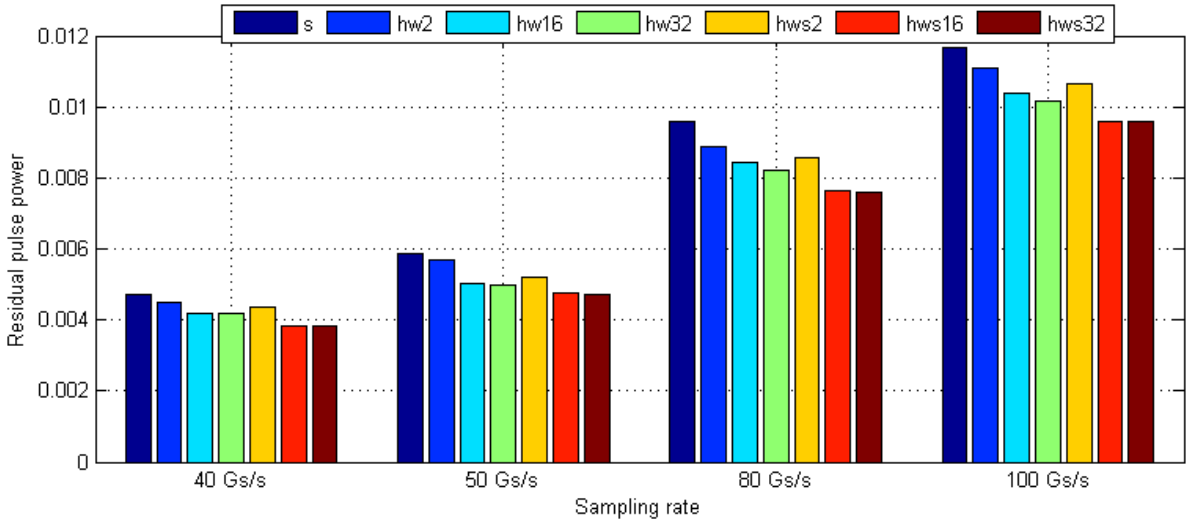

(a) Before alignment

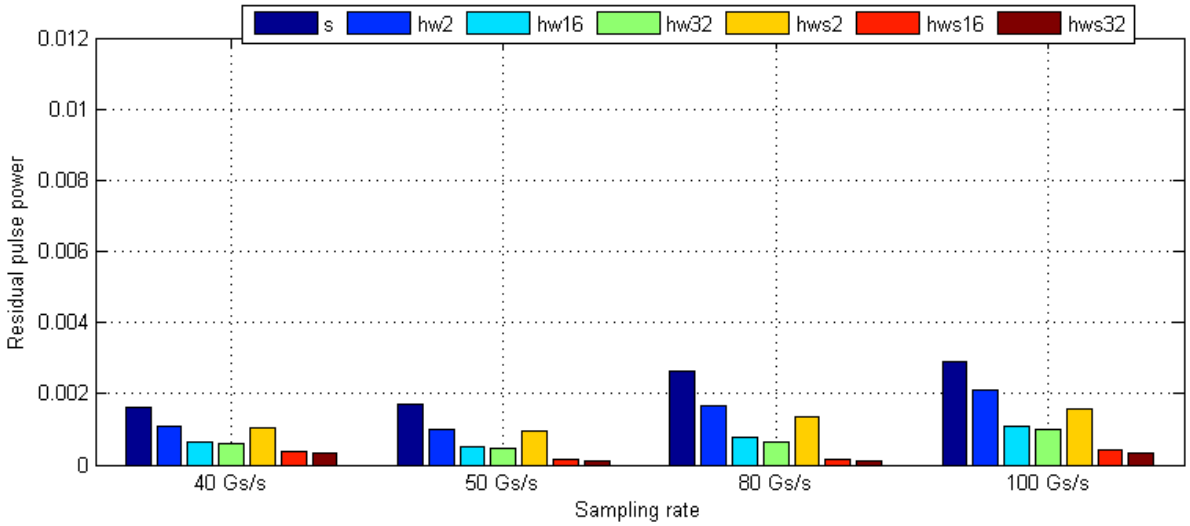

(b) After alignment

Fig. 5.27 Average residual pulse power of difference signals for various recording modes.

that for all recording modes, the alignment of signals reduces the residual pulse. However, optimal performance is achieved at sampling rate 80 Gs/s: residual pulse amplitude is reduced almost by a factor of 8 for "hws32" averaging and by a factor of 6 for "hws16".

5.4 Conclusions

This chapter presented the description of the requirements and the design of the first-generation experimental system in the research group at McGill University. The signals recorded by the data collection system were analyzed and potential factors of uncertainties that might prevent successful microwave imaging were discussed.

Phase error in the recorded signals is one of the identified sources of uncertainty. The source of the phase errors is related to the sampling equipment and cannot be easily eliminated by hardware techniques. In order to address this challenge, a method to adjust the phase of the recorded signals in software was proposed. This method is based on the analysis of the additional reference signals, recorded at the second channel of the oscilloscope.

The study shows that the phase error of both channels of the oscilloscope is stable throughout one recording session, thus allowing to compensate the phase drift with respect to the trigger event. The results demonstrated that this alignment method is efficient when applied to experimentally recorded RF signals. The recommendation for further recordings is to use 80 Gs/s sample rate of the oscilloscope with "stable" averaging mode and 16 or 32 averages.

The performance of this method can be further improved by compensating for the phase offset between the two channels. This offset can be estimated from additional recordings, done at the beginning of each session, after self-calibration of the oscilloscope.

Although this method demonstrated high performance in minimizing the residual pulse, the performance of the calibration procedure can be improved if pairwise analysis of the direct pulses is used instead of reference signals. Thus, the signal alignment procedure can be done in two steps: first all the signals are aligned based on the described method using "reference" signals; next, second additional alignment based on pairwise direct pulse analysis is done only for calibration purpose. This sequence will both minimize the residual pulse and align the signals between the channels to improve the sharpness of the microwave images.

Chapter 6

Ultrawide-band microwave breast imaging algorithms

This chapter focuses on the analysis of microwave imaging algorithms and discusses ways to improve their efficiency.

First, a study is presented that evaluates contemporary microwave breast imaging algorithms on a series of two-dimensional numerical breast models. Section 6.1 discusses the methodology and results of the algorithm assessment.

Second, section 6.2 discusses two approaches to improve the DMAS and DAS algorithms in order to significantly reduce the amount of computations and improve the image quality. The computational efficiency of the improved DMAS and the frequency-domain counterpart of the DAS algorithm, DASf, is analyzed. The study evaluates the algorithm performance on the signals recorded with the experimental system, from breast mimicking phantoms.

The chapter concludes with a discussion on further development of the microwave imaging algorithms.

6.1 Evaluation of the monostatic microwave radar algorithms on two-dimensional numerical breast models

6.1.1 Methodology

The presented study evaluates beamforming imaging algorithms as well as the hypothesis testing approach. Five algorithms representing both approaches that are mostly discussed in the literature are selected for the evaluation. Data-independent beamforming is represented by the conventional Delay-And-Sum (DAS) algorithm, its modified version, Delay-Multiply-And-Sum (DMAS) and more advanced Filter-And-Sum (FAS) beamforming. In order to evaluate robust beamformers, Robust Capon Beamformer (RCB) was implemented. The hypothesis testing approach is represented by the Generalized Likelihood Ratio Test (GLRT) algorithm. Theoretical description of these algorithms was given in chapter 3.

Breast Models

This evaluation study works with the signals obtained by numerical two-dimensional simulations. As a numerical representation of a human breast we consider coronal slices of circular shape (Fig. 6.1). The internal tissue structure of the breast is derived from MRI images and enclosed by a 1.6-mm thick skin. The selection of circular shape for the breast models is intentional - it helps provide identical skin-breast artifact seen at all antennas. In such a scenario the artifact can be easily removed from the signals by the average-subtract algorithm (refer to section 3.2), which allows to focus on the performance of the imaging algorithms while avoiding the additional factor due to the performance of the artifact removal algorithms. The dielectric properties of the tissue are described by a one-pole Debye model with four parameters, given by (3.6). As presented in Table 6.1, for each series, the values of $\Delta\epsilon$ and τ of the pixels are assigned to some constants. The values of ϵ_∞, and σ_s are assigned according to the linear mapping from the pixel intensities to ϵ_∞ in the range of $\epsilon_{\infty,b}\,(1 \pm 0.01\nu/2)$ and to σ_s in the range of $\sigma_{s,b}\,(1 \pm 0.01\nu/2)$, where $\epsilon_{\infty,b}$ and $\sigma_{s,b}$ denote the mean values, and ν denotes the

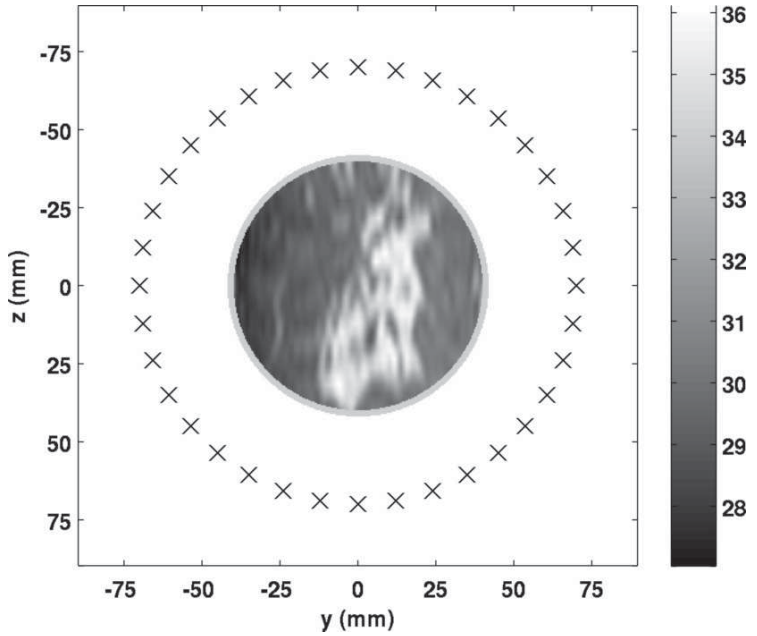

Fig. 6.1 Coronary slice of the permittivity extracted from one of the healthy breast phantoms. The locations of the current sources are marked by ×.

percentage of variation. The resulting expression for ϵ_∞ and σ_s are given by:

$$\epsilon_\infty(p) = \epsilon_{\infty,b}\left(1 + \frac{\nu}{2} - \frac{M(p) - \min(M)}{\max(M) - \min(M)}\nu\right) \quad , \tag{6.1}$$

$$\sigma_s(p) = \sigma_{s,b}\left(1 + \frac{\nu}{2} - \frac{M(p) - \min(M)}{\max(M) - \min(M)}\nu\right) \quad , \tag{6.2}$$

where p is the pixel number in the MRI image M and in the corresponding material map; ν denotes the percent of variation, which defines the level of heterogeneity of the breast tissue (Table 6.1).

Table 6.1 Tissue properties for data series

Series	Debye model parameters				$\nu \times 100$ (%)	$\min(\epsilon_{r,m}/\epsilon_{r,b})$	$\max(\epsilon_{r,m}/\epsilon_{r,b})$	$\min(\sigma_m/\sigma_b)$	$\max(\sigma_m/\sigma_b)$
	$\epsilon_{\infty,b}$	$\sigma_{s,b}$ (S/m)	$\Delta\epsilon$	τ (ps)					
1	3.1	0.05	1.6	13	7	10.6	11.1	24.8	25.1
2	13.0	0.4	24.4	13	30	1.4	1.6	1.7	1.8
3	13.0	0.4	24.4	13	70	1.3	1.7	1.7	1.8
4	13.8	0.7	35.6	13	30	1.1	1.2	1.2	1.2

The selection of the series properties can be explained as follows. Series 1 represents the case of the highest tumor-tissue contrast in dielectric properties and the lowest level of heterogeneity. This corresponds to adipose-dominant breast models and is the easiest case from the detection point of view. Series 2 and 3 are based on the same contrast level, much lower than that for Series 1, and they differ in the level of heterogeneity. Series 3 represents a highly heterogeneous case. Series 4, having the contrast ratio close to 1, is considered to be the most difficult from the detection point of view and is referred to as "extremely dense". Average level of heterogeneity of 30% has been chosen for this series.

In Table 6.1, columns $\min(\epsilon_{r,m}/\epsilon_{r,b})$, $\max(\epsilon_{r,m}/\epsilon_{r,b})$, $\min(\sigma_m/\sigma_b)$, and $\max(\sigma_m/\sigma_b)$ represent the minimum and maximum ratios of the relative permittivity and conductivity between the tumor and the healthy tissue after the tissue assignment, respectively. The dielectric properties in the table are given for the frequency of 6.85 GHz.

Finite-Difference Time-Domain Simulations

Fig. 6.1 shows an example of a breast model and the simulation scenario. The breast is placed in an oil-like lossless non-dispersive matching medium characterized by ($\epsilon' = 4.5, \sigma = 0$). A tumor with 3-mm radius, characterized by its Debye parameters ($\epsilon_\infty = 6.75$, $\sigma_s = 0.79$ S/m, $\Delta\epsilon = 48.35$, $\tau = 10.47$ ps), is placed inside the model. There are 36 equally-spaced current sources placed around the breast at a fixed distance (28 mm away from the skin). Each source sequentially emits a differentiated Gaussian pulse with a 3 dB bandwidth from 3.1 to 10.6 GHz. In this work, the monostatic scenario is considered, which results in 36 recorded signals for a breast model. The minimum wavelength, determined by the largest permittivity at 10.6 GHz, is 3.87 mm. We set the spatial increment to 0.4 mm and the relative Courant number to 0.999 to reduce the dispersion error. The time step is 2 ps. The maximum wavelength in the heterogeneous tissue at 3.1 GHz is 50.3 mm. We place 12 perfectly-matched layers at a half of this wavelength away from the sources to truncate the computation domain. Prior to the application of the imaging algorithms, we apply the average-subtract method to remove the skin-breast artifact. Then, the signals are down-sampled from 500 GHz to 64 GHz.

Datasets

In order to provide sufficient statistics for the performance assessment, generated ten different breast models containing tumor at different locations have been generated and used in the simulation procedure, described above, in order to obtain the signals received at each of the antennas. The same procedure has been applied to exactly the same tissue structures without tumor inside, which have been used to compute the performance metrics described further.

For the GLRT algorithm, in addition to the ten tissue structures, thirty more healthy breast models have been produced to estimate the covariance matrices needed for the algorithm. The same set of tissue structures with the assigned tumor locations have been used for each of the four series. The difference between the series is only in the tumor/tissue properties contrast and the level of heterogeneity. Besides the decrease in the number of breast phantoms needed for the experiments, fixing tissue structures between the series removes the factor of variability, which is beneficial for system performance comparison.

6.1.2 Results and discussion

The imaging algorithms mentioned above have been applied to each of the data sets to obtain the images shown in Fig. 6.2. Performance metrics described in section 3.7 have been computed and are presented in Fig. 6.3 - 6.5. Only the cases with correct detection have been taken into account to compute the average value and standard deviation of the metrics. When there are insufficient successful detections to allow adequate evaluation of performance metrics, this is labeled in the figures as 'FAILED'.

Table 6.2 Number of incorrect tumor detections

	Series 1	Series 2	Series 3	Series 4
DAS	0	0	0	10
DMAS	0	0	0	10
FAS	0	1	1	9
GLRT	0	0	0	2
RCB	0	0	3	6

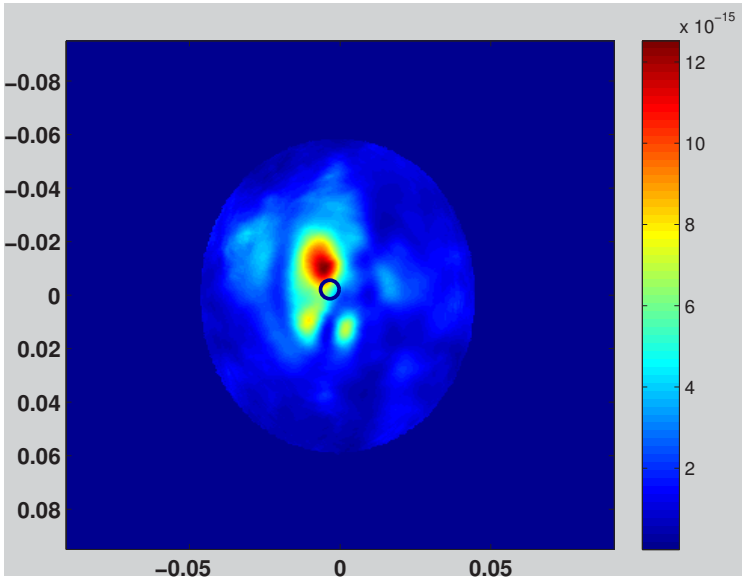

(a)

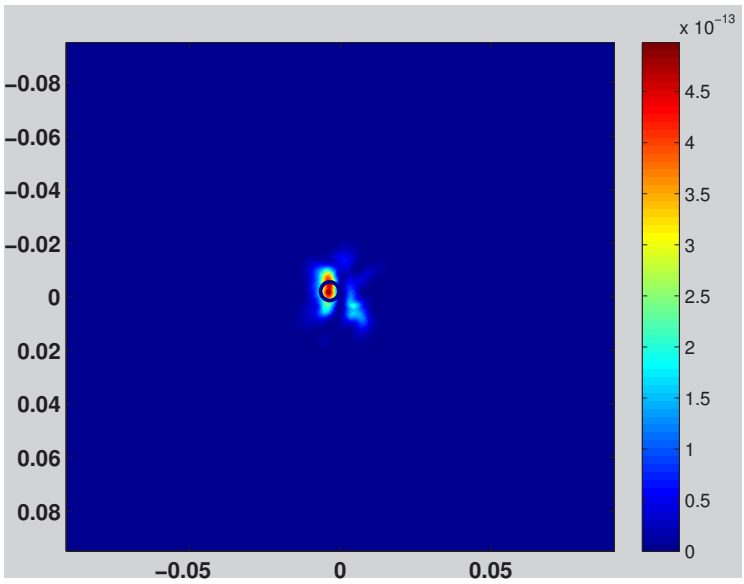

(b)

Fig. 6.2 Output images for the delay-and-sum algorithm (a) and filter-and-sum algorithm (b), applied to the Series 1 breast model (almost-entirely-fat).

Table 6.2 contains the number of incorrectly detected tumors for each series. By analyzing the table, it can be seen that most of the algorithms fail under the conditions of low contrast. The only reliable algorithm in such a scenario is the GLRT, which incorporates

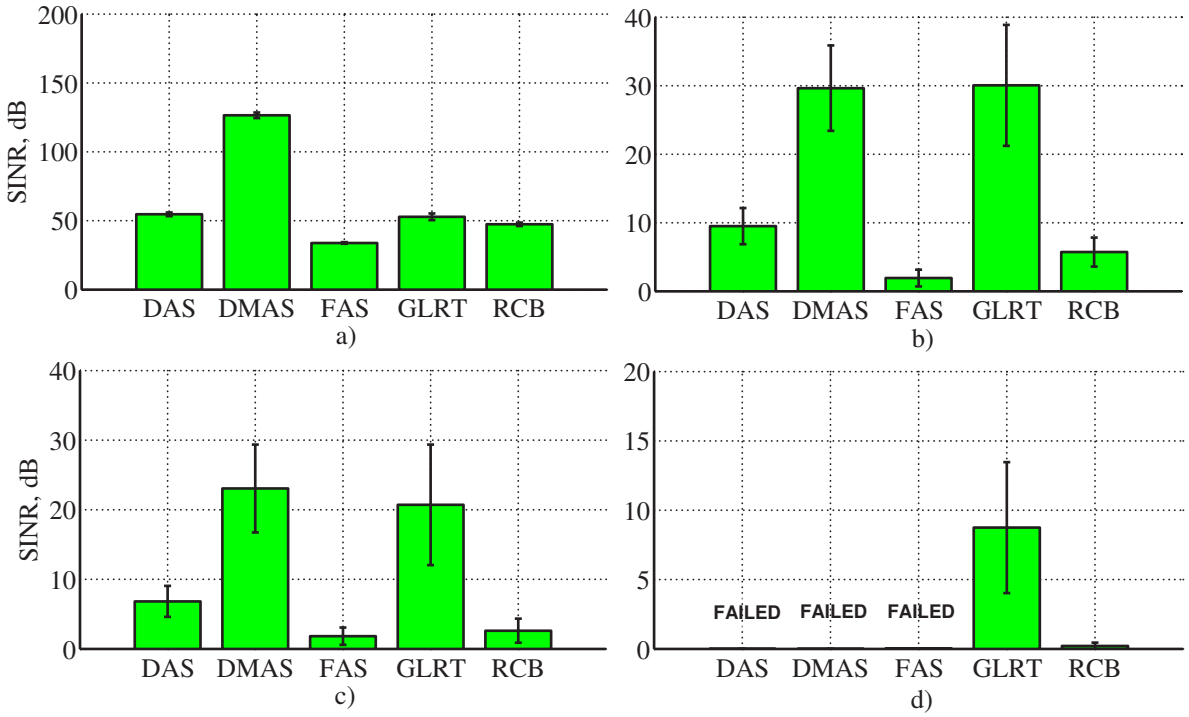

Fig. 6.3 Signal-to-interference-and-noise ratio for a) Series 1 b) Series 2 c) Series 3 and d) Series 4. Note that the scales in the four plots are not the same.

EM propagation model of high complexity, capable to describe the effects of scattering from the tumor. In conjunction with Fig. 6.3, one may notice that the simple algorithms such as DAS and DMAS are rather stable and successful under the high and medium tissue/tumor dielectric contrast levels. However, they fail under the extremely dense scenario. The FAS algorithm, which incorporates the effects of dispersion, exhibits marginal improvement over DAS and DMAS when the complexity of the model increases. The adaptive RCB algorithm demonstrates a gradual decrease in performance with the contrast decrease and heterogeneity growth. It is capable to detect tumor in four cases out of ten in the extremely dense scenario. This is explained by its adaptive nature to the input data. By comparing Fig. 6.3 b) and c), it is seen that the increase in heterogeneity from 30% to 70% decreases SINR by 2 to 10 dB.

Fig. 6.4 represents the results of tumor localization accuracy. It is observed that, for the easiest imaging scenario (Series 1), almost all of the algorithms localize the tumor up to the image resolution (1-mm grid). DAS/DMAS show comparable results and outperform all

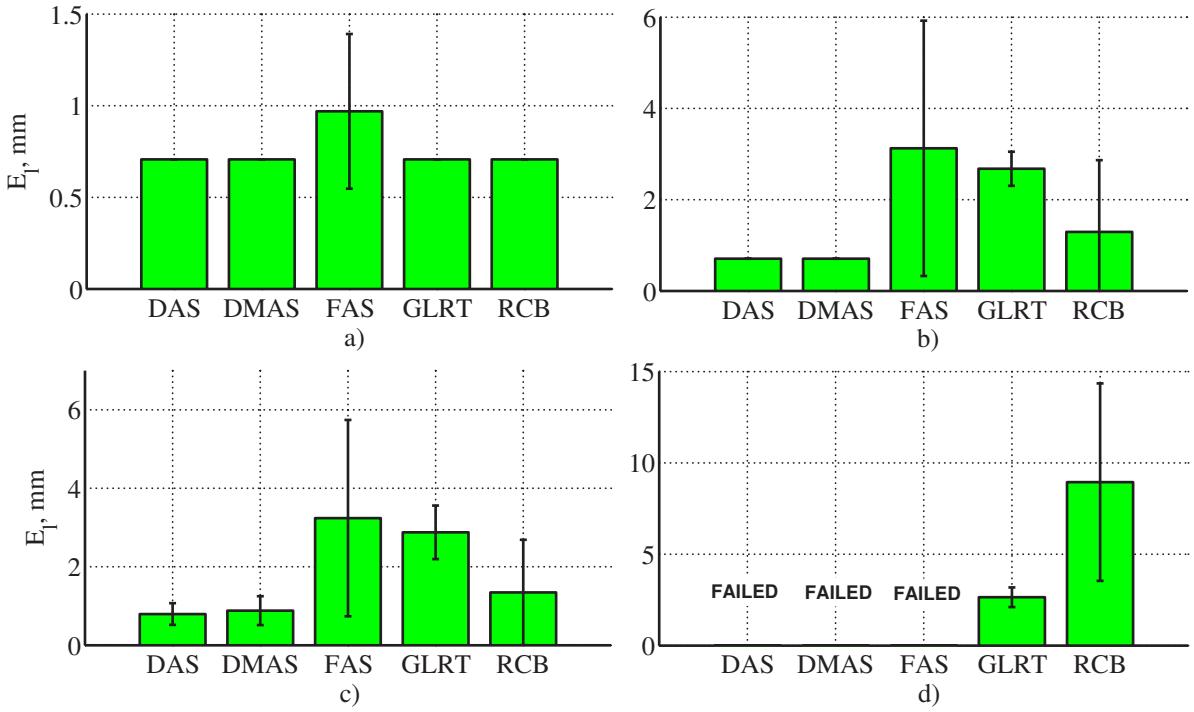

Fig. 6.4 Localization errors E_l for a) Series 1 b) Series 2 c) Series 3 and d) Series 4. Note that the scales in the four plots are not the same.

other algorithms. The FAS algorithm gives lower performance due to the point scatterer assumption and the regularization procedure. Heterogeneity does not play an important role for the localization (compare Fig. 6.4, b) and c)).

The ability of the algorithms to isolate the tumor response by suppressing the clutter can be estimated by metric PSLR (Fig. 6.5). The best performance for the easiest scenario is achieved by the RCB algorithm, due to its adaptive capability. The good performance of the DMAS algorithm can be explained by the signal cross-multiplication between channels, which, in this case, acts as an effective clutter suppression mechanism. Similar to the SINR metric, the PSLR decreases by several decibels with the increase of heterogeneity.

From the presented results, it is seen that the performance of the algorithms differs with respect to different metrics. This suggests that certain algorithms should be selected to address specific tasks. As the GLRT algorithm provides reliable performance with metrics SINR and PSLR in all series, it is considered for further extension and improvement.

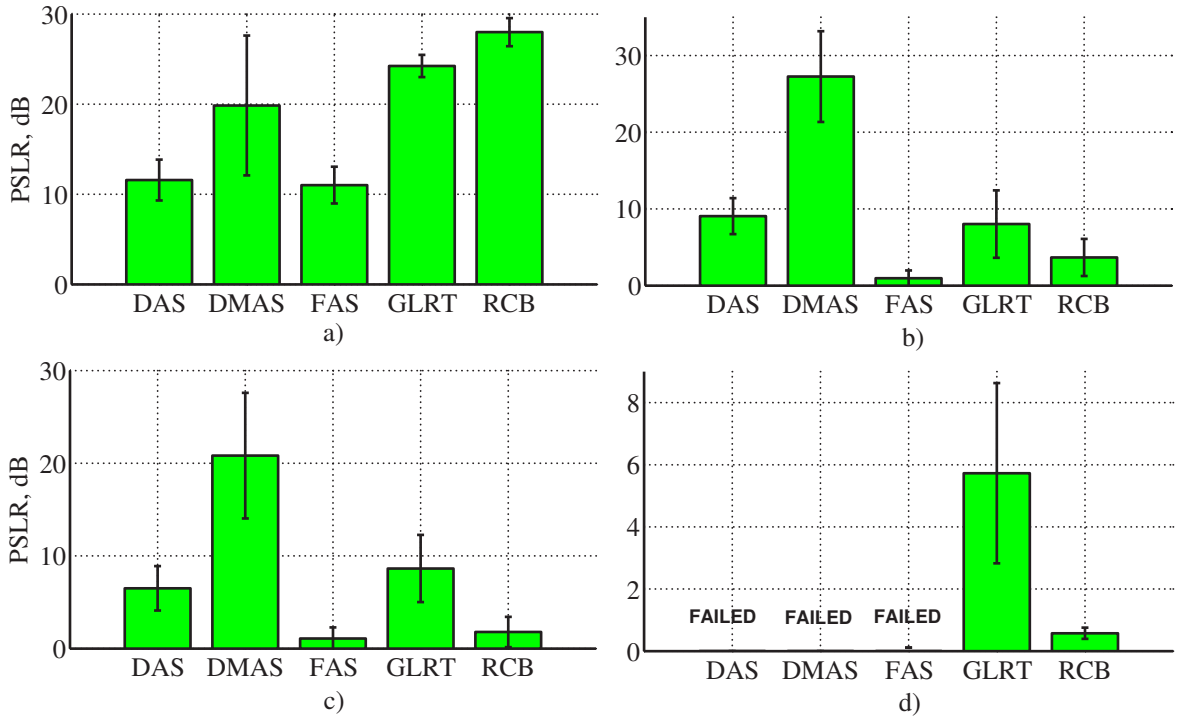

Fig. 6.5 Peak signal to sidelobe ratio a) Series 1 b) Series 2 c) Series 3 and d) Series 4. Note that the scales in the four plots are not the same.

6.1.3 Conclusions and future work

The first part of this chapter described the study of the performance of five microwave breast imaging algorithms, evaluated on the signals generated from the breast models with a reduced dielectric contrast and tissue heterogeneity.

The presented study shows that the DAS and DMAS algorithms exhibit small localization error in the generated images, but they fail in the scenarios of high breast tissue density. The FAS beamforming algorithm has an improved capability to image the models due to its rejection of interference, but is prone to localization errors. Under a good estimate of the average dielectric properties of the tissue and tumor, the hypothesis testing GLRT algorithm is capable of detecting tumors, in the sense of a good signal-to-interference-and-noise ratio. Since the microwave breast imaging strives to achieve the best SINR, the GLRT algorithm is the most promising for this aim. As the current GLRT algorithm handles monostatic signals, this study motivates to extend the GLRT algorithm to handle

multistatic signals.

6.2 The advancement of data-independent beamforming algorithms for microwave breast imaging

The analysis of the imaging algorithms described in the previous section has identified algorithms that offer increased performance when applied to the two-dimensional numerical breast phantoms with various degree of tissue heterogeneity and the level of dielectric contrast. On the other hand, further studies in our research group have revealed that in spite of demonstrating lower performance on the numerical data, algorithms such as the traditional DAS are still well applicable in the experimental studies - they produce microwave images with acceptable quality, with potential good detection of tumors in real patients. Being formulated in a more efficient way than advanced algorithms, DAS and DMAS algorithms can be improved to increase the computational performance without losing image quality.

This chapter presents two approaches to advance the performance of the DAS and DMAS algorithms. First, it is demonstrated that the DMAS algorithm, presented in the literature, can be reformulated in a different analytic expression, which significantly reduces the amount of required computations. In the second part of this chapter we propose a frequency-domain counterpart of the DAS algorithm, which both improves the computational performance and has a potential to improve the image quality.

It has been previously shown that data acquisition in the time domain can be carried out easier and faster than in the frequency domain [201]. However, processing of the collected signals in the frequency domain might provide certain benefits. For this purpose the pre-processed time-domain signals are converted into the frequency domain by applying the Fourier transform and further processing occurs in the frequency domain.

The author of this thesis proposes the **f**requency-domain version of the Delay-And-Sum beamformer (DASf) as a more computationally efficient replacement for the FAS beamforming, discussed earlier in the first part of this chapter.

6.2.1 Delay-multiply-and-sum algorithm: analysis of optimized version

The DMAS beamforming algorithm was described in section 3.6.1. The DMAS algorithm demonstrated high performance in the study reported in section 6.1 and in the studies by other research groups [127, 136]. However, the direct implementation of the DMAS, as presented in the mentioned studies, suffers from a serious drawback - the demand in computational resources. In fact, as shown further in this chapter, the DMAS algorithm is much slower in comparison to other algorithms, such as the conventional DAS. The analysis of the computational complexity shows that the DMAS presented in the literature can be considered as a second-order algorithm with respect to DAS. In order to support this argument and to explain how the DMAS algorithm can be optimized to lower computational cost, further analysis of the algorithm complexity is conducted.

The computational expense for the considered beamforming algorithms consists of the following two major contributions:

$$C_{bf} = C_c + C_o \quad , \tag{6.3}$$

Where C_c represents the computational cost related to the operation of compensation for spatial attenuation, spreading and delay (equation (3.37)); C_o denotes the number of operations spent for coherent summation and the computation of the beamformer output power given by (3.40) and (3.39), respectively. The term C_c is the same for all time-domain beamforming algorithms in this study, which eliminates C_c from the further analysis. However, the C_c term can dominate over the C_o since the cost to compute $H_{a,m,\ell}$ and $H_{sp,m,\ell}$ in (3.37) can vary significantly, depending on the considered propagation model.

For the DAS algorithm, the C_o is:

$$C_{o,DAS} = (M+1)N + 1 \quad . \tag{6.4}$$

In other words, the computational complexity is $\sim \mathcal{O}(MN)$.

For the DMAS algorithm, following (3.41), C_o is:

$$C_{o,DMAS} = (M(M-1)+1)N + 1 \quad , \tag{6.5}$$

Which is $\sim \mathcal{O}(M^2N)$ operations per voxel.

The analysis of expression (3.41) reveals that it can be simplified as follows:

$$\begin{aligned} z_\ell[n] &= \frac{1}{M(M-1)} \sum_{m=1}^{M} \sum_{\substack{k=1 \\ k\neq m}}^{M} \widetilde{x}_{m,\ell}[n]\widetilde{x}_{k,\ell}[n] \\ &= \frac{1}{M(M-1)} \left(\sum_{m=1}^{M} \sum_{k=1}^{M} \widetilde{x}_{m,\ell}[n]\widetilde{x}_{k,\ell}[n] - \sum_{m=1}^{M} \widetilde{x}_{m,\ell}[n]\widetilde{x}_{m,\ell}[n] \right) \\ &= \frac{1}{M(M-1)} \left(\sum_{m=1}^{M} \widetilde{x}_{m,\ell}[n] \sum_{k=1}^{M} \widetilde{x}_{k,\ell}[n] - \sum_{m=1}^{M} (\widetilde{x}_{m,\ell}[n])^2 \right) \\ &= \frac{1}{M(M-1)} \left((\sum_{m=1}^{M} \widetilde{x}_{m,\ell}[n])^2 - \sum_{m=1}^{M} (\widetilde{x}_{m,\ell}[n])^2 \right). \end{aligned} \tag{6.6}$$

The C_o for the optimized DMAS expression is:

$$C_{o,DMASo} = (3M+3)N + 1 \qquad , \tag{6.7}$$

Which is $\sim \mathcal{O}(3MN)$ operations per voxel.

Thus, by computing (6.6) instead of (3.41), the amount of computations can be significantly reduced. Further, in sections 6.2.3 and 6.2.4 the **o**ptimized version of the DMAS (DMASo) algorithm is applied to the experimental signals in order to demonstrate the improvement in computational performance.

6.2.2 Delay-and-sum beamforming in frequency domain

We next consider another approach to improve the data-independent algorithm DAS. In particular, we discuss the advantage of performing the signal processing in the frequency domain. The frequency-domain beamformer has been described in literature [202, 203]. This thesis adapts the same approach for use in microwave breast cancer detection.

It is assumed further that the collected digitized signals $\mathbf{x}_m$ are pre-processed in order to: a) filter-out measurement and other noise outside our range of interest (2 - 4 GHz) by a band-pass filter; b) remove direct pulses traveling from one antenna to another directly

by applying the calibration procedure, c) suppress the reflections from the skin surface by a filtering method described in [75]. The pre-processing procedures are described in section 3.2.

The resulting signals are then transformed into the frequency domain by applying the discrete Fourier transform. The resulting signal array can be represented by the signal model (3.28).

Similar to the time-domain DAS algorithm (see section 3.6.1), spatial focusing is applied to each of the points inside the breast domain $\ell = 1, \ldots, L$ to compensate for propagation effects. However, in the DASf algorithm the compensation occurs entirely in the frequency domain, enabling access to all the frequencies in the range of interest. This makes DASf more attractive for wide-band applications with high dispersion of the propagation media, which is the case for the breast cancer detection problem. Thus, a focused beamformer signal for location ℓ and channel m becomes:

$$\widetilde{Y}_{m,\ell}(\omega_n) = \frac{Y_m(\omega_n)}{A_{m,\ell}(\omega_n)} \quad , \tag{6.8}$$

The beamformer output is given by the channel-by-channel summation of focused signals:

$$Z_\ell(\omega_n) = \sum_{m=1}^{M} \widetilde{Y}_{m,\ell}(\omega_n) \quad . \tag{6.9}$$

Finally, the total beamformer power for a scan location ℓ is computed as follows:

$$p_\ell = \frac{1}{N} \sum_{n=1}^{N} |Z_\ell(\omega_n)|^2 \quad . \tag{6.10}$$

Visualization of p_ℓ with respect to the coordinates of the ℓ-th location produces two-dimensional or three-dimensional images of the scattering power within the breast region.

6.2.3 Methodology

The developed DMASo and the DASf algorithms are compared with the standard DMAS and two modifications of the conventional DAS algorithms: DASs and DASi, described in section 3.6.1. These algorithms are applied to the signals obtained from the experimental breast imaging system, described in detail in chapter 5 of this thesis and in [159].

This study involves the hemispherical breast-mimicking phantoms, imitating dielectric properties of the human breast [108]. The phantoms are placed in the radome of the experimental system (see chapter 5). The antenna array, integrated into the radome, consists of $M = 16$ elements. Each antenna in turn transmits a short pulse, produced by the pulse shaping circuit (described in [99]) and delivered to the antenna by the 16-by-2 blocking switching matrix (refer to section 5.2). The microwave response from the breast is recorded by a receiving antenna and further delivered by the switching matrix to a microwave sampler (we use equivalent-time sampling oscilloscope PicoScope 9201A [204]).

The data collection for one breast phantom results in 240 bi-static signals (the 16 monostatic signals are not recorded), which are used in the imaging. In this study, a tumor phantom of approximately spherical shape with radius 1 cm is introduced into the breast-mimicking phantom at the location x=30 mm; y=-30 mm; z=10 mm (Fig. 6.6).

For the demonstration of the performance three recordings with the same tumor location are used. These recordings were previously obtained by our research group [159]. The results presented further in this chapter are averaged across these three cases.

In order to demonstrate the performance of the algorithms with respect to the sampling rate of the input signals, the signals are downsampled to 80, 40, 20 and 10 GHz (which result in 2048, 1024, 512 and 256 samples in one signal, respectively). The number in the algorithm abbreviation will denote the number of samples in the source signals (e.g. DASf2048 will denote the DASf algorithm applied to the signals with 2048 samples).

6.2.4 Results and discussion

Fig. 6.7 represents the DASi2048 output image of the coronal slice at x=36mm, where the reflections from the tumor are the strongest in power. The tumor response is seen as the red spot in the lower left quadrant. In the zoomed-in regions with the tumor response

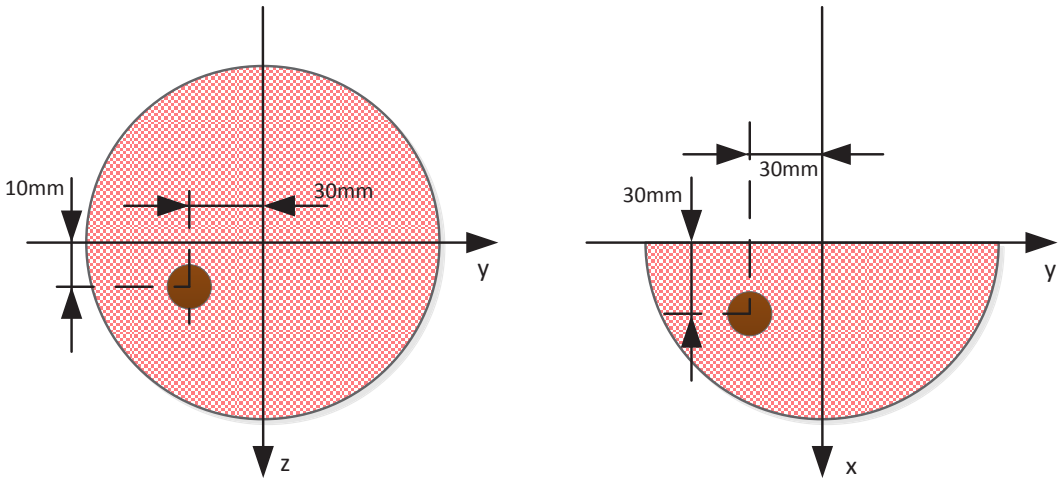

Fig. 6.6 Tumor is placed in the breast-mimicking phantom at location [30mm; -30mm; 10mm].

presented in Fig. 6.8, one can see that algorithms DASi2048 and DASf256 provide almost identical images. The DASs version of the algorithm demonstrates worse results, especially with 256 samples in the signals, where the tumor response is significantly distorted. The artifacts seen in Fig. 6.8,d) are associated with the coarse time-alignment.

The code to obtain the images was executed on a Matlab cluster with 16 nodes (each node is one core of Xeon 2.5 GHz quad-core processors). A summary of the execution time to obtain the whole three-dimensional image is shown in Fig. 6.9. The computational time agrees with the expected complexity of the algorithms: DASs being twice faster than DASi due to the interpolation procedure in the latter. The execution time for DASf is between the DASs and DASi for 2048 samples, but becomes the lowest as the number of samples in the signals decreases to 256. This highlights that the benefit of the decreased sampling rate for DASf is higher. At the same time, being the fastest, DASf256 offers image quality comparable to DASi2048 (the slowest).

This clearly demonstrates the benefits of signal-processing in the frequency domain: unlike using the time domain, it does not require interpolation, it is less time-consuming and it

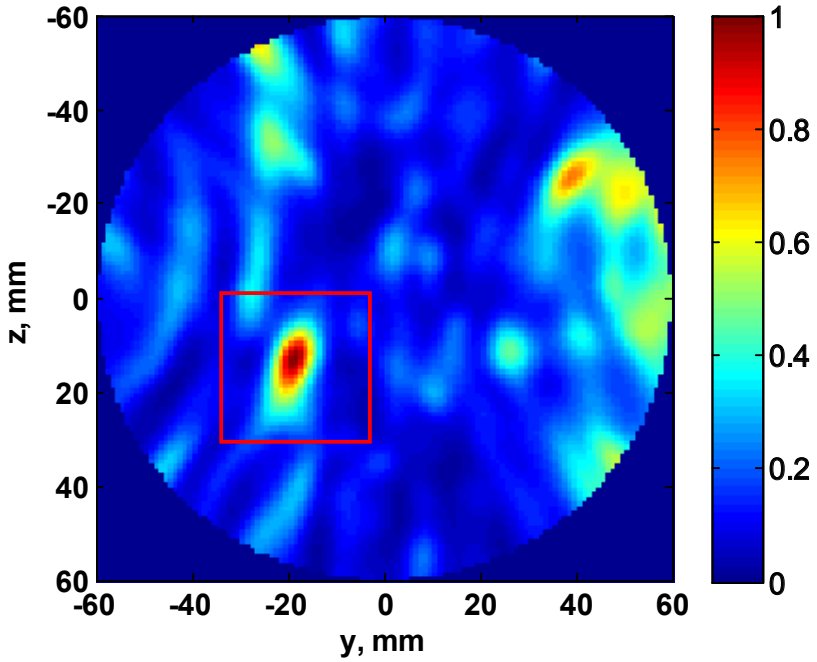

Fig. 6.7 Image slice at x=36 mm, given by the delay-and-sum algorithm with 2048 samples in the input signals and time-alignment with interpolation (DASi2048). The red square outlines the zoomed-in area for Fig. 6.8.

does not have the coarse time-alignment errors. It must be noted that the breast phantoms are made with fat-mimicking material with a relatively flat frequency characteristic of the dielectric properties (the material is not very dispersive). This is confirmed by the result of DAS2048 being comparable to the DASf. In general, for dispersive materials DASf offers a tool with a more convenient frequency-dependent properties compensation compared to DASi/DASs.

The computational efficiency of DASf can be further increased if only the frequencies in the range of interest are taken. For example, when working with the 256 samples and limiting the frequency range to 2 - 4 GHz, just 21 frequency values are taken into account, out of 129 (256/2+1).

Besides the discussed benefits, there are some drawbacks associated with the DASf algorithm. One significant limitation that could affect the computational efficiency arises when time-windowing is considered. In several works related to DAS, time-windowing after spatial focusing is performed (see e.g. [75]), which is intended to isolate the tumor

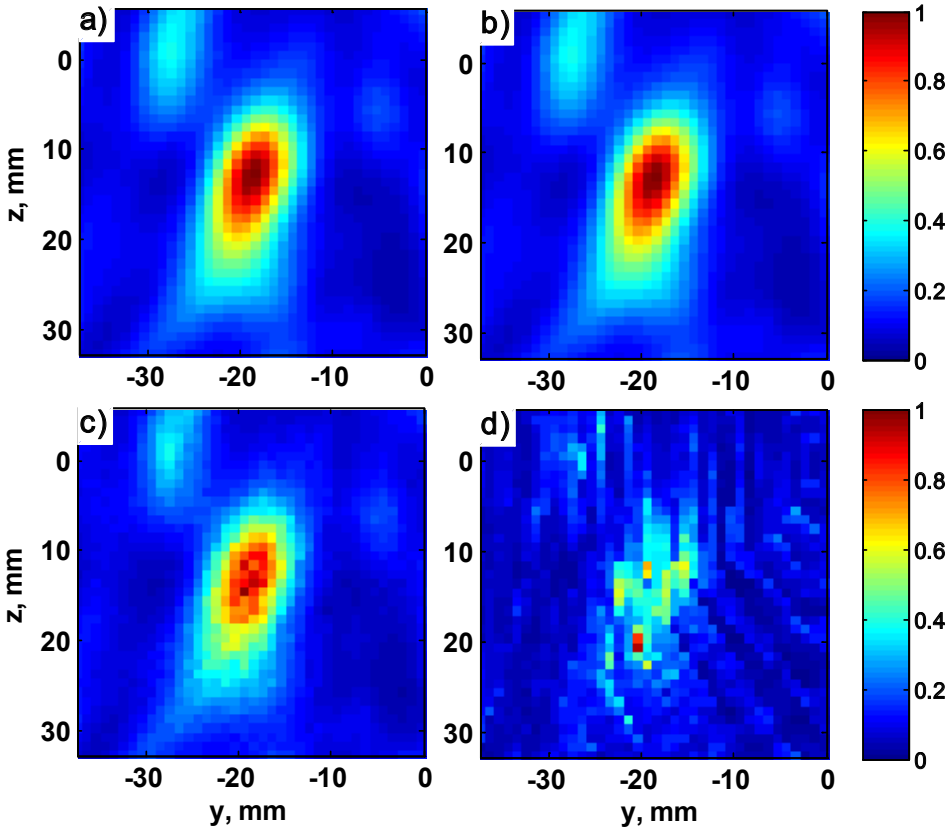

Fig. 6.8 Comparison of the selected area of interest (depicted in Fig. 6.7) between the following algorithms: a) DASi2048; b) DASf256; c) DASs2048; d) DASs256.

response in time. This procedure might improve the performance if the time of the reflection is known accurately enough. The equivalent operation in the frequency domain is the convolution, which is more computationally costly in frequency domain.

To assess the performance of the DMASo algorithm, an additional study was conducted and the discussed algorithms applied to another set of the signals described in [159]. An example image of the DMAS2048 output is shown in Fig. 6.10. This image is acquired in lower resolution (2 mm grid) than the image in Fig. 6.7 since the time to compute a high-resolution image for DMAS2048 is too high. Similar pictures are obtained for DASs, DASi, DASf and DMASo algorithms. Their performance in terms of SINR is very close and on average is $0.2 - 1.5$ dB. The tumour clearly stands out from the clutter, however due to the limitations of the data acquisition system and due to the limited number of antennas

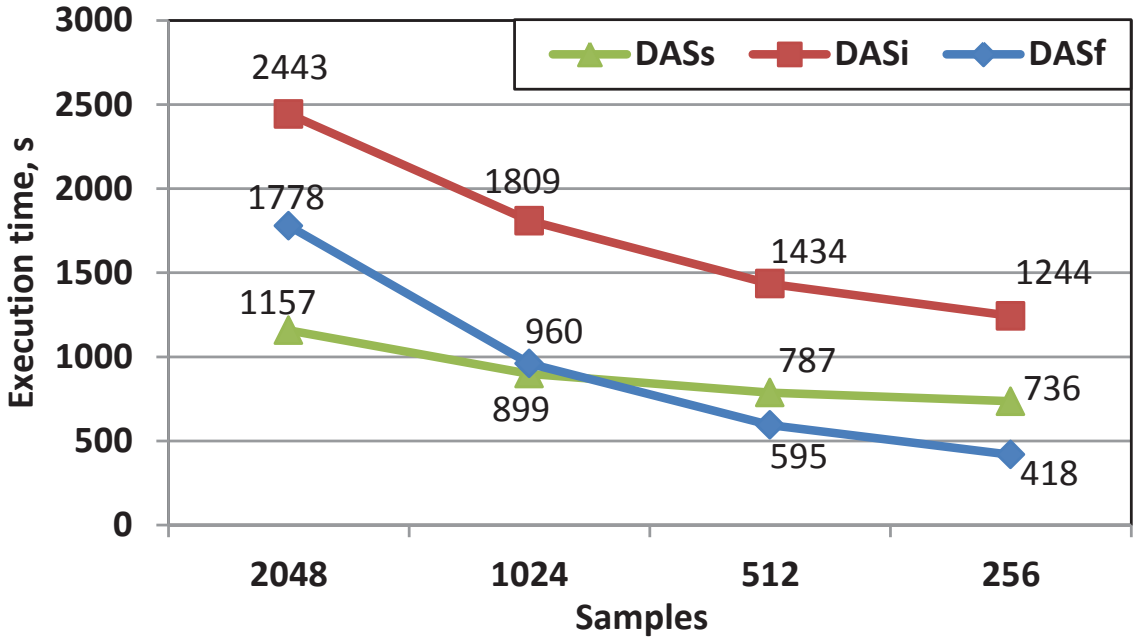

Fig. 6.9 Algorithm execution time for the whole three-dimensional image on a 16-node Matlab cluster.

and their placement, the performance is lower than that for the numerically simulated scenarios.

Table 6.3 represents the summary of the execution times spent to produce one slice of the three-dimensional image, averaged with respect to the slice number and the imaging case (in total, three cases were considered, as mentioned earlier in this section). From the Table 6.3, one can see that the results for the DASs, DASi and DASf agree well with those presented in the study of the DASf algorithm. The non-optimized version of the DMAS takes much more time to compute one slice than all other algorithms. On the other hand, the DMASo algorithm executes much faster than the DMAS and the result is comparable with the DASi algorithm (the applied DMAS algorithm performs coarse time alignment with the signals, thus taking less time in comparison to the DASi, but more time compared to the DASs algorithm). The images produced by the DMASo and DMAS algorithms match exactly, up to the round-off errors of the double-precision floating point arithmetic performed in Matlab, confirming the correctness of the derivations in (6.6) and the implementation in Matlab.

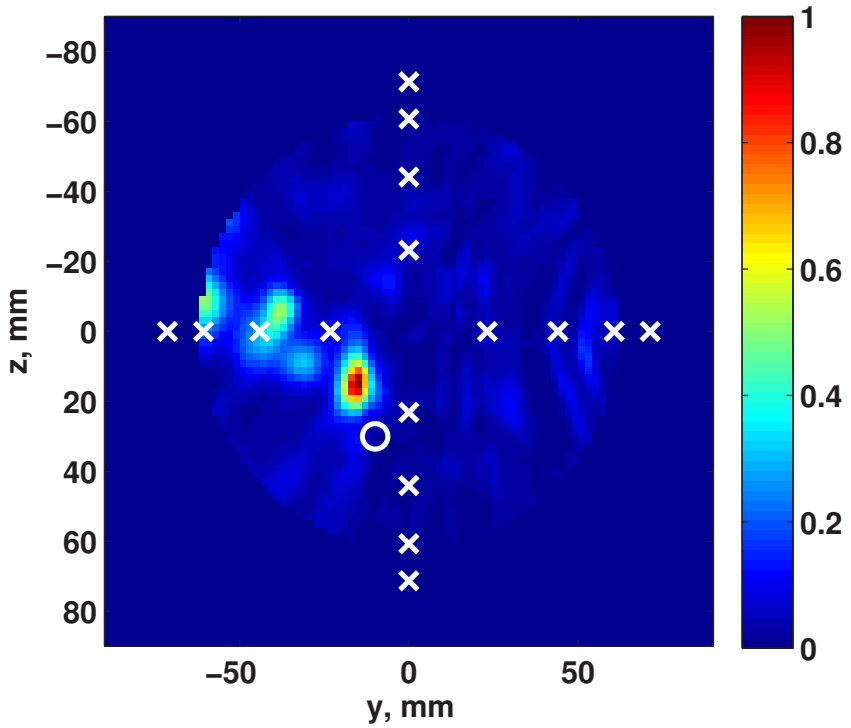

Fig. 6.10 Image slice at x=31 mm, produced by delay-multiply-and-sum algorithm with 2048 samples in the input signals.

6.2.5 Chapter summary

The conducted studies of the described DASf and DMASo algorithms demonstrate their significant improvement in computational performance compared to the conventional DAS and DMAS algorithms.

The DASf algorithm offers several benefits over the time-domain DAS. First, no oversampling of the recorded signals is needed to achieve optimal results, which reduces the computational complexity. as well as the requirements of the data acquisition system. Second, working with a selected frequency range can further improve the performance. In addition, DASf has potential for broadband processing: it allows easy incorporation of frequency-dependent properties of the propagation medium. The DASf algorithm can be used, in future work, as a basis for more advanced robust algorithms, required to improve the performance with the realistic signals recorded from the experimental system.

The computational performance of the DMAS algorithm was improved by analytically

Table 6.3 Computational time per slice, averaged across three cases, given in seconds

Algorithm	2048 samples	1024 samples	512 samples	256 samples
DASs	52.3	37.0	32.6	30.1
DASi	68.2	51.3	43.6	38.9
DASf	73.6	39.3	22.8	13.3
DMAS	1025.7	671.1	505.2	422.1
DMASo	64.6	48.3	42.4	36.9

optimizing the expression described in [127]. This improvement is critical for the systems with a large number of antennas, especially when considering multistatic signal arrays. The optimized analytical expression for DMASo significantly reduces the computational complexity of the DMAS algorithm and makes it comparable to the conventional DAS algorithm in execution time.

Chapter 7

Conclusions and future work

Microwave imaging has received significant attention during the past two decades. This interest can be primarily explained by the advancement of the RF technology, which has enabled data acquisition in the GHz frequency range. Computational performance of modern computers has grown tremendously, allowing implementation of complex image reconstruction algorithms.

In the effort to advance the microwave breast imaging system, the thesis presented several contributions.

First, a method to address inherent physical limitations of microwave breast imaging was explored (chapter 4). Limitations such as low spatial resolution due to the wave length and high amount of clutter in the recorded signals due to the heterogeneous breast tissues are hard to overcome using single imaging modality, such as microwave radar. In the presented study a dual-modality approach was employed in order to fuse signals of different physical origin: microwave and acoustic. An optimal rule to combine signals, collected from the MWR and MWIT modalities, was developed and compared to the MWR and MWIT, applied separately. In conclusion, the optimal fusion rule suffered from a significant bias, discriminating the information from the MWIT signals. To compensate for that, another "product" fusion rule was introduced, which demonstrated that the fusion method can yield increased performance compared to the single MWR and MWIT methods. Next steps in this research could involve three-dimensional numerically simulated data and/or data obtained experimentally.

Second, the advancement of the experimental data acquisition system was presented in chapter 5.

- Signals, recorded by the data acquisition system, were analyzed for the factors of variability. It was found that a significant factor of variability, relevant for the "differential imaging" approach, is the uncertainty in phase in the time-domain RF sampler (oscilloscope).

- Further research (section 5.3) demonstrated that the phase uncertainties of the oscilloscope can be compensated by time-aligning the signals based on the analysis of the "reference" signals, recorded at the second channel. In particular, it was identified that the phase uncertainty of the oscilloscope can be decomposed into three components: phase offset, phase drift and random jitter. As demonstrated in section 5.3.3, phase offset and phase drift can be compensated in software. It has been also identified that optimal recording mode of the oscilloscope is at around 80 Gs/s sampling rate, with 16 or 32 averages and with "stable" averaging mode. This information can be used for further improvement of the breast imaging system. Random phase jitter can be also significantly reduced by the software compensation, if optimal settings of the oscilloscope are used. Further work can confirm the performance of the phase alignment method based on the output microwave images. Additional compensation for the phase offset can be implemented and evaluated in future research.

Finally, a study of microwave imaging algorithms, applied to the time-domain microwave signals, was presented in chapter 6).

- Five algorithms, most presented in literature (DAS, DMAS, FAS, GLRT and RCB), were compared in the context of breast imaging application. It was found that, applied to highly heterogeneous and dense breast cases, only the GLRT algorithm can detect tumors. Nevertheless, DAS and DMAS have shown good performance for low-complexity imaging scenarios (i.e., for adipose-dominant breast tissues), while offering relatively low computational complexity. It must be admitted that the conducted evaluation study of the algorithms is not comprehensive. First, due to the limitations of the data acquisition system, our research group had to resort to

the numerical simulation studies. Second, due to computational limitations, only two-dimensional simulations were performed, with simplified assumptions of the system. As the computational capability increases with time and experimental data becomes available, it is suggested to repeat this study in future, without the limitations described above.

- Methods to optimize the DAS and the DMAS algorithms were explored. It was shown that the DMAS algorithm can be mathematically optimized. The resulting DMASo algorithm offers computational complexity comparable to that of DAS. Finally, a **f**requency-domain counterpart of the DAS algorithm (DASf) was developed. It was demonstrated that operating in frequency domain offers several benefits over the time-domain DAS. First, it can offer comparable performance to DAS on signals with much lower sampling rate. Second, it benefits from frequency-domain processing by limiting frequency range, applying weighting for different frequencies and compensating breast tissue dispersiveness. Further research in the area of microwave imaging algorithms could include the advancement of the DASf algorithm. One direction is to include compensation for the dispersiveness of the propagation media. Next, a robust approach can be applied to the DASf algorithm to adjust phase factor in the frequency domain, in a similar way to the Robust Capon Beamformer (RCB).

References

[1] E. Fear and M. Stuchly, "Microwave detection of breast cancer," *IEEE Trans. Microw. Theory Tech.*, vol. 48, no. 11, pp. 1854–1863, 2000.

[2] J. Sill and E. Fear, "Tissue sensing adaptive radar for breast cancer detection-experimental investigation of simple tumor models," *IEEE Transactions on Microwave Theory and Techniques*, vol. 53, no. 11, pp. 3312–3319, 2005.

[3] H. Kanj and M. Popovic, "A novel ultra-compact broadband antenna for microwave breast tumor detection," *Progress In Electromagnetics Research*, vol. 86, pp. 169–198, 2008.

[4] Canadian Cancer Society. [Online]. Available: http://www.cancer.ca/ , last accessed: May 12, 2015.

[5] National Cancer Institute. [Online]. Available: http://www.cancer.gov/ , last accessed: April 15, 2015.

[6] S. Nass and I. Henderson, *Mammography and beyond: developing technologies for the early detection of breast cancer*. National Academies Press, 2001.

[7] M. Patlak, S. Nass, I. Henderson, and J. Lashof, *Mammography and Beyond: Developing Technologies for the Early Detection of Breast Cancer: A Non-Technical Summary*. National Academies Press, 2001.

[8] M. Morrow, J. Waters, and E. Morris, "MRI for breast cancer screening, diagnosis, and treatment," *The Lancet*, vol. 378, no. 9805, pp. 1804–1811, 2011.

[9] S. K. Moore, "Better breast cancer detection," *Spectrum, IEEE*, vol. 38, no. 5, pp. 50–54, 2001.

[10] C. Gabriel, S. Gabriel, and E. Corthout, "The dielectric properties of biological tissues: I. literature survey," *Physics in Medicine and Biology*, vol. 41, pp. 2231–2249, 1996.

[11] S. Gabriel, R. Lau, and C. Gabriel, "The dielectric properties of biological tissues: II. measurements in the frequency range 10 hz to 20 ghz," *Physics in Medicine and Biology*, vol. 41, pp. 2251–2269, 1996.

[12] ——, "The dielectric properties of biological tissues: III. parametric models for the dielectric spectrum of tissues," *Physics in Medicine and Biology*, vol. 41, pp. 2271–2293, 1996.

[13] E. Fear, P. Meaney, and M. Stuchly, "Microwaves for breast cancer detection?" *IEEE potentials*, vol. 22, no. 1, pp. 12–18, 2003.

[14] F. Moinfar, *Essentials of diagnostic breast pathology: a practical approach*. Springer, 2007.

[15] *A Guide to Mammography and Other Breast Imaging Procedures: (Report No. 149). National Council on Radiation Protection and Measurements (NCRP)*. National Council on Radiation Protection and Measurements (NCRP), 2004.

[16] D. Dershaw, *Imaging-guided interventional breast techniques*. Springer Verlag, 2003.

[17] S. Nass, J. Ball *et al.*, *Improving breast imaging quality standards*. National Academies Press, 2005.

[18] G. Rovere, R. Warren, and J. Benson, Eds., *Early Breast Cancer: From screening to multidisciplinary management*. Taylor & Francis, 2006.

[19] E. D. Pisano, M. Zuley, J. K. Baum, and H. S. Marques, "Issues to consider in converting to digital mammography," *Radiologic clinics of North America*, vol. 45, no. 5, pp. 813–830, 2007.

[20] M. J. Michell, Ed., *Breast Cancer*, 1st ed., ser. Contemporary Issues in Cancer Imaging. Cambridge University Press, 2010.

[21] I. C. Duarte, L. Caldeira, F. Soares, F. Janela, and J. S. Silva, "3d medical image reconstruction on digital breast tomosynthesis," in *Bioengineering (ENBENG), 2012 IEEE 2nd Portuguese Meeting in*, pp. 1–6, 2012.

[22] M. Males, D. Mileta, and M. Grgic, "Digital breast tomosynthesis: A technological review," in *ELMAR, 2011 Proceedings*, pp. 41–45, 2011.

[23] S. L. Rose, A. L. Tidwell, L. J. Bujnoch, A. C. Kushwaha, A. S. Nordmann, and R. Sexton Jr, "Implementation of breast tomosynthesis in a routine screening practice: An observational study," *American Journal of Roentgenology*, vol. 200, no. 6, pp. 1401–1408, 2013.

[24] N. Pallikarakis and K. Bliznakova, "Advances in X-ray breast imaging using digital tomosynthesis," in *E-Health and Bioengineering Conference (EHB), 2011*, pp. 1–6. IEEE, 2011.

[25] D. Gur, G. S. Abrams, D. M. Chough, M. A. Ganott, C. M. Hakim, R. L. Perrin, G. Y. Rathfon, J. H. Sumkin, M. L. Zuley, and A. I. Bandos, "Digital breast tomosynthesis: observer performance study," *American Journal of Roentgenology*, vol. 193, no. 2, pp. 586–591, 2009.

[26] S. P. Poplack, T. D. Tosteson, C. A. Kogel, and H. M. Nagy, "Digital breast tomosynthesis: initial experience in 98 women with abnormal digital screening mammography," *American Journal of Roentgenology*, vol. 189, no. 3, pp. 616–623, 2007.

[27] J. L. Prince and J. M. Links, *Medical Imaging Signals and Systems*. Prentice Hall, Inc., 2006.

[28] C. Stelling, P. Wang, A. Lieber, S. Mattingly, W. Griffen, and D. Powell, "Prototype coil for magnetic resonance imaging of the female breast. work in progress." *Radiology*, vol. 154, no. 2, pp. 457–462, 1985.

[29] C. Kuhl, S. Schrading, C. Leutner, N. Morakkabati-Spitz, E. Wardelmann, R. Fimmers, W. Kuhn, and H. Schild, "Mammography, breast ultrasound, and magnetic resonance imaging for surveillance of women at high familial risk for breast cancer," *Journal of clinical oncology*, vol. 23, no. 33, p. 8469, 2005.

[30] S. G. Orel and M. D. Schnall, "MR imaging of the breast for the detection, diagnosis, and staging of breast cancer," *Radiology*, vol. 220, no. 1, pp. 13–30, 2001.

[31] C. D. Lehman and M. D. Schnall, "Imaging in breast cancer: magnetic resonance imaging," *Breast Cancer Research*, vol. 7, no. 5, p. 215, 2005.

[32] A. Karellas and S. Vedantham, "Breast cancer imaging: A perspective for the next decade," *Medical Physics*, vol. 35, no. 11, pp. 4878–4897, 2008.

[33] A. M. Hassan and M. El-Shenawee, "Review of electromagnetic techniques for breast cancer detection," *IEEE Reviews in Biomedical Engineering*, vol. 4, pp. 103–118, 2011.

[34] K. L. Carr, "Microwave radiometry: Its importance to the detection of cancer," *Microwave Theory and Techniques, IEEE Transactions on*, vol. 37, no. 12, pp. 1862–1869, 1989.

[35] D. Kopans, "Early breast cancer detection using techniques other than mammography," *American Journal of Roentgenology*, vol. 143, no. 3, p. 465, 1984.

[36] K. R. Foster, "Thermographic detection of breast cancer," *Engineering in Medicine and Biology Magazine, IEEE*, vol. 17, no. 6, pp. 10–14, 1998.

[37] A. H. Barrett, P. C. Myers, and N. Sadowsky, "Microwave thermography in the detection of breast cancer," *American Journal of Roentgenology*, vol. 134, no. 2, pp. 365–368, 1980.

[38] R. Tipa and O. Baltag, "Microwave thermography for cancer detection," *Romanian Journal of Physics*, vol. 51, no. 3/4, pp. 371–377, 2006.

[39] M. Anbar, C. Brown, and L. Milescu, "Objective identification of cancerous breasts by dynamic area telethermometry (dat)," *Thermology International*, vol. 9, pp. 127–133, 1999.

[40] C. J. Chang, J. L. Sibala, J. H. Gallagher, R. C. Riley, A. W. Templeton, P. V. Beasley, and R. A. Porte, "Computed tomography of the breast a preliminary report," *Radiology*, vol. 124, no. 3, pp. 827–829, 1977.

[41] J. J. Gisvold, D. F. Reese, and P. R. Karsell, "Computed tomographic mammography (CTM)," *American Journal of Roentgenology*, vol. 133, no. 6, pp. 1143–1149, 1979.

[42] S. Orel and R. Troupin, "Nonmammographic imaging of the breast: current issues and future prospects," in *Seminars in roentgenology*, vol. 28, no. 3, pp. 231–241. Elsevier, 1993.

[43] K. Paulsen, P. Meaney, and L. Gilman, *Alternative breast imaging: four model-based approaches*. Springer-Verlag New York Inc, 2005.

[44] M. El-Shenawee, "Electromagnetic imaging for breast cancer research," in *Biomedical Wireless Technologies, Networks, and Sensing Systems (BioWireleSS), 2011 IEEE Topical Conference on*, pp. 55–58, 2011.

[45] B. Brooksby, S. JIang, H. Dehghani, B. W. Pogue, K. D. Paulsen, C. Kogel, M. Doyley, J. B. Weaver, and S. P. Poplack, "Magnetic resonance-guided near-infrared tomography of the breast," *Review of Scientific Instruments*, vol. 75, 2004.

[46] D. S. Holder, *Electrical impedance tomography: methods, history and applications*. CRC Press, 2010.

[47] Y. A. Glickman, O. Filo, U. Nachaliel, S. Lenington, S. Amin-Spector, and R. Ginor, "Novel EIS postprocessing algorithm for breast cancer diagnosis," *Medical Imaging, IEEE Transactions on*, vol. 21, no. 6, pp. 710–712, 2002.

[48] D. Flores-Tapia and S. Pistorius, "Electrical impedance tomography reconstruction using a monotonicity approach based on a priori knowledge," in *2010 Annual International Conference of the IEEE Engineering in Medicine and Biology Society, EMBC'10*, pp. 4996–4999, 2010.

[49] Y. Zou and Z. Guo, "A review of electrical impedance techniques for breast cancer detection," *Medical Engineering and Physics*, vol. 25, no. 2, pp. 79–90, 2003.

[50] C. Li and L. V. Wang, "Photoacoustic tomography and sensing in biomedicine," *Physics in Medicine and Biology*, vol. 54, pp. R59–R97, 2009.

[51] A. Abbosh, "Early breast cancer detection using hybrid imaging modality," in *Proc. IEEE International Symposium on Antennas & Propagation & USNC/URSI National Radio Science Meeting (AP-S/URSI'09)*, 2009.

[52] H. Rivaz, P. Foroughi, I. Fleming, R. Zellars, E. Boctor, and G. Hager, "Tracked regularized ultrasound elastography for targeting breast radiotherapy," in *MICCAI*, 2009.

[53] A. Surowiec, S. Stuchly, J. Barr, and A. Swarup, "Dielectric properties of breast carcinoma and the surrounding tissues," *Biomedical Engineering, IEEE Transactions on*, vol. 35, no. 4, pp. 257–263, 1988.

[54] W. Joines, Y. Zhang, C. Li, and R. Jirtle, "The measured electrical properties of normal and malignant human tissues from 50 to 900 MHz," *Medical Physics*, vol. 21, p. 547, 1994.

[55] C. Gabriel, "Compilation of the dielectric properties of body tissues at RF and microwave frequencies," Armstrong Laboratory (AFMC) Occupational and Environmental Health Directorate Radiofrequency Radiation Division, Tech. Rep., 1996.

[56] S. Chaudhary, R. Mishra, A. Swarup, and J. Thomas, "Dielectric properties of normal & malignant human breast tissues at radiowave & microwave frequencies," *Indian Journal of Biochemistry & Biophysics*, vol. 21, no. 1, p. 76, 1984.

[57] M. Lazebnik, D. Popovic, L. McCartney, C. Watkins, M. Lindstrom, J. Harter, S. Sewall, T. Ogilvie, A. Magliocco, T. Breslin *et al.*, "A large-scale study of the ultrawideband microwave dielectric properties of normal, benign and malignant breast tissues obtained from cancer surgeries," *Physics in Medicine and Biology*, vol. 52, no. 20, pp. 6093–6116, 2007.

[58] R. J. Halter, T. Zhou, P. M. Meaney, A. Hartov, R. J. Barth Jr, K. M. Rosenkranz, W. A. Wells, C. A. Kogel, A. Borsic, E. J. Rizzo *et al.*, "The correlation of in vivo

and ex vivo tissue dielectric properties to validate electromagnetic breast imaging: initial clinical experience," *Physiological measurement*, vol. 30, no. 6, p. S121, 2009.

[59] T. Sugitani, S. Kubota, S.-i. Kuroki, K. Sogo, K. Arihiro, M. Okada, T. Kadoya, M. Hide, M. Oda, and T. Kikkawa, "Complex permittivities of breast tumor tissues obtained from cancer surgeries," *Applied Physics Letters*, vol. 104, 2014.

[60] L. Larsen and J. Jacobi, *Medical applications of microwave imaging*. Storming Media, 1985.

[61] S. C. Hagness, A. Taflove, and J. E. Bridges, "Two-dimensional fdtd analysis of a pulsed microwave confocal system for breast cancer detection: fixed-focus and antenna-array sensors," *IEEE Trans. Biomed. Eng.*, vol. 45, no. 12, pp. 1470–1479, 1998.

[62] Y. Wang and W. Chew, "An iterative solution of the two-dimensional electromagnetic inverse scattering problem," *International Journal of Imaging Systems and Technology*, vol. 1, no. 1, pp. 100–108, 1989.

[63] W. Chew and Y. Wang, "Reconstruction of two-dimensional permittivity distribution using the distorted born iterative method," *Medical Imaging, IEEE Transactions on*, vol. 9, no. 2, pp. 218–225, 1990.

[64] W. Chew and G. P. Otto, "Microwave imaging of multiple metallic cylinders using shape functions," in *Antennas and Propagation Society International Symposium, 1992. AP-S. 1992 Digest. Held in Conjuction with: URSI Radio Science Meeting and Nuclear EMP Meeting., IEEE*, pp. 1716–1719, 1992.

[65] P. Meaney, M. Fanning, D. Li, S. Poplack, and K. Paulsen, "A clinical prototype for active microwave imaging of the breast," *IEEE Transactions on Microwave Theory and Techniques*, vol. 48, no. 11 Part 1, pp. 1841–1853, 2000.

[66] A. H. Golnabi, P. M. Meaney, S. Geimer, and K. D. Paulsen, "Microwave imaging for breast cancer detection and therapy monitoring," in *Biomedical Wireless Technologies, Networks, and Sensing Systems (BioWireleSS), 2011 IEEE Topical Conference on*, pp. 59–62, 2011.

[67] L. V. Wang, X. Zhao, H. Sun, and G. Ku, "Microwave-induced acoustic imaging of biological tissues," *Review of Scientific Instruments*, vol. 70, pp. 3744–3748, 1999.

[68] R. A. Kruger, W. L. Kiser, Jr., D. R. Reinecke, G. A. Kruger, and R. L. Eisenhart, "Thermoacoustic computed tomography of the breast at 434 mhz," in *IEEE MTT-Symposium*, 1999.

[69] E. Kirshin, B. Oreshkin, K. Zhu, M. Popovic, and M. Coates, "Fusing microwave radar and microwave-induced thermoacoustics for breast cancer detection," in *Biomedical Imaging: From Nano to Macro, 2011 IEEE International Symposium on*, pp. 113–116, 2011.

[70] J. E. Bridges, "Non-invasive system for breast cancer detection," US Patent 5,704,355, 1998.

[71] E. Fear and J. Sill, "Preliminary investigations of tissue sensing adaptive radar for breast tumor detection," in *Engineering in Medicine and Biology Society, 2003. Proceedings of the 25th Annual International Conference of the IEEE*, vol. 4, 2003.

[72] E. Porter, E. Kirshin, A. Santorelli, M. Coates, and M. Popovic, "Time-domain multistatic radar system for microwave breast screening," *Antennas and Wireless Propagation Letters, IEEE*, vol. 12, pp. 229–232, 2013.

[73] M. Klemm, I. Craddock, A. Preece, J. Leendertz, and R. Benjamin, "Evaluation of a hemi-spherical wideband antenna array for breast cancer imaging," *Radio Science*, vol. 43, no. 6, 2008.

[74] Y. Kuwahara, K. Suzuki, H. Horie, and H. Hatano, "Conformal array antenna with the aspirator for the microwave mammography," in *Antennas and Propagation Society International Symposium (APSURSI), 2010 IEEE*, pp. 1–4, 2010.

[75] E. J. Bond, X. Li, S. C. Hagness, and B. D. van Veen, "Microwave imaging via space-time beamforming for early detection of breast cancer," *IEEE Trans. Antennas Propag.*, vol. 51, pp. 1690–1705, 2003.

[76] S. K. Davis, H. Tandradinata, S. C. Hagness, and B. D. van Veen, "Ultrawideband microwave breast cancer detection: a detection-theoretic approach using the generalized likelihood ratio test," *IEEE Trans. Biomed. Eng.*, vol. 52, pp. 1237–1250, 2005.

[77] R. C. Conceicao, M. O'Halloran, M. Glavin, and E. Jones, "Comparison of planar and circular antenna configurations for breast cancer detection using microwave imaging," *Progress In Electromagnetics Research*, vol. 99, pp. 1–20, 2009.

[78] M. Hernandez-Lopez, M. Quintillan-Gonzalez, S. González García, A. Rubio Bretones, and R. Gomez Martin, "A rotating array of antennas for confocal microwave breast imaging," *Microwave and optical technology letters*, vol. 39, no. 4, pp. 307–311, 2003.

[79] S. Hagness, A. Taflove, and J. Bridges, "Three-dimensional fdtd analysis of a pulsed microwave confocal system for breast cancer detection: Design of an antenna-array

element," *Antennas and Propagation, IEEE Transactions on*, vol. 47, no. 5, pp. 783–791, 1999.

[80] H. Kanj and M. Popovic, "Miniaturized microstrip-fed "dark eyes" antenna for near-field microwave sensing," *IEEE Antennas and Wireless Propagation Letters*, vol. 4, 2005.

[81] C. Shannon, E. Fear, and M. Okoniewski, "Dielectric-filled slotline bowtie antenna for breast cancer detection," *Electronics Letters*, vol. 41, no. 7, pp. 388–390, 2005.

[82] M. Hein, C. Geyer, M. Helbig, I. Hilger, J. Sachs, U. Schwarz, F. Seifert, R. Stephan, and F. Thiel, "Antennas for ultra-wideband medical sensor systems," in *Antennas and Propagation, 2009. EuCAP 2009. 3rd European Conference on*, pp. 1868–1872, 2009.

[83] F. Scotto di Clemente, R. Stephan, and M. Hein, "Ultra-wideband miniaturised high permittivity-matched antennas for biomedical diagnostic," in *Antennas and Propagation (EuCAP), 2013 7th European Conference on*, pp. 2896–2899, 2013.

[84] J. Bourqui, M. A. Campbell, T. Williams, and E. C. Fear, "Antenna evaluation for ultra-wideband microwave imaging," *International Journal of Antennas and Propagation*, vol. 2010, 2010.

[85] R. Nilavalan, J. Leendertz, I. Craddock, R. Benjamin, and A. Preece, "Breast tumour detection using a flat 16 element array," in *Proc. 16th Int. Symp. on Electromagn. Compat. Topical Meeting on Biomed. EMC*, pp. 81–84, 2005.

[86] A. Sabouni and A. Kishk, "Dual-polarized, broadside, thin dielectric resonator antenna for microwave imaging," *Antennas and Wireless Propagation Letters, IEEE*, vol. 12, pp. 380–383, 2013.

[87] J. Sill and E. Fear, "Tissue sensing adaptive radar for breast cancer detection: study of immersion liquids," *Electronics Letters*, vol. 41, no. 3, pp. 113–115, 2005.

[88] B. Zhou, W. Shao, and G. Wang, "Uwb microwave imaging for early breast cancer detection: effect of the coupling medium on resolution," in *2004 Asia-Pacific Radio Science Conference Proceedings*, vol. 2004, pp. 431–4, 2004.

[89] A. M. Abbosh, M. E. Bialkowski, and S. Crozier, "Investigations into optimum characteristics for the coupling medium in uwb breast cancer imaging systems," in *Proc. IEEE International Symposium on Antennas & Propagation & USNC/URSI National Radio Science Meeting (AP-S/URSI'08)*, 2008.

[90] A. Santorelli, E. Kirshin, E. Porter, M. Popovic, and J. Schwartz, "Improved calibration for an experimental time-domain microwave imaging system," in *Antennas and Propagation (EuCAP), 2013 7th European Conference on*, pp. 801–805, 2013.

[91] *IEEE Standard for Safety Levels with Respect to Human Exposure to Radio Frequency Electromagnetic Fields, 3 kHz to 300 GHz*, IEEE Std., 1999.

[92] *American National Standard Recommended Practice for the Measurement of Hazardous Electromagnetic Fields-RF and Microwave*, IEEE Std., 1981.

[93] *IEEE Recommended Practice for Radio Frequency Safety Programs, 3 kHz to 300 GHz*, IEEE Std., 2005.

[94] E. Fear, X. Li, S. Hagness, and M. Stuchly, "Confocal microwave imaging for breast cancer detection: Localization of tumors in three dimensions," *IEEE Trans. Biomed. Eng.*, vol. 49, pp. 812–822, 2002.

[95] Y. Xie, B. Guo, J. Li, G. Ku, and L. V. Wang, "Adaptive and robust methods of reconstruction for thermoacoustic tomography," *IEEE Trans. Biomed. Eng.*, vol. 55, pp. 2741–2842, 2008.

[96] E. Kirshin, G. Zhu, M. Popovic, and M. Coates, "Evaluation of the mono-static microwave radar algorithms for breast imaging," in *Antennas and Propagation (EUCAP), Proceedings of the 5th European Conference on*, pp. 881–885, 2011.

[97] A. Lazaro, D. Girbau, and R. Villarino, "Wavelet-based breast tumor localization technique using a uwb radar," *Progress In Electromagnetics Research*, pp. 75–95, 2009.

[98] Y. Chen, E. Gunawan, K. S. Low, S. chang Wang, Y. Kim, and C. B. Soh, "Pulse design for time reversal method as applied to ultrawideband micrwoave breast cancer detection: a two-dimensional analysis," *IEEE Trans. Antennas Propag.*, vol. 55, no. 1, pp. 194–204, 2007.

[99] A. Santorelli, M. Chudzik, E. Kirshin, E. Porter, A. Lujambio, I. Arnedo, M. Popovic, and J. Schwartz, "Experimental demonstration of pulse shaping for time-domain microwave breast imaging," *Progress In Electromagnetics Research*, vol. 133, pp. 309–329, 2013.

[100] X. Zeng, A. Fhager, M. Persson, P. Linner, and H. Zirath, "An ultrawideband microwave medical diagnostic system: Design considerations and system performance," in *Antennas and Propagation (EUCAP), 2012 6th European Conference on*, pp. 3664–3668, 2012.

[101] H. Mextorf, F. Daschner, M. Kent, and R. Knchel, "Non-contacting moisture sensing using a dedicated uwb time domain instrument," in *Microwave Conference (GeMiC), 2012 The 7th German*, pp. 1–4, 2012.

[102] J. Sill, T. Williams, E. Fear, R. Frayne, and M. Okoniewski, "Realistic breast models for second generation tissue sensing adaptive radar system," *2nd European Conference on Antennas and Propagation, EuCAP 2007*, vol. 2007, no. 11961, 2007.

[103] G. Zhu, B. Oreshkin, E. Porter, M. Coates, and M. Popović, "Numerical breast models for commercial fdtd simulators," in *Proc. European Conference on Antennas and Propagation (EuCAP'09)*, Berlin, Germany, 2009.

[104] CST - Computer Simulation Technology. [Online]. Available: https://www.cst.com/ , last accessed: Aug 12, 2015.

[105] Schmid & Partner Engineering AG. [Online]. Available: http://www.speag.com/ , last accessed: Aug 12, 2015.

[106] ANSYS - Simulation Driven Product Development. [Online]. Available: http://www.ansys.com/ , last accessed: Aug 12, 2015.

[107] COMSOL Multiphysics. [Online]. Available: http://www.comsol.com/ , last accessed: Aug 12, 2015.

[108] E. Porter, J. Fakhoury, R. Oprisor, M. Coates, and M. Popovic, "Improved tissue phantoms for experimental validation of microwave breast cancer detection," in *Antennas and Propagation (EuCAP), 2010 Proceedings of the Fourth European Conference on*, pp. 1–5, 2010.

[109] A. Bakar, A. Abbosh, P. Sharpe, M. Bialkowski, and Y. Wang, "Heterogeneous breast phantom for ultra wideband microwave imaging," *Microwave and Optical Technology Letters*, vol. 53, no. 7, pp. 1595–1598, 2011.

[110] M. Burfeindt, T. Colgan, R. Mays, J. Shea, N. Behdad, B. Van Veen, and S. Hagness, "Mri-derived 3-d-printed breast phantom for microwave breast imaging validation," *Antennas and Wireless Propagation Letters, IEEE*, vol. 11, pp. 1610–1613, 2012.

[111] R. C. Conceicao, M. O'Halloran, R. M. Capote, C. S. Ferreira, N. Matela, H. A. Ferreira, M. Glavin, E. Jones, and P. Almeida, "Development of breast and tumour models for simulation of novel multimodal PEM-UWB technique for detection and classification of breast tumours," in *Nuclear Science Symposium and Medical Imaging Conference (NSS/MIC), 2012 IEEE*, pp. 2769–2772, 2012.

[112] J. C. Y. Lai, C. B. Soh, E. Gunawan, and K. S. Low, "Homogeneous and heterogeneous breast phantoms for ultra-wideband microwave imaging applications," *Progress In Electromagnetics Research*, vol. 100, pp. 397–415, 2010.

[113] D. Winters, J. Shea, E. Madsen, G. Frank, B. Veen, and S. Hagness, "Estimating the breast surface using uwb microwave monostatic backscatter measurements," *IEEE Transactions on Biomedical Engineering*, vol. 55, no. 1, pp. 247–256, 2008.

[114] T. Williams, E. Fear, and D. Westwick, "Tissue sensing adaptive radar for breast cancer detection–investigations of an improved skin-sensing method," *IEEE Trans. Microw. Theory Tech.*, vol. 54, pp. 1308–1314, 2006.

[115] T. Williams and E. Fear, "Tissue sensing adaptive radar for breast cancer detection: skin outline creation on a complex simulated hemispherical breast model," in *2007 IEEE Antennas and Propagation Society International Symposium*, pp. 2156–2159, 2007.

[116] T. Williams, J. Sill, and E. Fear, "Breast surface estimation for radar-based breast imaging systems," *Biomedical Engineering, IEEE Transactions on*, vol. 55, no. 6, pp. 1678–1686, 2008.

[117] ——, "Robust approach to skin location estimation for radar-based breast imaging systems," *IEEE transactions on Engineering in Medicine and Biology*, vol. 2009, pp. 5837–5841, 2009.

[118] X. Li, E. Bond, B. Van Veen, and S. Hagness, "An overview of ultra-wideband microwave imaging via space-time beamforming for early-stage breast-cancer detection," *IEEE Antennas and Propagation Magazine*, vol. 47, no. 1, pp. 19–34, 2005.

[119] D. W. Winters, E. J. Bond, B. D. van Veen, and S. C. Hagness, "Estimation of the frequency-dependent average dielectric properties of breast tissue using a time-domain inverse scattering technique," *IEEE Trans. Antennas Propag.*, vol. 54, no. 11, pp. 3517–3528, 2006.

[120] D. W. Winters, B. D. V. Veen, and S. C. Hagness, "A three-dimensional inverse scattering technique for estimating the nominal dielectric properties of breast tissue at microwave frequencies," in *Proc. IEEE International Symposium on Antennas & Propagation (AP-S'07)*, 2007.

[121] D. W. Winters, J. D. Shea, P. Kosmas, B. D. V. Veen, and S. C. Hagness, "Three-dimensional microwave breast imaging: dispersive dielectric properties estimation using patient-specific basis functions," *IEEE Trans. Med. Imag.*, vol. 28, no. 7, pp. 969–981, 2009.

[122] M. O'Halloran, E. Jones, and M. Glavin, "Quasi-multistatic MIST beamforming for the early detection of breast cancer," *IEEE Trans. Biomed. Eng.*, vol. 57, pp. 830–840, 2010.

[123] W. Zhi and F. Chin, "Entropy-based time window for artifact removal in uwb imaging of breast cancer detection," *IEEE Signal Processing Letters*, vol. 13, no. 10, pp. 585–588, 2006.

[124] A. Maskooki, E. Gunawan, C. Soh, and K. Low, "Frequency domain skin artifact removal method for ultra-wideband breast cancer detection," *Progress In Electromagnetics Research*, vol. 98, pp. 299–314, 2009.

[125] E. Fear and M. Stuchly, "Confocal microwave imaging for breast tumor detection: a study of resolution and detection ability," *IEEE Transactions on Engineering in Medicine and Biology*, vol. 3, no. 3, pp. 2355–2358, 2001.

[126] E. Fear, J. Sill, and M. Stuchly, "Experimental feasibility study of confocal microwave imaging for breast tumor detection," *IEEE Transactions on Microwave Theory and Techniques*, vol. 51, no. 3, pp. 887–892, 2003.

[127] H. B. Lim, N. T. T. Nhung, E.-P. Li, and N. D. Thang, "Confocal microwave imaging for breast cancer detection: delay-multiply-and-sum image reconstruction algorithm," *IEEE Trans. Biomed. Eng.*, vol. 55, no. 6, pp. 1697–1704, 2008.

[128] M. Klemm, I. Craddock, J. Leendertz, A. Preece, and R. Benjamin, "Improved delay-and-sum beamforming algorithm for breast cancer detection," *International Journal of Antennas and Propagation*, 2008.

[129] M. K. Paul, M. A. K. Sagar, S. U. Hussain, and A. Rashid, "UWB microwave imaging via modified beamforming for early detection of breast cancer," in *Electrical and Computer Engineering (ICECE), 2010 International Conference on*, pp. 642–645, 2010.

[130] S. S. Tiang, M. Sadoon, T. F. Zanoon, M. F. Ain, and M. Z. Abdullah, "Radar sensing featuring biconical antenna and enhanced delay and sum algorithm for early stage breast cancer detection," *Progress In Electromagnetics Research B*, vol. 46, pp. 299–316, 2013.

[131] M. O'Halloran, M. Glavin, and E. Jones, "Channel-ranked beamformer for the early detection of breast cancer," *Progress In Electromagnetics Research*, vol. 103, pp. 153–168, 2010.

[132] X. Li, S. Davis, S. Hagness, D. van der Weide, and B. Van Veen, "Microwave imaging via space-time beamforming: Experimental investigation of tumor detection

in multilayer breast phantoms," *IEEE Transactions on Microwave Theory and techniques*, vol. 52, no. 8, pp. 1856–1865, 2004.

[133] A. Shahzad, M. O'Halloran, E. Jones, and M. Glavin, "Prefiltered beamforming for early-stage breast cancer detection," *Antennas and Wireless Propagation Letters, IEEE*, vol. 12, pp. 500–503, 2013.

[134] M. O'Halloran, M. Glavin, and E. Jones, "Performance and robustness of a multistatic MIST beamforming algorithm for breast cancer detection," *Progress in Electromagnetics Research*, vol. 105, pp. 403–424, 2010.

[135] D. Byrne, M. O'Halloran, E. Jones, and M. Glavin, "A comparison of data-independent microwave beamforming algorithms for the early detection of breast cancer," in *Proc. Annual Int. Conf. of the IEEE Engineering in Medicine and Biology Society EMBC 2009*, pp. 2731–2734, 2009.

[136] D. Byrne, M. O'Halloran, M. Glavin, and E. Jones, "Data independent radar beamforming algorithms for breast cancer detection," *Progress in Electromagnetic Research*, vol. 107, pp. 331–348, 2010.

[137] Y. Benjamini and Y. Hochberg, "Controlling the false discovery rate: a practical and powerful approach to multiple testing," *Journal of the Royal Statistical Society. Series B (Methodological)*, pp. 289–300, 1995.

[138] P. Chung, J. Bohme, C. Mecklenbrauker, and A. Hero, "On signal detection using the benjamini-hochberg procedure," in *Proc. IEEE Workshop on Statistical and Signal Processing*. Citeseer, 2005.

[139] ——, "Multiple signal detection using the benjamini-hochberg procedure," in *IEEE International Workshop on Computational Advances in Multi-Sensor Adaptive Processing*, pp. 209–212. Citeseer, 2005.

[140] E. Bond, B. Van Veen, and S. Hagness, "Multiple window based ultrawideband microwave imaging for early-stage breast cancer detection," in *Fourth IEEE Workshop on Sensor Array and Multichannel Processing, 2006*, pp. 127–131, 2006.

[141] B. Guo, Y. Wang, J. Li, P. Stoica, and R. Wu, "Microwave imaging via adaptive beamforming methods for breast cancer detection," *Progress In Electromagnetics Research*, vol. 1, pp. 350–353, 2005.

[142] ——, "Microwave imaging via adaptive beamforming methods for breast cancer detection," *Journal of Electromagnetic Waves and Applications*, vol. 20, pp. 53–63, 2006.

[143] Y. Xie, B. Guo, L. Xu, J. Li, and P. Stoica, "Multistatic adaptive microwave imaging for early breast cancer detection," *IEEE Trans. Biomed. Eng*, vol. 53, pp. 1647–1657, 2006.

[144] Y. Xie, B. Guo, J. Li, and P. Stoica, "Novel multistatic adaptive microwave imaging methods for early breast cancer detection," *EURASIP Journal on applied signal processing*, vol. 20, 2006.

[145] A. Munawar, S. Adabi, A. Ismail, M. Saripan, R. Mahmood, W. Mahadi, and R. Raja Abdullah, "Breast cancer detection using forward scattering radar technique," in *RF and Microwave Conference, 2008. RFM 2008. IEEE International*, pp. 252–256, 2008.

[146] Y. Jin, Y. Jiang, and J. Moura, "Time reversal beamforming for microwave breast cancer detection," in *Proceedings of the IEEE Intational Conference on Image Processing*, pp. 13–16, 2007.

[147] Y. Jin, J. Moura, Y. Jiang, M. Wahl, H. Zhu, and Q. He, "Breast cancer detection by time reversal imaging," *2008 IEEE International Symposium on Biomedical Imaging: From Macro to Nano (ISBI '08)*, pp. 816–19, 2008.

[148] D. Flores-Tapia, G. Thomas, and S. Pistorius, "Wavefront reconstruction method for subsurface radar imagery acquired along circular and planar scan trajectories," *Aerospace and Electronic Systems, IEEE Transactions on*, vol. 46, no. 3, pp. 1346–1363, 2010.

[149] A. Kerhet, M. Raffetto, A. Boni, and A. Massa, "A svm-based approach to microwave breast cancer detection," *Engineering Applications of Artificial Intelligence*, vol. 19, no. 7, pp. 807–818, 2006.

[150] S. AlShehri and S. Khatun, "UWB imaging for breast cancer detection using neural network," *Progress In Electromagnetics Research*, vol. 7, pp. 79–93, 2009.

[151] D. Woten and M. El-Shenawee, "Error analysis of breast tumor signature versus skin thickness at microwave frequencies," in *Proc. IEEE International Symposium on Antennas & Propagation (AP-S'08)*, pp. 1–4, 2008.

[152] D. Kurrant, E. Fear, and D. Westwick, "Tumor response estimation in radar-based microwave breast cancer detection," *Biomedical Engineering, IEEE Transactions on*, vol. 55, no. 12, pp. 2801–2811, 2008.

[153] S. Davis, B. V. Veen, S. C. Hagness, and F. Kelcz, "Breast tumor characterization based on ultrawideband microwave backscatter," *IEEE Trans. Biomed. Eng.*, vol. 55, no. 1, pp. 237 –246, 2008.

[154] J. Teo, Y. Chen, C. B. Soh, E. Gunawan, K. S. Low, T. C. Putti, and S.-C. Wang, "Breast lesion classification using ultrawideband early time breast lesion response," *IEEE Trans. Antennas Propag.*, vol. 58, no. 8, pp. 2604–2613, 2010.

[155] R. C. Conceicao, M. O'Halloran, E. Jones, and M. Glavin, "Investigation of classifiers for early-stage breast cancer based on radar target signatures," *Progress In Electromagnetics Research*, vol. 105, pp. 295–311, 2010.

[156] M. O'Halloran, B. McGinley, R. C. C. ao, F. Morgan, E. Jones, and M. Galvin, "Spiking neural networks for breast cancer classification in a dielectrically heterogeneous breast," *Progress in Electromagnetics Research M*, vol. 113, pp. 413–428, 2011.

[157] D. Byrne, M. O'Halloran, E. Jones, and M. Glavin, "Support vector machine-based ultrawideband breast cancer detection system," *Journal of Electromagnetic Waves and Applications*, vol. 25, no. 13, pp. 1807–1816, 2011.

[158] R. Conceicao, H. Medeiros, M. O'Halloran, D. Rodriguez-Herrera, D. Flores-Tapia, and S. Pistorius, "Initial classification of breast tumour phantoms using a UWB radar prototype," in *Electromagnetics in Advanced Applications (ICEAA), 2013 International Conference on*, pp. 720–723, 2013.

[159] A. Santorelli, E. Porter, E. Kirshin, Y. J. Liu, and M. Popovic, "Investigation of classifiers for tumor detection with an experimental time-domain breast screening system," *Progress In Electromagnetics Research*, vol. 144, pp. 45–57, 2014.

[160] J. Bourqui, J. Sill, and E. Fear, "A prototype system for measuring microwave frequency reflections from the breast," *Journal of Biomedical Imaging - Special issue on Microwave Imaging and Emerging Applications*, vol. 2012, 2012.

[161] M. Klemm, I. Craddock, J. Leendertz, A. Preece, D. Gibbins, M. Shere, and R. Benjamin, "Clinical trials of a uwb imaging radar for breast cancer," in *Proc. Eur. Conf. Ant. and Prop. (EuCAP), 2010*, pp. 1–4. IEEE, 2010.

[162] M. Klemm, D. Gibbins, J. Leendertz, T. Horseman, A. Preece, R. Benjamin, and I. Craddock, "Development and testing of a 60-element UWB conformal array for breast cancer imaging," in *Antennas and Propagation (EUCAP), Proceedings of the 5th European Conference on*, pp. 3077–3079, 2011.

[163] E. Porter, E. Kirshin, A. Santorelli, and M. Popovic, "A clinical prototype for microwave breast imaging using time-domain measurements," in *Antennas and Propagation (EuCAP), 2013 7th European Conference on*, pp. 830–832, 2013.

[164] B. Maklad, C. Curtis, E. Fear, and G. Messier, "A skin response estimation and suppression technique for radar-based microwave breast imaging applications," in *Antennas and Propagation (EUCAP), 2012 6th European Conference on*, pp. 1772–1775, 2012.

[165] M. Elahi, A. Shahzad, M. Glavin, E. Jones, and M. O'Halloran, "Hybrid artifact removal for confocal microwave breast imaging," *Antennas and Wireless Propagation Letters, IEEE*, vol. 13, pp. 149–152, 2014.

[166] D. K. Cheng, *Field and wave electromagnetics*, 2nd ed. Addison-Wesley New York, 1989.

[167] A. Sihvola, *Electromagnetic Mixing Formulas and Applications*. Institution of Electrical Engineers, 1999.

[168] C. Balanis, *Advanced engineering electromagnetics*. Wiley New York, 1989.

[169] R. F. Harrington, *Time-Harmonic Electromagnetic Fields*. Piscataway, NJ: IEEE Press, 2001.

[170] A. Ishimaru, *Electromagnetic wave propagation, radiation, and scattering*. Prentice Hall Englewood Cliffs, NJ:, 1991.

[171] E. J. Bond, S. C. Hagness, B. D. Van Veen *et al.*, "Surface identification using microwave signals for microwave-based detection of cancer," US Patent 7,647,089, 2010.

[172] M. Sarafianou, D. Gibbins, I. Craddock, M. Klemm, J. Leendertz, A. Preece, and R. Benjamin, "Breast surface reconstruction algorithm for a multi-static radar-based breast imaging system," in *Antennas and Propagation (EuCAP), 2010 Proceedings of the Fourth European Conference on*, pp. 1–5, 2010.

[173] D. Kurrant and E. Fear, "Regional estimation of the dielectric properties of the breast: Skin, adipose, and fibroglandular tissues," in *Antennas and Propagation (EUCAP), Proceedings of the 5th European Conference on*, pp. 2920–2924, 2011.

[174] M. Sarafianou, I. Craddock, T. Henriksson, M. Klemm, D. Gibbins, A. Preece, J. Leendertz, and R. Benjamin, "MUSIC processing for permittivity estimation in a delay-and-sum imaging system," in *Antennas and Propagation (EuCAP), 2013 7th European Conference on*, pp. 839–842, 2013.

[175] S. Kay, *Fundamentals of Statistical Signal Processing, Volume 2: Detection Theory*. Prentice Hall PTR, 1998.

[176] F. Bandiera, D. Orlando, and G. Ricci, "Advanced radar detection schemes under mismatched signal models," *Synthesis Lectures on Signal Processing*, vol. 4, no. 1, pp. 1–105, 2009.

[177] X. Li and S. C. Hagness, "A confocal microwave imaging algorithm for breast cancer detection," *IEEE Microw. Wireless Compon. Lett.*, vol. 11, no. 3, pp. 130–132, 2001.

[178] J. Li and P. Stoica, *Robust adaptive beamforming*. Wiley Online Library, 2006.

[179] R. A. Kruger, K. Stantz, and W. L. Kiser, Jr., "Thermoacoustic ct of the breast," in *Proc. SPIE Conf. Medical Imaging: Physics of Medical Imaging.*, vol. 4682, pp. 521–525, 2002.

[180] M. Xu and L. Wang, "RF-induced thermoacoustic tomography," in *Proc. Ann. Conf. Biomedical Eng. Soc.*, vol. 2, pp. 1211–1212, 2002.

[181] M. Klemm, I. J. Craddock, J. A. Leendertz, A. Preece, and R. Benjamin, "Radar-based breast cancer detection using a hemispherical antenna array—experimental results," *IEEE Trans. Antennas Propag.*, vol. 57, pp. 1692–1704, 2009.

[182] B. Oreshkin, E. Kirshin, G. K. Zhu, M. Popovic, and M. Coates, "Null hypothesis distributions of the test statistics for the dual-modality fused detection," 2011. [Online]. Available: http://www.tsp.ece.mcgill.ca/Networks/publications-techreport.html , last accessed: Aug 12, 2015.

[183] V. Adamchik and O. Marichev, "The algorithm for calculating integrals of hypergeometric type functions and its realization in reduce system," in *Proc. ACM Int Symp. Symbolic and Algebraic Computation*, pp. 212–224, 1990.

[184] E. Zastrow, S. K. Davis, M. Lazebnik, F. Kelcz, B. D. van Veen, and S. C. Hagness, "Database of 3d grid-based numerical breast phantoms for use in computational electromagnetics simulations," 2007. [Online]. Available: http://uwcem.ece.wisc.edu/MRIdatabase/InstructionManual.pdf , last accessed: Aug 12, 2015.

[185] M. Lazebnik, M. Okoniewski, J. H. Booske, and S. C. Hagness, "Highly accurate debye models for normal and malignant breast tissue dielectric properties at microwave frequencies," *IEEE Microw. Wireless Compon. Lett.*, vol. 17, pp. 822–824, 2007.

[186] National Physical Laboratory. Kaye and Laby tables of physical and chemical constants. Online. National Physical Laboratory. [Online]. Available: http://www.kayelaby.npl.co.uk , last accessed: Aug 12, 2015.

[187] F. A. Duck, *Physical properties of tissue: A comprehensive reference book*. San Diego, CA: Academic Press, 1990.

[188] J. B. Schneider, "Plane waves in FDTD simulations and a nearly perfect total-field/scattered-field boundary," *IEEE Trans. Antennas Propag.*, vol. 52, pp. 3280–3287, 2004.

[189] A. Taflove and S. Hagness, *Computational Electrodynamics: The Finite-Difference Time-Domain Method*, ser. The Artech House antenna and propagation library. Artech House, Incorporated, 2005.

[190] U. Oğuz and L. Gürel, "Interpolation techniques to improve the accuracy of the plane wave excitations in the finite difference time domain method," *Radio Science*, vol. 32, pp. 2189–2199, 1997.

[191] L. Käll, J. Storey, and W. Noble, "qvality: non-parametric estimation of q-values and posterior error probabilities," *Bioinformatics*, vol. 25, pp. 964–966, 2009.

[192] Model 3600 Impulse Generator. Picosecond Pulse Labs. [Online]. Available: http://www.picosecond.com/product/product.asp?prod_id=104 , last accessed: Aug 12, 2015.

[193] Coaxial High Power Amplifier ZVE-3W-83+. [Online]. Available: http://www.minicircuits.com/pdfs/ZVE-3W-83+.pdf , last accessed: Aug 12, 2015.

[194] E. Porter, A. Santorelli, M. Coates, and M. Popovic, "An experimental system for time-domain microwave breast imaging," in *Antennas and Propagation (EUCAP), Proceedings of the 5th European Conference on*, pp. 2906–2910, 2011.

[195] PicoScope 9200 PC Sampling Oscilloscopes. PicoTech. [Online]. Available: http://www.picotech.com/picoscope9200.html , last accessed: Aug 12, 2015.

[196] *gigaBERT1400. 1400 Mb/s Bit Error Rate Tester Generator and Analyzer.*, Tektronix Inc, 2000.

[197] STM32 F4 series of high-performance MCUs with DSP and FPU instructions. ST Microelectronics. [Online]. Available: http://www.st.com/web/en/catalog/mmc/FM141/SC1169/SS1577?sc=stm32f4 , last accessed: Aug 12, 2015.

[198] E. Porter, E. Kirshin, A. Santorelli, and M. Popović, "Microwave breast screening in the time-domain: Identification and compensation of measurement-induced uncertanties," *Progress In Electromagnetics Research B*, vol. 55, 2013.

[199] S.-C. Pei and C.-C. Tseng, "An efficient design of a variable fractional delay filter using a first-order differentiator," *Signal Processing Letters, IEEE*, vol. 10, no. 10, pp. 307–310, 2003.

[200] J. Olkkonen and H. Olkkonen, "Fractional time-shift b-spline filter," *Signal Processing Letters, IEEE*, vol. 14, no. 10, pp. 688–691, 2007.

[201] X. Zeng, A. Fhager, P. Linner, M. Persson, and H. Zirath, "Experimental investigation of the accuracy of an ultrawideband time-domain microwave-tomographic system," *Instrumentation and Measurement, IEEE Transactions on*, vol. 60, no. 12, pp. 3939 –3949, 2011.

[202] D. Johnson and D. Dudgeon, *Array signal processing: concepts and techniques*. Simon & Schuster, 1992.

[203] H. Van Trees, *Detection, estimation, and modulation theory*. Wiley-Interscience, 2001.

[204] Pico Technology Limited. [Online]. Available: http://www.picotech.com/ , last accessed: Aug 12, 2015.